

Multi-pulsed turbidity current dynamics and geological implications

Viet Luan Ho

Submitted in accordance with the requirements for the degree of
Doctor of Philosophy

The University of Leeds
School of Earth and Environment
June 2018

The candidate confirms that the work submitted is his own, except where work which has formed part of jointly-authored publications has been included. The contribution of the candidate and the other authors to this work has been explicitly indicated below. The candidate confirms that appropriate credit has been given within this thesis where reference has been made to the work of others.

A version of Chapter 3 is published in *Sedimentology*, authored by V.L. Ho, R.M. Dorrell, G.M. Keevil, A.D. Burns and W.D. McCaffrey (VLH, RMD, GMK, ADB, WDM). The candidate, as the main author, acquired, processed experimental data and prepared the manuscript (production figures, plots and writing). RMD helped improve the analysis and presentation of experimental data. GMK provided technical support in running experiments. Discussion with RMD, GMK and WDM helped improve the interpretation of this paper. ADB provided comments and feedback on the paper.

A version of Chapter 4 is published in the *Journal of Geophysical Research: Oceans* by the same authors. The candidate, as the main author, acquired and processed the experimental data that underpin the scaling analysis and also prepared the manuscript. RMD provided feedbacks and suggestions on how to justify the use of the least-squared fitting method and to best present data describing natural flows. RMD and WDM proposed the idea of constraining the scope of application of the study (i.e., only for short, sequential releases on low gradient). GMK and ADB provided feedbacks on the manuscript.

This copy has been submitted on the understanding that it is copyright material and that no quotation from the thesis may be published without proper acknowledgement. The right of Viet Luan Ho to be identified as Author of this work has been asserted by him in accordance with the Copyright, Designs and Patents Act 1988.

Acknowledgement

I would like to express my thanks, first and foremost, to my supervisors: Prof. William D. McCaffrey, Dr Robert M. Dorrell, Dr Gareth M. Keevil and Dr Alan D. Burns. I am very grateful for the time and effort they have invested in me and the golden opportunity for me to broaden my horizon and to have different flavours of research experience. Bill is thanked for his never-ending support in coaching me through my research that helps me step out of my research comfort zone. In particular, he is appreciated for being a great adviser in all aspects and my well-needed teacher who has helped frame my English in a much more British way. Rob who has truly amazed me by his commitment to Maths is thanked for his continuous support in the data analysis of my research. I have saved an awful lot of time by using the MatLab skills acquired during my PhD, that I trust will serve me well in the next steps of my career. Gareth is thanked for his endless help and assistance with my experiments, and more importantly, for making me realise that “every day in the lab is a happy day”, regardless of how intricate equipment could be. Also, my special thank goes to Gareth for never tuning away when I come to find him in the lab. Alan is thanked for his guidance during certain stages of my research.

I would also like to thank Dr Robert E. Thomas and Helena Brown, both working in the Sorby Lab, for their assistance with the experiments. The same appreciation goes to Tony Windross in the Instrument Workshop and Harri (John Wyn) Williams in the Thin Section Lab for their help with setting up my rig and producing sediment samples. Dr Richard Walshaw and Dr Duncan Hedges are thanked for assisting me with using the Scanning Electron Microscope.

Next, I wish to appreciate the administration and IT teams in School of Earth and Environment and Turbidites Research Group for their support that makes my time in Leeds go very smoothly.

Also, I would like to thank my friends in the Institute of Applied Geosciences and Centre of Doctoral Training for sharing their knowledge in

Geology, which does help fulfil the gaps in mine, or simply for the conversations that I have got so dragged-in. In addition, they are thanked for the memories over all the drinks and dinners.

I would also like to thank my family in Vietnam for being so supportive with my PhD and for their unconditional love to me. I want to say a massive thank to my cousins in the USA for making numerous times of my visits feel at home and for loving me like your own brother.

Lastly, I would like to thank my housemates and all other friends in Leeds simply for just being there, making my daily life jam-packed with fun.

Abstract

Deposits of turbidity currents – turbidites – commonly exhibit upward-fining grainsize profiles, reflecting deposition from flows with simple rapidly-waxing then progressively-waning velocity structures. However, turbidites with patterns of multiple cycles of inverse-to-normal grading are not uncommon. Such deposits are interpreted as being deposited under the influence of repeated waxing-waning velocity cycles within multi-pulsed turbidity currents and are termed “multi-pulsed turbidites”. Multi-pulsed flow can be initiated by sequences of retrogressive submarine failures in which each slumping episode can form a pulse in the velocity structure, or may arise due to the combination of multiple flows at downstream confluences; separate flows may even run into each other over long distances. In the first case, it has been inferred that multi-pulsed deposits might carry signals of flow initiation, with each slump linked to a seismic impulse, and further, that such signals can be recognised in the vertical grading structures of distal turbidites. The focus of this research has been to establish i) how multi-pulsed flow dynamics and associated deposits vary along flow pathways and ii) the degree to which grading structures in turbidites deposited by multi-pulsed flows permit inference of flow initiation mechanisms.

Initial experiment modelling of single- and multi-pulsed solute-driven gravity flows shows that internal pulses are necessarily advected forward, eventually merging with the flow head such that multi-pulsed flows transition from being cyclically waxing-waning to waxing on arrival then monotonically waning. This finding implies that initiation signals should be distorted then lost in any deposits along the flow pathway. Accordingly, an interpretational template for the spatial variation in turbidite character along flow pathways was developed, accounting for both pulse merging and flow combination at confluences. Further experiments were conducted to support a scaling analysis to estimate merging lengths; these lengths are shorter than those documented from prototype settings, and may reflect a limitation in the scope of application, arising from experimental constraints. Experiment modelling of single- and multi-pulsed

sediment-driven gravity flows confirms the occurrence of the pulse merging phenomenon in turbidity currents. Analysis of associated deposits confirms the downstream spatial transition from multi- to uni-pulsed turbidites, albeit with the point of transition being more proximal in the laboratory deposit than the point of pulse merging. However, the spatial persistence of the complex velocity structure up to the point of merging need not be reflected in the associated deposit. Beyond the merging point, single-pulsed turbidites must always be deposited. Such deposits cannot be used to infer flow initiation mechanisms.

TABLE OF CONTENTS

ACKNOWLEDGEMENT	iii
ABSTRACT	v
TABLE OF CONTENTS	vii
LIST OF FIGURES	x
LIST OF TABLES	xv
ABBREVIATIONS	xv
Chapter 1: Introduction	1
1.1 AIMS, OBJECTIVES AND OVERVIEW OF THE RESEARCH	1
1.2 THESIS OUTLINE	5
Chapter 2: Literature review	8
2.1 INTRODUCTION	8
2.2 DEFINITION AND CLASSIFICATION OF GRAVITY CURRENTS	8
2.3 TURBIDITY CURRENTS	11
2.3.1 Triggering mechanisms.....	11
2.3.2 Turbidites.....	13
2.4 STRUCTURE AND DYNAMICS OF GRAVITY CURRENTS.....	17
2.4.1 Natural vs. lock-exchange gravity currents	17
2.4.2 Gravity current anatomy and mixing processes	19
2.4.2.1 The head.....	19
2.4.2.2 The body.....	20
2.4.2.3 The tail.....	21
2.4.3 Velocity structure and density profile.....	21
2.4.3.1 Head advance velocity and internal fluid velocity of gravity current.....	21
2.4.3.2 Vertical density profile	23
2.5 EXPERIMENTAL APPROACHES TO STUDY GRAVITY CURRENTS	23
2.5.1 Overview of experimental techniques	23
2.5.2 Experiments and theory for non-particle-driven gravity currents	24
2.5.3 Experiments for particle-driven gravity currents.....	27
Chapter 3: Pulse propagation in turbidity currents	30

3.1 INTRODUCTION	30
3.2 METHODOLOGY	33
3.2.1 Experimental set-up and research methodology	33
3.2.2 Dynamics of density currents	35
3.3 RESULTS	36
3.3.1 Single-pulsed flow	37
3.3.2 Multi-pulsed flow	38
3.3.3 Single-pulsed vs. multi-pulsed flows	42
3.4 DISCUSSION	44
3.4.1 Multi-pulsed turbidity current propagation	44
3.4.2 Conceptual models of deposition from multi-pulsed flows	47
3.4.3 Seismo-turbidites	52
3.5 CONCLUSIONS	55
Chapter 4: Scaling analysis of multi-pulsed turbidity current evolution, with application to turbidite interpretation	57
4.1 INTRODUCTION	58
4.2 METHODOLOGY	60
4.2.1 Experimental set-up	60
4.2.2 Scaling analysis	62
4.2.2.1 Experimental parameters	62
4.2.2.2 Data fitting	66
4.3 RESULTS	70
4.3.1 Flow dynamics	70
4.3.1.1 Single-pulsed flow	71
4.3.1.2 Short-delay time flow	71
4.3.1.3 Long-delay time flow	74
4.3.2 Scaling analysis	75
4.4 DISCUSSION AND APPLICATION	76
4.4.1 Merging phenomenon	76
4.4.2 Application of the scaling analysis	79
4.4.3 Initiation mechanisms of multi-pulsed turbidity currents ..	84
4.5 CONCLUSIONS	87
Chapter 5: Dynamics of sediment-bearing gravity flows and geological implications	89
5.1 INTRODUCTION	89
5.2 METHODOLOGY	92

5.2.1 Experimental set-up and parameters	92
5.2.2 Experimental approach	94
5.2.3 Data processing.....	95
5.2.3.1 Acoustic Doppler Velocimetry.....	95
5.2.3.2 Focus Beam Reflectance Measurement	96
5.2.3.3 Sediment data processing.....	99
5.3 RESULTS	102
5.3.1 Visualisation.....	102
5.3.2 Velocity data	102
5.3.3 Sediment suspension profiles.....	111
5.3.4 Sediment data.....	112
5.4 DISCUSSION	113
5.4.1 Criteria for the generation, and depositional structure of single-pulsed flows	113
5.4.1.1 Advection of the body fluid towards the flow fronts in single-pulsed flows, with relevant timing threshold between pulses	115
5.4.1.2 Single-pulsed flow deposits.....	116
5.4.2 Multi-pulsed flows.....	118
5.4.2.1 Conceptual model of multi-pulsed flow dynamics and deposition	119
5.4.2.2 Limitations of the conceptual model and experimental methodology	124
5.5 CONCLUSIONS	125
Chapter 6: Discussion and Conclusions.....	127
6.1 COMPARISON OF THE DYNAMICS OF SALINE AND SEDIMENT-BEARING MULTI-PULSED FLOWS.....	127
6.1.1 Longitudinal variation in velocity structures	127
6.1.2 Dynamics of the second pulse within a multi-pulsed flow.	127
6.2 MERGING LENGTHS IN MULTI-PULSED FLOWS.....	129
6.2.1 Multi-pulsed turbidite deposition with possibility of erosion and bypassing	130
6.2.2 Flows generated on slopes	132
6.2.3 Multi-pulsed flows comprised by two initial flow components of different compositions and volumes	133
6.3 MULTI-PULSED TURBIDITE DEPOSITIONAL MODEL AND APPLICATION	134
6.4 CONCLUSIONS	137

6.4.1 Summary of observation from experimental data137

6.4.2 Suggestions for future research139

References141

Appendix A158

Appendix B161

LIST OF FIGURES

Figure 2.1 - Feedback loop for the autosuspending of particulates in suspension currents (after Pantin, 1979). 10

Figure 2.2 - Turbidity currents generated by downwelling. 12

Figure 2.3 - Bouma sequence (modified after Shanmugam, 1997). 16

Figure 2.4 - A schematic diagram of gravity currents. 19

Figure 2.5 - The head of a gravity current modelled at laboratory scale (scale bar in centimetres is shown). 21

Figure 2.6 - Different density profiles (Kneller & Buckee, 2000); A) Two-layer profile, B) Smooth profile, C) Stepped profile, D) Uniform profile. 22

Figure 2.7 - Representation of 2D flow structure (adapted from Lowe et al., 2002). 22

Figure 2.8 - The ratios of measured and predicted current lengths as a function of time (adapted from Huppert & Simpson, 1980). 26

Figure 2.9 - Two gravity currents with different interstitial fluids (adapted from Gladstone & Woods, 2000); A) Interstitial and ambient are water, B) Interstitial fluid is saline and C) Conceptual models of the two cases. 27

Figure 3.1 - Schematic sedimentary log of a turbidite with intervals of inversely graded grain size. Inverse grading in pulsed deposits is distinct from basal inverse grading, which can be produced by other mechanisms (e.g., Hand, 1997). Note: S = Silt; VF = very fine sand; F = fine sand; M = medium sand; C = coarse sand; VC = very coarse sand; G = granules. Mudstone clasts and hemipelagites are not always present. Relative thicknesses of individual intervals of the deposit depend on compositions of sediments and the timescales within which the intervals are deposited. 31

Figure 3.2 - Schematic of the experimental set up. A 5 m-long flume with two lock boxes (each 0.125 m long) set up in series at one end to enable the delayed release of a second pulse to generate a pulsed flow. Two overspill boxes were used to reduce the effect of returning waves associated with slumping of dense fluids in the lock boxes. Acoustic-Doppler Velocimetry (ADV) was used to collect velocity data at successive downstream positions located at 0.365, 0.465, 0.585, 0.675, 0.765, 0.865, 0.965, 1.065, 1.265, 1.465, 1.665 and 1.865 m. 34

Figure 3.3 - Photographs of the flow at different time intervals for A) a single-pulsed flow experiment with 0 second delay time and B) a multi-pulsed flow experiment with 4 second delay time between two pulses. In (B) the two pulses completed merged between 15 s and 18 s. Gridlines on the bottom of the flume were used for camera alignment and flow position tracking. Inset shows the advection of the second pulse within the first pulse. 36

Figure 3.4 - Plots showing the location of the front of A) a single-pulsed and B) a multi-pulsed flow over time. Dashed curves are best fits of front position data collected from multiple experiments. 39

Figure 3.5 - Contour plots showing spatio-temporal variation of internal velocity structure within A) a single-pulsed flow and B) a multi-pulsed flow at 0.365 m, 0.675 m, 0.865 m, 1.265 m and 1.665 m downstream from the back of the lock box. Red and blue lines between plots indicate the arrivals of the primary and secondary pulses, respectively; these become progressively closer with time in multi-pulsed flows. Note that the low velocity variations that appear as vertical stripes of amplitude ($< 0.025 \text{ ms}^{-1}$) show the effect of surface waves, white horizontal stripes in each subplot are areas of no data. 40

Figure 3.6 - Contour plots showing spatio-temporal variations of depth-averaged velocity of A) Single-pulsed flows and B) Multi-pulsed flows. Note: Dashed and dotted curves are best fits of front positions of primary and secondary pulses respectively. 42

Figure 3.7 - Comparison between depth-averaged velocity profiles of single- and multi-pulsed flows at three different downstream positions: A) Raw data and B) Filtered data. Note: Raw data were filtered by using Savitzky-Golay smoothing process in MatLab with a polynomial order of three and a framelength of 151. 43

Figure 3.8 - Model of multi-pulsed flow propagation based on experimental results. Vertical axis shows flow height (h), horizontal axes show density (d) and velocity (v). Note: The model illustrates the scenario in which the second pulse intrudes into the first pulse at neutrally buoyant level (see text for discussion of alternative scenarios). 44

Figure 3.9 - Conceptual models illustrating the depth-averaged velocity-time profile for various turbidity current configurations and their inferred deposits. A) A single-pulse turbidite with an upward fining grain size profile. B) Stacked turbidites comprising two single-pulsed turbidities with a presence of Bouma Te (silt or clay layer) in between. C) Amalgamated turbidite with sharp interface between different inverse-to-normal grading cycles due to the erosion of a latter flow into the deposit of an earlier flow. D) Pulsed turbidites at relatively proximal and distal locations. Note: 1) the lack of linear correspondence between the time and depth records (shown schematically for Fig. 3.9A, and implied for Fig. 3.9B-D); 2) pulsed turbidites might have internal erosion surfaces instead of (or in addition to) inverse grading depending on pulse strength. 49

Figure 3.10 - Initiation mechanisms of multi-pulsed flows: A) Multi-pulsed flow triggered by retrogressive slope failures and conceptual turbidite patterns for

longer vs. shorter failure delays in the left-hand and right-hand panels, respectively and B) Tri-pulsed flow triggered by flow combination at channels, and possible turbidite grading patterns. 50

Figure 3.11 - Multi-pulsed turbidites A) offshore Sumatra at the 4MC and 2MC core locations (modified after Sumner et al., 2013), dashed curve shows proposed channel conduit, unit of grain size is μm ; and B) in the linked Juan de Fuca and Cascadia channels at the 12PC and 25PC locations (modified from Gutiérrez-Pastor et al., 2013), white curve shows channel conduit (Goldfinger et al., 2016). Note: because grain size was estimated directly from the core, sediments finer than $62 \mu\text{m}$ cannot be distinguished (A). Magnitude of magnetic data reflect grain size of turbidites. Bathymetric data were taken from GebCO, 2014. 53

Figure 4.1 - A) Sketch of experimental set up (modified from Ho et al., 2018a). Note: i) three arrows sketched along the top of the flume indicate positions of ADV/siphoning instrumentation, ii) two cameras were set up on a track fixed in front of the flume, iii) initial flow height $h=0.05 \text{ m}$ (see vertical scale bar). B) Flow propagation model with lock length, L , merging length, l_m , and total merging length, L_m , highlighted. 60

Figure 4.2 - Front positions of some flows plotted based on different ambient heights A) 0.1 m, B) 0.125 m, C) 0.167 m and D) 0.25 m. Note: symbols on plots highlight points of merging in each experiment. 66

Figure 4.3 - Time-series velocity (contour fields) and density (contour curves) data collected from experiments of A) single-pulsed flow, B) short delay flow and C) long delay flow, in which $L = 0.125 \text{ m}$, $H = 0.25 \text{ m}$, $h = 0.05 \text{ m}$. Note: i) contour curves show excess density in percentage, ii) vertical stripes indicate the effects of surface waves of small magnitude, iii) the x value shown on each plot indicates the position along the flume where the ADV/siphoning data were taken. 73

Figure 4.4 - Data regression showing merging length as a linear function of initial dimensionless parameters, obtained using Matlab'sTM numerical nonlinear data-fitting solver, lsqnonlin. Note: $R^2 = 0.96$, RMSE = 6.8%. 74

Figure 4.5 - Contour plot showing variation of RMSE of different data fitting, Equation 5.11, resulting from varying A and B within 0-1. 77

Figure 4.6 - Conceptual models of the intrusion of the second pulse in A) short delay time flows (modified from Ho et al., 2018a) and B) long delay time flows. Note: h , v and d denote flow height, velocity and density; in (B) i) the nose of the secondary pulse is lifted off the bed, ii) the dilute cloud remnant flow from the first pulse above the second pulse. 78

Figure 4.7 - Probability distribution plots of recorded natural flow height and concentration A) conditional density plot showing the density of co-occurrence of different flow heights and concentrations between the considered empirical data, B) cumulative density function of flow height and C) cumulative density function of concentration. Note: i) different colours indicate numbers of occurrence of a flow height at a given concentration, ii) red crosses indicate empirical values of flow height and concentration (data used in this calculation are provided in Appendix A), iii) dashed line shows non-linear correlation between flow height and

concentration. 81

Figure 4.8 - Probability distribution and cumulative functions of normalized merging lengths $\frac{l_m}{\sqrt{L}}$ computed at delay time $\Delta t = 10 \text{ mins}$ 83

Figure 4.9 - Parametric analysis of merging length scales on the variations of lock length, flow height, delay time and concentration, equation (4.11), in which all but the selected parameter retained their values in Table 4.4, whilst the selected parameter were varied. Note: blue dots indicate the merging length cited in the example (see text and Table 4.4). 84

Figure 4.10 - Diagram showing maximum lengths of lock that can produce a multi-pulsed gravity current for different combinations of flow height and delay time between successive releases (see text for discussion). 85

Figure 5.1 - Experimental set-up. Note: i) ADV/FBRM data were collected at $x=1.7 \text{ m}$, 2.7 m and 3.7 m centered at midpoint of offset between the two probes, ii) sediments were sampled at $x=0.7 \text{ m}$, 1.7 m , 2.7 m , 3.7 m and 4.7 m and iii) the back of the second lockgate (i.e., right end of the flume) starts at 0.15 m position so the absolute distances between sampling positions and source are $x - 0.15 \text{ (m)}$ 92

Figure 5.2 - Grain size distribution and grain shape data of sediments in the lockboxes used in the experiments (measured via laser diffraction granulometry method, using a Malvern 2000e grainsizer). 93

Figure 5.3 - FBRM technique A) schematic layout of internal structure of a FBRM probe, B) cross section of the measuring window, the focused beam travels along a circular path, C) measuring of chord length distribution of sediments entering the measurement vicinity and D) Chord length as a function of particle diameter, laser beam is exaggerated as being a straight line upon travelling through the particle in the figure (modified after Wynn, 2003; Mettler-Toledo, 2013). 96

Figure 5.4 - Steps in the conversion between CLD and PSD data. 97

Figure 5.5 - Steps conducted to process SEM images to produce grain size grading data.101

Figure 5.6 - The evolution of single-pulsed flow (0 s delay time).....103

Figure 5.7 - The evolution of 2.5 s delay time flow.104

Figure 5.8 - The evolution of 8 s delay time flow.105

Figure 5.9 - ADV data showing variation in velocity field of A) single-pulsed flows, B) 2.5 s delay time flows and C) 8 s delay time flows. Note that the experimental set-up in which two laterally offset ADV probes were deployed results in a stitching artefact such that the flows arrived at the upper probe first, then at the lower one 2 s later.106

Figure 5.10 - Depth-averaged velocity of A) 0 s delay time flows, B) 2.5 s delay time flows and C) 8 s delay time flows. Note that effects of surface waves are indicated by the fluctuation of data, especially during waning phases. However, the magnitudes of the waves are relatively small compared to the flow velocity (see

e.g., Chapter 3).107

Figure 5.11 - Real time particle size distribution at 2 cm height of A) single-pulsed flows, B) 2.5 s delay time flows and C) 8 s delay time flows. Note: the reduction in proportions of mean grainsize at 22-25 s, $x=1.85$ m for the 2.5 s delay time flow and that within 34-46 s, $x=1.85$ m for 8 s delay time flow are interpreted as a result of technical glitch.108

Figure 5.12 - Vertical grading profiles of deposits of single-pulsed (2.5 s delay time) and multi-pulsed (8 s delay time) flows collected at 0.7 m, 1.7 m, 2.7 m, 3.7 m and 4.7 m.109

Figure 5.13 - Standard deviation of grain sizes.110

Figure 5.14 - Sketch of single-pulsed flow at an initial stage within which the dense fluids in each lockbox starts to collapse: A) when the second pulse component was released, B) at a time after the delay time. Note: dashed lines indicate that the lock gates have already been withdrawn, in this particular setting the delay time is non-zero but smaller than the relevant threshold (see text for discussion of this upper limit), rectangle highlights the mixing of fluid portions from each pulse components which make up the single-pulsed flows body.116

Figure 5.15 - Comparison between two data sets of grain size distribution analysed using the same control mixture of sediments; such control mixture is representative of the composition of sediments used in the lockboxes. Note: i) analysis using laser diffraction granulometry method, blue curve (by deploying Malvern 2000e), ii) analysis using FBRM measurement and inversion, red curve and iii) this plot indicates that the reliability of the inversion algorithm is acceptable.....117

Figure 5.16 - Conceptual model describing the deposition of multi-pulsed flows: A) Shortly after second pulse release, B) Approaching the point of merging and C) Beyond the point of merging. Notes: i) three conceptual density/velocity profiles account for the dynamics at the second flow front at three characteristic timescales, ii) the same density/velocity and height axis scheme applies for all three plots and iii) dashed lines in velocity/density models indicate positions of velocity maximum.....120

Figure 6.1 - Conceptual model of the longitudinal variation of turbidite deposition. Note: i) deposit depth and grain size are not drawn to scale, ii) points of depositional transition indicate where single-pulsed turbidites start to be deposited and iii) dashed line indicates the distance prior to points of merging within which single-pulsed turbidites might be deposited.136

LIST OF TABLES

Table 4.1 - Experimental parameters conducted to underpin a scaling analysis.	64
Table 4.2 - Dimensionless parameter groups.	64
Table 4.3 - Repeated experiments and error analysis.	68
Table 4.4 - Calculated merging lengths for multiple canyon head scale failures.	82

ABBREVIATIONS

ADV – Acoustic Doppler Velocimetry
CLD – Chord length distribution
FBRM – Focus Beam Reflectance Measurement
PSD – Particle size distribution
UVP – Ultrasonic Velocity Profiling
SEM – Scanning Electron Microscope

Chapter 1

Introduction

1.1 AIMS, OBJECTIVES AND OVERVIEW OF THE RESEARCH

Gravity currents are formed by the intrusion of dense fluids into less dense ambient fluids; such density-driven flows are widespread in both natural settings and industrial scenarios (Middleton, 1993; Simpson & Britter, 1979; Simpson, 1982; Dasgupta, 2003). Turbidity currents are a form of dilute sediment-bearing gravity flow. They are common in submarine environments, where they are known to transport clastic sediments from the continents to the deep seas, building some of the largest geomorphological features on the planet (Shanmugam, 2002; Khripounoff et al., 2003; Johnson et al., 2017). Turbidity currents can be triggered by submarine slope failures due to earthquakes, direct discharges of sediments from fluvial systems into the oceans or other mechanisms (Heezen & Ewing, 1955; Pharo & Carmack, 1979; Weirich, 1989; van de Berg et al., 2002; Strachan, 2008; Meiburg & Kneller, 2010; Talling, 2014; van de Berg et al., 2017). Studying the dynamics of turbidity currents, directly, or via their deposits, turbidites, has become an important research topic, as such currents can evolve extensively into deep oceans and last for hours or days and cause significant damage to submarine infrastructure (Piper et al., 1988; Xu et al., 2004; Mikada et al., 2006; Sumner & Paull, 2014; Talling et al., 2015). The Grand Banks 1929 seismic event in the Laurentina Slope Seismic Zone is a well-studied example of turbidity current spatial and temporal scales; the associated seismically initiated gravity current, transformed from an initial debris flow (Piper & Normark, 2009), lasted for at least 12 hours and deposited a considerable amount of sand in the deep ocean that was eroded from the continental slope (Piper et al., 1999). In addition, up to 12 submarine cables were damaged by the current within a few hours of the earthquake (Talling et al., 2013). Turbidite deposits are thought to act as proxies for flow dynamics and thus can be interpreted to indicate flow initiation mechanisms (Kneller & McCaffrey, 2003; Sequeiros, 2012). The interpretation of

sequences of seismically generated turbidite units can be used to support the analysis of earthquake reoccurrence (see e.g., Gutiérrez-Pastor et al., 2013).

In order to interpret turbidites, grading analysis is commonly conducted under an assumption that suspended sediments within a turbidity current aggrade progressively from the overpassing flow (see e.g., Goldfinger et al., 2003; Basilici et al., 2012). Commonly, turbidites are seen with a classic upward-fining grading profile referred to as normal grading (Bouma, 1962; Lowe, 1982; Gutiérrez-Pastor et al., 2013) and are thought to be deposited by turbidity currents with normal waxing-waning velocity structures (see e.g., Kneller & Branney, 1995; Kneller & McCaffrey, 2003; Amy et al., 2005; Basilici et al., 2012) during the depositional phase. However, it is not uncommon for turbidites to show deviations from the classic upward fining structures; such as multiple intervals of inverse-to-normal grading within one turbidite unit (see e.g., Kuenen & Menard, 1952; Gutiérrez-Pastor et al., 2013). These complex deposits are termed multi-pulsed turbidites and are interpreted as being deposited by multi-pulsed turbidity currents whose velocity structures show cycles of waxing and waning; such flows likely transition to become monotonically varying. Hence, flow dynamics and longitudinal structures of the deposits vary along depositional pathways. The coarsening-upward depositional feature of note here is different from the inverse grading commonly observed at turbidites bases which could be a result of traction carpet action, the incorporation of mud clasts at the flow base or simply grain size fractionation within the flow (Hand, 1997; Sohn et al., 2002; Talling et al., 2015). Multi-pulsed flows comprising two or more flow components (i.e., waxing-waning cycles) can be generated by retrogressive slope failures during which each slumping episode leads to the formation of one flow component (Goldfinger et al., 2012), or as a result of a combination of multiple single flows at downstream confluences that were initially generated in separate upstream channels (Nakajima & Kanai, 2000). In addition, multi-pulsed flows can sometimes be initiated by the variations in the flux of flood discharges into oceans (Mulder & Alexander, 2001) or a combination of multiple river inputs (Ismail et al., 2016).

To date, multi-pulsed turbidity current dynamics have not been a research focus and thus there is a need for an in-depth understanding both of the dynamics of such flows and also of their depositional structures. Although multi-pulsed turbidity flows have been inferred to occur in deep ocean environments based on field-based studies of turbidite deposits (see e.g., Gutiérrez-Pastor et al., 2013), the dynamics of associated flows were not directly deduced from the grading data of the studied deposits. Also, studying in-situ the dynamics of submarine seismically initiated multi-pulsed turbidity currents can be difficult and problematic as such flows occur in the deep oceans, are rare, and can be destructive (see e.g., Puig et al., 2003; Babonneau et al., 2010; Sumner & Paull, 2014). Therefore, conducting experimental research to model multi-pulsed flows at laboratory scale can usefully help to develop insight into the flow dynamics and associated depositional structures at prototype scales.

The principal aim of this research is to explain the linkages between flow dynamics, and depositional structures, of multi-pulsed turbidity currents. Specific research objectives are as follows: i) demonstrate the differences in dynamics of single- and multi-pulsed saline gravity flows; ii) examine the scaling between laboratory and full-scale multi-pulsed flows; and iii) validate the hypothesis that multi-pulsed turbidites are deposited by associated multi-pulsed flows and that grading patterns deposits vary along channel pathways, given that waning and waxing phases during the flows' evolution suggest upward-fining and upward-coarsening depositions respectively (Kneller & Branney, 1995; Kneller & McCaffrey, 2003; Amy et al., 2005). Overarching questions arise as to whether signals of multi-pulsed flow initiation mechanisms can be carried by the flow deposits and how far from sources such signals will persist.

In order to achieve the outlined objectives, experimental research was conducted in which both compositionally-driven and particulate-laden single- and multi-pulsed flows were modelled. The research was subdivided into three laboratory components: i) modelling of saline flows to examine the difference in dynamical variations during the evolution of single- and multi-pulsed flows; geological implications for turbidite deposition can be suggested based on these

experimental data, ii) studying the dependency of the merging phenomenon on initial conditions and iii) modelling sediment-laden flows to compare depositional structures of sediments deposited by single- and multi-pulsed turbidity currents. Experimental data show that for the chosen configurations, two flow components within a multi-pulsed flow eventually merge at some distance from source to form a uni-pulsed flow.

As part of the first work component, in order to underpin the comparison of flow dynamics between single- and multi-pulsed flows, visualisation detailing the spatio-temporal evolution of the flows was conducted using high definition (HD) interlinked cameras. In particular, such data were used to examine the differences in the evolution of the flow fronts during slumping and inertial phases of flow evolution. Also, streamwise, high-frequency velocity and density data were collected using Acoustic Doppler Velocimetry (ADV) and a direct sample siphoning technique, respectively. The data provide insight into the variations of internal velocity and density of single- and multi-pulsed flows. It will be shown that the experimental data confirmed that pulses within the modelled multi-pulsed flow progressively merged and eventually a unified flow was formed. Therefore, the deposits of multi-pulsed flows are interpreted as being multi-pulsed up to the point of merging and becoming single-pulsed thereafter. The signals of flow initiations are expected to be distorted progressively up to the point of merging. Based upon this observation, a model to explain the evolution of multi-pulsed flow has been generalised and the interpretation of multi-pulsed turbidites observed in real world settings can be reviewed and broadened.

To support the second part of the research, a series of saline multi-pulsed flows in which initial parameters were systematically varied was conducted in order to study the merging phenomenon under a wider range of flow conditions. This work permitted an analysis of the dependence of merging lengths, measured as the distance between source and points of merging, on initial parameters; such analysis can be used to estimate the spatial persistence of multi-pulsed turbidites. A numerical analytical approach was deployed to seek a mathematical correlation upon which examples of possible real world merging lengths were given and

discussed. The scaling analysis provided a useful tool in the estimation of the persistence of multi-pulsed turbidites deposited following short-duration, closely-spaced submarine slumping initiation events. The assumptions underpinning this analysis prevent its direct application to predict merging length scales in pulsed flow generated in confluence settings.

In the third part of the research, single- and multi-pulsed sediment-bearing flows were modelled. Experimental approaches included i) velocity sampling using Acoustic Doppler velocimetry (ADV), ii) examining sediment distributions at a given point within the flows using Focus Beam Reflection Measurement (FBRM) and iii) collecting deposit samples at multiple positions to analyse the variations in vertical depositional structures of the flows. Experimental data confirm that the pulse merging phenomenon occurs in particulate as well as saline flows, but suggest that although multi-pulsed turbidites are deposited relatively proximal to source, such deposition may cease well before the point at which pulses merge. This observation suggests that interpretations of the lengthscales to which multi-pulsed turbidites might persist from source in prototype environments – based on analysis of the first and second laboratory work components - are likely overestimates, assuming that these experiments are good proxies for natural scale flow initiation and development. Nevertheless, turbidites found beyond points of merging always exhibit a normal grading profiles and thus cannot carry signals of flow initiation mechanisms. The early shredding of flow initiation signals can be accounted for by the variation in flow dynamics and/or limitations of the experimental configurations deployed in the research.

The experiments in this research were conducted to study the dynamics of multi-pulsed flows generated by two fluid components initially contained within a series of two lockboxes. Such a configuration models only the generation of multi-pulsed turbidity currents initiated by short, sequential breaches in low-gradient prototype environments. However, experimental data may also provide qualitative insight into the dynamics of multi-pulsed flows generated in confluence settings.

1.2 THESIS OUTLINE

The thesis is structured in 6 chapters:

Chapter 1: An introduction to the project, aims, objectives, experimental methodologies, brief overview of the results of this research and the outline of the thesis.

Chapter 2: A literature review providing the theoretical background for the research and an overview of the experimental methodologies deployed to study the dynamics and deposition of turbidity currents.

Chapter 3: A comparison of the dynamics of multi-pulsed and single-pulsed gravity currents and the geological implications based on a series of saline flow experiments. In this chapter, it is proposed that multi-pulsed turbidite can persist up to the points where two flow components comprising the overpassing multi-pulsed flow merge. Therefore, signals of flow initiation mechanisms can be preserved up to points of merging. A version of this chapter is published in *Sedimentology*; see **Ho, V.L., Dorrell, R.M., Keevil, G.M., Burns, A.D. and McCaffrey, W.D.** (2018) Pulse propagation in turbidity currents. *Sedimentology*, **65**, 620-637.

Chapter 4: This chapter expands on the work detailed in Chapter 3 to study the merging phenomenon in multi-pulsed saline flows under a wider range of initial flow conditions; this new body of work supports a scaling analysis that can be used to estimate the spatial persistence of multi-pulsed turbidites in prototype environments. A manuscript incorporating this chapter is published in the *Journal of Geophysical Research: Oceans*; see **Ho, V.L., Dorrell, R.M., Keevil, G.M., Burns, A.D. and McCaffrey, W.D.** (2018) Scaling analysis of multi-pulsed turbidity current evolution with application to turbidite interpretation. *J. Geophys. Res. Oceans*, **123**, 2017JC013463. The supplementary material of the manuscript is used in Appendix A of this thesis.

Chapter 5: This chapter reports on experiments of dilute, sediment-bearing subaqueous gravity flows (turbidity currents) which were designed to assess whether the pulse merging phenomenon observed in saline flows also occurs in

flows of this type. In addition, study of representative deposits of such flows (turbidites) was conducted to assess whether the passage of single- vs multi-pulse flows leaves a depositional record in terms of uni- vs. multi-pulsed turbidites. The chapter incorporates development of conceptual models of the dynamics and deposition of sediment-bearing multi-pulsed flows and considers the limitations of the experimental set-up in allowing such models to be applied to prototype environments.

Chapter 6: An overall discussion of dynamics and deposition of multi-pulsed flows in prototype environments and conclusions of the study. Suggestions for future research are provided as to outline possible directions to broaden the understanding of multi-pulsed flow dynamics and deposition.

Chapter 2

Literature review

2.1 INTRODUCTION

In this chapter a review of experimental research conducted on lock-exchange gravity currents is presented, with a focus on turbidity currents and their deposits, tied to a review of the turbidity current phenomenon. In order to summarise relevant literature, the following are discussed: i) definitions of different subtypes of gravity flows, ii) turbidity currents, their initiation mechanisms and deposits, iii) structures and dynamics of gravity currents and iv) experimental techniques deployed to study the flow dynamics. Section 2.2 includes a review of the terminologies used to refer to different types of gravity currents plus a review of the mechanisms by which the currents are driven. Sections 2.3 to 2.5 provide the main theoretical background upon which the research conducted within the scope of this thesis is based.

2.2 DEFINITION AND CLASSIFICATION OF GRAVITY CURRENTS

Gravity currents, also referred to as density or buoyancy flows, result from the different relative buoyancy between the flow and ambient fluids. Such buoyancy arises from differences in composition, concentration, temperature or a combination of these factors (Rottman & Simpson, 1983; Middleton, 1993). Such currents can generally be subdivided into two types: i) compositionally-driven and ii) sediment-bearing flows. Compositionally-driven gravity flows arise due to the difference in fluid density between the flow and ambient fluid; where suspended sediments contribute to the density excess, such gravity currents are classified as particulate-laden flows. Sediments within particulate flows are moved by gravitational forces; and their motion, in turn, exerts a movement on the interstitial fluids (Middleton, 1993; Hallworth et al., 1996; Baas et al., 2005; Piper & Normark, 2009). The suspension, and transportation, of sediments within

particulate-laden flows are thought to be controlled by four main mechanisms including i) fluid turbulence (turbidity currents), ii) upward movement of interstitial fluids (fluidised sediment flows), iii) grain interactions (grain flows) and iv) matrix strength in suspended particles (debris flows) (see e.g., Middleton & Hampton, 1973; Simpson, 1982; Middleton, 1993). However, particle support mechanisms might work in combination with different relative degrees of importance in different parts of the flow (see also below; e.g., Kneller & Buckee, 2000; Mulder & Alexander, 2001). Indeed, such classification was solely based on particle-supported mechanisms and was criticised by Dasgupta (2003) who argued that interstitial fluids in particulate-laden gravity flows play a more important role than just being inactively moved under the action of suspended sediments. As such, the role of interstitial fluids seemed to have been underestimated previously (see Middleton & Hampton, 1973). In particular, the whole fluid-sediment mixtures of debris flows move en masse and therefore the fluid components have some effects on the dynamics of debris flow. Reviews on particulate density currents have been conducted by many authors. Huppert (2006) provided a review on viscous, compositional-driven, particulate-laden and highly concentrated gravity flows. Because of the use of small particles in their experiments, granular flows of the type reviewed by Huppert (2006) compare most naturally to the grain flow classification proposed by Middleton & Hampton (1973).

Sediment-bearing flows in which materials are carried by fluids (other than pyroclastic flows, see below) are subdivided into cohesive (i.e., debris flows), hyperconcentrated, concentrated and turbidity currents, based on sediment concentration (Mulder & Alexander, 2001). In this thesis, the term 'current' is used interchangeably with 'flow', rather than specifically referring to surge type flows whose initial volumes are fixed (cf. Mulder & Alexander, 2001). Several researchers define turbidity currents as particulate gravity currents in which sediments are in suspension within the interstitial fluid due to fluid turbulence only. For submarine turbidity currents, such fluid turbulence is generated mostly by shearing, at both the upper and lower boundaries of the currents (Sohn et al.,

2002). Kneller & Buckee (2000), however, raised an argument that it is not always straightforward to determine sediment-suspension mechanisms in natural turbidity currents and that a combination of some mechanisms likely operates within one single flow; they redefine gravity currents as 'flows induced by the action of gravity upon a turbid mixture of fluid and suspended sediment, by virtue of density difference between the mixture and the ambient fluid' (Kneller & Buckee, 2000). When the interstitial fluid is a gas, such as air, examples of suspension currents include pyroclastic currents and powder snow avalanches. The term 'autosuspension' (*sensu* Bagnold, 1962; see e.g., Middleton & Hampton, 1973) is used to describe a feedback loop, as shown in Fig. 2.1 below. This term is deployed to explain the mechanism by which turbidity current movement is maintained. The movement of turbidity currents is driven by density difference between the ambient and particulate-fluid mixture; the excess density is maintained by the suspension of sediments within the interstitial fluid which might or might not be identical to the ambient fluid. Such particle suspension is in turn generated by the turbulence resulting from the movement of the current. The movement of turbidity currents downslope then maintains fluid turbulence within the flows. That means turbidity currents sustain for as long as the sediments suspended within the flows due to turbulence have not been deposited entirely and seafloor gradients are sufficiently high to maintain the movement which keep the flows in turbulence (Pantin, 1979; Parker et al., 1986; Meiburg & Kneller, 2010).

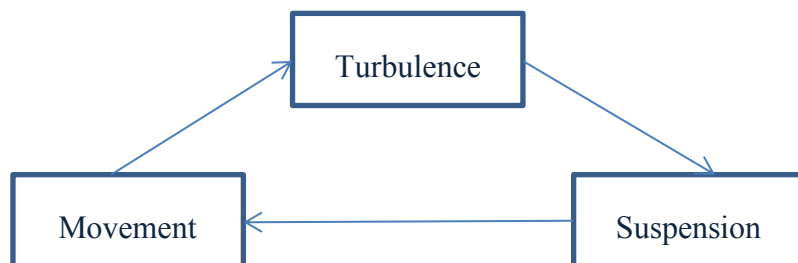


Figure 2.1 - Feedback loop for the autosuspending of particulates in suspension currents (after Pantin, 1979).

2.3 TURBIDITY CURRENTS AND TURBIDITES

2.3.1 Triggering mechanisms

As discussed in section 2.2, turbidity currents are referred to as suspension-driven gravity currents in which the suspension of particles results from the forward movement of the currents (Huppert, 1998; Meiburg & Kneller, 2010). Such currents are principal agent that transports clastic sediments to deep sea environments and build extensive submarine landforms (Simpson, 1982; Canals et al., 2004; Carter et al., 2012; Lintern et al., 2016). Their initiation requires a mechanism and a sufficient gradient to maintain the flow during its early history (Piper & Normark, 2009). Turbidity currents can be generated due to i) earthquake- and autogenically-triggered landslides, ii) discharges of highly-concentrated particle flows (i.e., flows sourced from fluvial systems), iii) overloading of sediments on delta fronts, iv) oceanographic processes (i.e., tides and storms that can lead to the formation of underflows, see text below for description) and v) breaching whereby medium to densely packed sands on steep slopes collapse due to an increase in pore water pressure (Heezen & Ewing, 1952; Hallworth & Huppert, 1998; Piper et al., 1999; van Den Berg et al., 2002; Puig et al., 2004; Waltham, 2004; Gilbert et al., 2006; Tappin, 2010; van Den Berg et al., 2017). Duration of turbidity currents depends on the type and strength of associated triggering mechanisms (Huppert, 1998) but generally such durations can extend up to hours or days though they may be much shorter (see e.g., Piper et al., 1999; Khripounoff et al., 2003; Xu et al., 2004; Mikada et al., 2006; Hughes Clarke et al., 2012; Johnson et al., 2017).

Submarine slope failure is the most important mechanism in the generation of turbidity currents and such failures of sediments are commonly caused by earthquakes and slope oversteepening (Goldfinger et al., 2003; Hughes Clarke et al., 2012; Bernhardt et al., 2015). The main focus of this thesis is on seismically triggered turbidity current dynamics and their deposits. The Grand Banks turbidity current in 1929 is a well-studied example of a flow initiated by failure of slope sediments on steep gradients, with the resultant large muddy

debris flow transforming into a dilute sediment-suspension flow (see e.g., Heezen & Ewing, 1952; Piper & Savoye, 1993). Although the Grand Banks event began with a failure on an open slope, research has suggested that canyon-related failures is more common in prototype environments and associated turbidity currents might be confined within channels (see e.g., Driscoll et al., 2000; Sultan et al., 2007). Indeed, field-based research has been conducted to examine submarine slope failure mechanisms by which submarine sediment-bearing flows are commonly initiated with a highlight that landslides at canyon heads are a typical example of this mechanism.

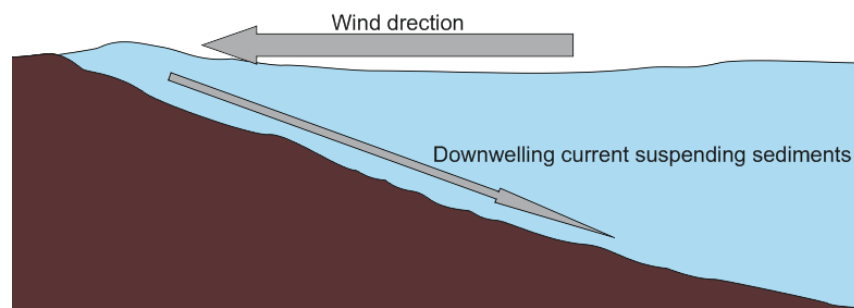


Figure 2.2 - Turbidity currents generated by downwelling.

A second triggering mechanism is direct discharges of fluvially-sourced highly-concentrated sediment flows into lakes or oceans; such events can occur due to intensive rainfalls. The associated underflows are denser than the ambient and propagate along the bottom of seafloors; they are termed ‘hyperpycnal flows’. Turbidity currents initiated by these processes can last up to a few days depending on hydrographical variation of the sources (Piper & Normark, 2009). Turbidity currents can also be initiated by oceanographic processes (e.g., tides and storms) and other mechanisms. For example, oceanic tides result in the resuspension of bottom muddy sediments and thus the formation of turbidity currents (Puig et al., 2004; Johnson et al., 2017). Near river mouths, direct discharges of high-concentration particle plumes can deposit muddy materials in the form of fluid muds which will then be resuspended under the action of tides and waves (e.g., Piper & Normark, 2009; Meiburg & Kneller, 2010). Turbidity currents formed by this process deposit muddy sediments further from

continental shelves and eventually into deep seas (Piper & Normark, 2009). In addition, 'downwelling' is a process that leads to the formation of turbidity currents. Strong onshore winds result in the development of superelevated water columns on continental shelves and at shorelines; counterflows then generated along the shelves (see e.g., Palanques et al., 2006; Meiburg & Kneller, 2010; Fig. 2.2), which travel away from shorelines, down to oceans can erode sediments and become autosuspending (Meiburg & Kneller, 2010).

It is necessary to acknowledge that the formation of turbidity currents sometimes appears more complex. In prototype environments, turbidity currents might be formed by the transformation from earlier debris flows which have been initially initiated by earthquakes (Mulder & Alexander, 2001; Sohn et al., 2002; Strachan, 2008). As an attempt to understand this transformation, Felix & Peakall (2006) conducted laboratory research on the formation of turbidity currents from debris flow and suggested that transformations that take place solely due to the dilution on upper layers of debris flows are not efficient. More efficient transformations, which generate turbidity currents of larger spatial and temporal scales, involve some or all of the processes including i) eroding sediments on upper parts of debris flows, ii) "breaking apart the dense underflow, iii) breaking of internal waves and iv) turbulent mixing" (see e.g., Felix & Peakall, 2006). These processes can even take place simultaneously, depending on the density and viscosity of the flows. Despite the fact that turbidity currents might be initiated by this indirect mechanism and also the flow dynamics might be relatively more complex than direct seismically triggered turbidity current dynamics, the flows are still thought to carry flow initiation mechanisms (e.g., Goldfinger et al., 2003; Beeson et al., 2017). In this thesis, the main research question arises as to whether turbidity currents triggered by earthquakes, regardless of the possibility of debris flow transformation, can carry signals of flow initiations.

2.3.2 Turbidites

Turbidity currents are capable of transporting clastic sediments from continents to deep seas and build extensive turbidite systems in submarine environments

(Simpson, 1982; Canals et al., 2004; Xu, 2011; Lintern et al., 2016). A thorough understanding of turbidity current dynamics is particularly crucial in studying sediment transport and associated deposition in deep seas; such understanding can help predict the distribution of turbidite deposits (e.g., Middleton, 1993; Kneller & Buckee, 2000).

Research on field- and laboratory-based turbidity current deposits has sought to establish the linkage between turbidites and the dynamics of overpassing flows dynamics (e.g., Allen, 1971; Simpson & Britter, 1979; Simpson, 1982; Bonnetaze et al., 1993; Hallworth & Huppert, 1998; Darby & Peakall, 2012; Lintern et al., 2016). It is suggested that turbidites with the classic upward-fining grading profiles are commonly deposited by simple turbidity currents with monotonically-varying velocity profiles (e.g., Fig. 2.3; Bouma, 1962; Lowe, 1982). Turbidites deposited at natural scales are commonly characterised by this grading profile. Such classic grainsize patterns are thought to reflect the deposition of associated flows within their waning phase as the flows during their short waxing phases (in comparison to the duration of waning phases) tend to be erosional or deposit layers of upward-coarsening sediments (Kneller & Branney, 1995; Kneller & McCaffrey, 2003). In fact, the deposition of such basal inversely-graded interval within a turbidite has been researched by various authors. Traction carpet development (*sensu* Dzulynski & Sandes, 1962; see also Lowe, 1982) is thought to be one mechanism by which this depositional pattern can be accounted for; as such, coarse sediments within turbidity currents are likely incorporated within a bed layer with high basal shear stress between the layer and channel floor. Such layers are commonly developed beneath a more turbulent layer within which sediments of finer grainsize are carried and is subdivided into a lower frictional interval (sediments are in continuous contact; turbulence is suppressed) and an upper collisional interval (sediments are more mobilised due to shearing between the layer and upper turbulent flow) (Lowe, 1982). Coarsely-grained sediments then aggrade progressively from the carpet and are deposited onto the channel bed, followed by the deposition of finer materials from the upper turbulent layer (see e.g., Lowe, 1982; Sohn, 1997; Dasgupta, 2003; Kneller & McCaffrey, 2003). In

addition, Hand (1997) suggested a mechanism referred to as transport lag of coarsely-grained sediment fractions in order to explain the deposition of basal inverse layers. This model is based on the hypothesis that velocities by which sediments of any grain size class travel streamwise, prior to deposition, are controlled by fluid velocity within the flows. Coarse sediments are carried by a lower, slowly-travelling region of the body which might be lagged behind the front within which finer sediments are suspended. Therefore, prior to the arrival of the coarse sediment fraction at a given point along the channel, early depositional patterns would be inverse grading as fine sediments in the front and the upper region of the body would fall out first. Upon the arrival of the coarse sediments, deposits would become normally graded. Nevertheless, depositional structures of the upper part of turbidites (i.e., other than the inversely-graded base) commonly exhibit some or all of the standard Bouma sequence (Bouma, 1962) and/or the Lowe sequence (Lowe, 1982). Turbidites described as displaying the Bouma sequence are subdivided into four intervals with upward-fining grading profiles. A large scale, well-graded interval of sand and possibly granules (T_a , might be deposited on top of an upward-coarsening basal layer) is overlaid by three intervals of finer sand and silt materials (T_b , T_c and T_d). The upper three intervals might be characterised by different types of bedforms. The deposits are commonly capped by an interval of mud (i.e., incorporated within the depositional flows) or hemipelagite (T_e) (Bouma, 1962; Middleton, 1993; Shanmugam, 1997). Similarly, this sequence of deposits was used by Lowe (1982) who suggested that the bottom massive coarse interval might be absent if the associated turbidity currents are low concentrated. That means, given the range of materials and density of the flows, some or all of the intervals can be exhibited in the deposits.

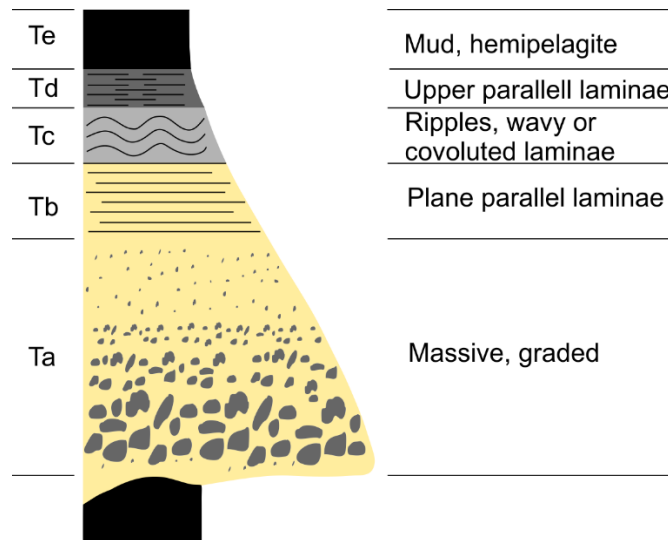


Figure 2.3 - Bouma sequence (modified after Shanmugam, 1997).

Although the majority of turbidites found in the prototype environments commonly exhibit the classic grainsize profile; exceptions have been seen for some deposits, apart from basal inverse grading (see e.g., Kneller & McCaffrey, 2003; Mulder et al., 2003). For example, interrupted graded or reversed beddings (i.e., alternatively termed stacked turbidites) were observed in deposits recovered from deep seas and hypothesised as a result of 'stack' deposition of two turbidity currents along the same channel pathway (see e.g., Kuene & Menard, 1952). As such, the second current built up coarse sediments on top of the fine materials previously deposited by the first current. Also, turbidites deposited in prototype environments sometimes exhibit an upward-coarsening characteristic, for example deposits of this feature have been found in the Cascadia channel system (e.g., Goldfinger et al., 2003) and Lake Challa in Kilimanjaro, Kenya/Tanzania (e.g., Van Daele et al., 2017). Such multi-pulsed turbidites are characterised by the presence of multiple intervals of inverse-to-normal grading within one turbidite unit and are different from basal inverse grading which can be accounted for by other mechanisms as already discussed. Multi-pulsed turbidites can be deposited by multi-pulsed turbidity currents whose longitudinal velocity structures acquire a transition from being initially cyclically waxing-waning to rapidly waxing and then monotonically varying (i.e., the commonly accepted turbidity current velocity

profile). Given that waxing phase suggests upward-coarsening deposition and waning phase suggests the opposite, as discussed, multi-pulsed turbidites are expected to be deposited within the initial waxing-waning phase. Multi-pulsed turbidity currents can be generated by i) retrogressive submarine slope failures (i.e., due to variation in ground shaking pattern of a single seismic event or shock/aftershock events) in which each slumping episode can lead to the formation of a flow pulse (e.g., Piper et al., 1999; Canals et al., 2004; Bull et al., 2009), ii) combination of multiple turbidity currents sourced from different upstream attributes at their downstream confluences (e.g., Nakajima & Kanai, 2000; Ismail et al., 2016), iii) variation in hydrographic discharges of fluvially-sourced sediment-bearing flows into oceans (e.g., Mulder & Alexander, 2001; Best et al., 2005). Delay times between successive submarine failures can be relatively short (i.e., up to 10 mins for earthquake-triggered slumping) or long (i.e., up to hours or days for short/aftershock events). These timescales will be discussed in Chapter 4. In particular, within the scope of this thesis, multi-pulsed flows initiated by retrogressive submarine failures are focused upon and thought to be able to carry signals of flow initiation mechanisms (e.g., Goldfinger et al., 2003). Such signatures might be expressed in the associated depositional structures. As such, the deposits are likely multi-pulsed proximally and eventually become normally-graded. In addition, it is important to estimate the spatial persistence of multi-pulsed turbidites as the question arises as to how far from source initiation signals can be transmitted. Experiments tailored to model retrogressive slumping settings in which the generation of multiple flow pulses and their interaction were enabled are the principle focus of this thesis.

2.4 STRUCTURE AND DYNAMICS OF GRAVITY CURRENTS

2.4.1 Natural vs. lock-exchange gravity currents

Conducting laboratory lock-exchange experiments of gravity currents remains an effective approach in studying the flow dynamics. Such experimental configurations require an initial separation of ambient and dense fluids, using a lock gate, into two compartments within a flume (see e.g., Middleton, 1993;

Nokes et al., 2008). This surge-type flow of fixed initial volume is generated upon releasing the lock gate and maintains a physical structure of three components consisting of a head, a body and a tail (Huppert, 1998; Baas et al., 2005). The first two components are always distinct and well-defined (see Fig. 2.4) whereas a tail exists only in the form of a thin and very dilute layer (Middleton, 1993; Kneller & Buckee, 2000). Lock-exchange flows commonly experience a transition from a rapidly-waxing phase, marked by the arrival of the head, to a slowly-waning phase after the passage of the head at any given point along the channel pathway (Basilici et al., 2012; Talling, 2014; Kneller & McCaffrey, 2003). By way of contrast, sustained or steady-state flows, widely observed in prototype environments, commonly exhibit steady bodies with relatively constant velocity following a similar waxing phase corresponding to the passage of the flow fronts (Kneller & Branney, 1995). Such flows are sustained due to constant influxes of sediments sourced from upstream initiation points, over certain time periods, and thus are considered steady only within such timescales. Therefore, the dynamics of the experimentally-modelled currents of fixed initial volumes do not entirely reflect the dynamics of sustained or steady-state gravity currents. However, since the dynamics of flow heads between two settings are comparable and the dynamics of any gravity current flow front are thought not to be affected by turbulent mixing occurring behind it (i.e., turbulence on the back of the flow front and on the body of the flow; e.g., Simpson & Britter, 1979; Puig et al., 2004; Nokes et al., 2008), lock-exchange gravity flows can still act as proxies for their relatively more sustained counterparts (Kneller & Buckee, 2000). Although lock-exchange flows display a full range of the dynamics of most gravity currents in prototype environments (Hacker et al., 1996), they have better-defined heads and also show a reduction in sedimentation immediately downstream, compared to continuous-supply, steady-state currents which show a more constant profile of horizontal sedimentation (Peakall et al., 2001). This difference is caused by the sudden initial collapse of the dense fluid-sediment mixture in the fixed-volume flow experiments. In this section, the structure and dynamics of gravity flows will be reviewed and discussed, with focus on lock-exchange flows.

In order to study turbidity current dynamics, saline flows are commonly used as proxies at laboratory scales. Although saline flows do not exhibit the effects of sediment settlement during turbidity currents runout, they experience similar phases of flow evolution including i) the slumping phase, ii) an inertial phase and iii) a viscous phase (see Chapter 3). During the first phase, flows modelled on a zero-gradient (i.e., horizontal) slope advance with relatively constant velocity for about 5-10 lock lengths. The flows then start to decelerate within the second phase and further slow down in the viscous phase until they completely stop. When present, coarse sediments are concentrated within the frontal part of the body and in the heads of turbidity currents (Choux & Druitt, 2002; Baas et al., 2005) and deposited progressively as the flows evolve downstream; finer grained (i.e., slower-settling) sediments are considered to be analogous in their behaviour to compositionally-driven currents, i.e., saline flows (Kneller & Buckee, 2000). Based on the assumption of flow initial parameters, gravity currents modelled at laboratory setting can be scaled up to estimate run out lengths of turbidity currents in prototype environments (see Chapter 4).

2.4.2 Gravity current anatomy and mixing processes

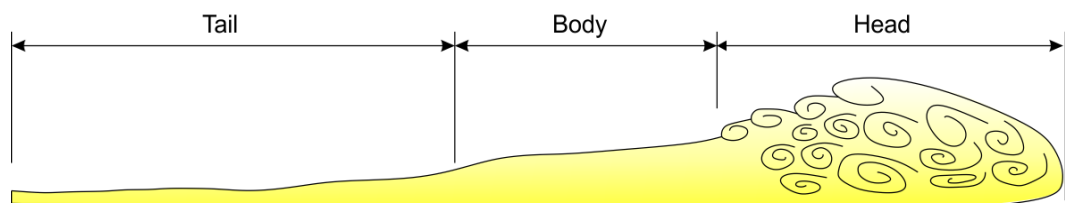


Figure 2.4 - A schematic diagram of gravity currents.

2.4.2.1 The head

The head of a gravity flow is distinct from the rest of the current and characterized by an overhanging nose, greater thickness than the body, and one or a series of turbulent billows at its rear (Britter & Simpson, 1978); see Fig. 2.4. Turbulent mixing between dense fluid and the ambient at the head play an essential role both in the flow's dynamics (Britter & Simpson, 1978). Compared to other parts of the current, the head has a greater thickness, sometimes double that of the

current body (Britter & Simpson, 1981). This increase in the thickness at the head is thought to enable it to overcome frictions on both upper and lower boundaries, in order to advance through the stationary ambient fluid (Middleton, 1993). This also explains the shape of an overhanging nose which overrides and traps some of the ambient fluid.

However, the head is unstable due to two main mixing processes occurring i) underneath the nose and ii) on the back of the head (Hacker et al., 1996). The overridden, less-dense ambient fluid is entrained into the flow front and mixed with the dense fluid. As a result of this entrainment, cleft-lobe patterns enhancing the trapping of ambient fluid are formed on the base of the flow front (see Fig. 2.5). Lobe spacing is proportional to flow thickness (Kneller & Buckee, 2000). However, turbulent mixing in the form of Kelvin-Helmholz billows generated by instability on the back of the head due to upper surface shearing is more significant than the mixing process occurring underneath the nose of the flow. This billow region is sometimes described as a small neck region behind the front (e.g., Middleton & Hampton, 1973). By modelling laboratory brine flows, Kneller et al. (1999) showed that two areas of negative Reynolds stress are associated with the entrainment of overridden fluid underneath the nose and the detrainment of dense fluid in the neck region into the ambient (e.g., Allen, 1971). These two main mixing processes are thought to govern the dynamics of gravity currents at laboratory scales (García & Parsons, 1996). It should be noticed that the effect of fluid entrainment underneath the flow front is not significant for large-scale natural gravity currents (Middleton & Hampton, 1973).

2.4.2.2 The body

The body of a gravity current has a different mass-momentum balance in comparison with that of the head (Middleton, 1993). In contrast to the instability of the head, the body is more uniform in thickness and relatively steady over time. The body can be subdivided into upper and lower layers; the former is denser and moves at a higher velocity, whereas the latter is more dilute as a result of surface mixing with the ambient (Hallworth et al., 1993). Turbulent mixing occurring at

the back of the head does not affect the dynamics of the body as the fraction of dense fluid on the back of the head that is mixed with the ambient is lost into the ambient and thus loses its forward momentum; such fluid fraction ends up being left behind (Lowe et al., 2002). For natural turbidity currents, ambient entrainment at the flow front will keep fine particulates in suspension; such fine particles are circulated towards the body of the flow and remain within the outer layer of the currents (i.e., upper part of the body).

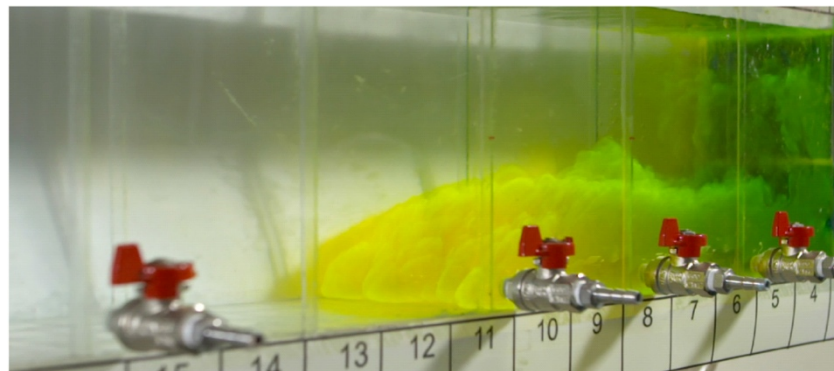


Figure 2.5 - The head of a gravity current modelled at laboratory scale (scale bar in centimetres is shown).

2.4.2.3 The tail

The tail of gravity currents is commonly seen as a very thin, dilute layer of fluid; its thickness is reduced as the flow lengthens over time (Hallworth et al., 1996; de Rooij et al., 1999; Harris et al., 2002). For turbidity currents, the tail bears mainly fine-grained sediments suspended within the flow and indicates the flow waning phase during which its velocity decreases to zero (Sohn et al., 2002; Goldfinger et al., 2003; Kneller & McCaffrey, 2003; Goldfinger et al., 2007; Goldfinger et al., 2008).

2.4.3 Velocity structure and density profile

2.4.3.1 Head advance velocity and internal fluid velocity of gravity currents

A commonly observed vertical velocity profile of gravity currents is shown in Fig. 2.6A. The height of a velocity maximum is controlled by the ratio of drag forces between upper and lower boundaries and normally between 0.2 and 0.3 of the

flow's height (Kneller & Buckee, 2000; Darby & Peakall, 2012; Sher & Woods, 2015). The velocity maximum divides a gravity current into inner and outer regions of opposite velocity gradients. The ratio of thicknesses of the two regions is equal to that of friction coefficients at the top and bottom boundaries (Middleton, 1993; Islam & Imran, 2010).

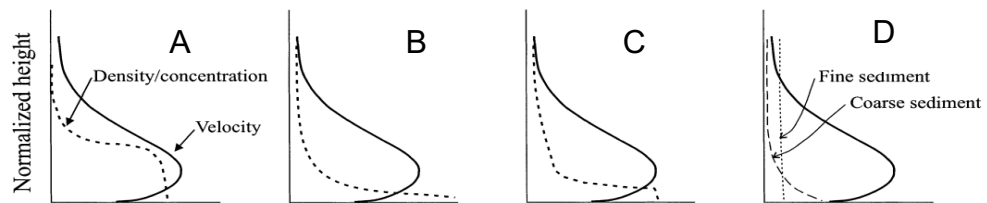


Figure 2.6 - Different density profiles (Kneller & Buckee, 2000); A) Two-layer profile, B) Smooth profile, C) Stepped profile, D) Uniform profile.

The mean internal fluid velocity within a gravity current is always higher than that of the flow front (Benjamin, 1968; Middleton, 1993). It has been shown experimentally that the maximum velocity excess between the advancing body fluid of brine gravity currents and that of the current heads may exceed 50% (Kneller et al., 1999; Sher & Woods, 2015). These velocity patterns can be related to the three distinct regions within the currents, based on theoretical considerations: i) an energy-conserving head within which fluid velocity equals to that of the current head, ii) a dissipative wake region containing the body and the tail with fluid velocity greater than the current speed by a factor of up to 1.3-1.5 (see Lowe et al., 2002). The difference between fluid velocity in the wake region and current front velocity is required to account for mass balance (see Fig. 2.7).

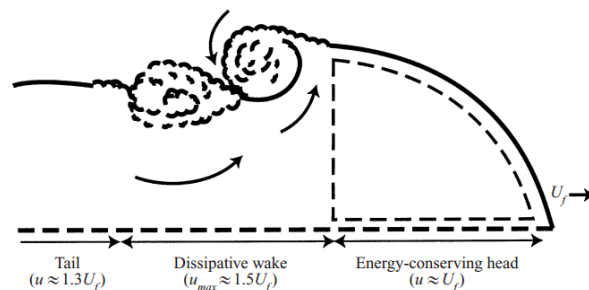


Figure 2.7 - Representation of 2D flow structure (adapted from Lowe et al., 2002).

2.4.3.2 Vertical density profile

Density profile of a gravity current is characterised by the development of a dense base above which fluid density gradually decreases upwards (Middleton, 1993; Kneller & Buckee, 2000; Monaghan, 2007). A typical density profile consists of a dense lower region and an upper one within which the density significantly decreases (profiles B, C and D in Fig. 2.6). The fluid in the upper region is mixed more homogeneously, which accounts for a more constant density profile. In particular, turbidity currents have a basal layer where coarse sediments are concentrated whilst most of fine particles are suspended in the upper layer above it.

The two-layer density profile (Fig. 2.6A) comprises a constant density lower layer and a continuously stratified upper one (e.g., Simpson & Britter, 1979; Middleton, 1993; Hosseini et al., 2006). The lower layer has the form of a high-density underflow and the upper one is diluted by the ambient. The inflection point between the two layers does not have to match the velocity maximum position. However, the model was justified as being too simple to be widely applicable (Kneller & Buckee, 2000). Three other profiles better characterise concentration profiles of gravity currents. Saline and weakly depositional sediment currents tend to exhibit profiles (B) or (C), depending on the sizes of suspended sediments, as the basal layers of such flows appear very dense, whereas the upper layer is significantly diluted due to ambient entrainment. If the variation of grain size of sediments suspended within turbidity currents is more linear, the flows likely have concentration profiles as shown in Fig. 2.6B. Very fine graded sediments tend to distribute homogeneously within flows of low density (Fig. 2.6D).

2.5 EXPERIMENTAL APPROACHES TO STUDY GRAVITY CURRENTS

2.5.1 Overview of experimental techniques

A range of techniques for measuring internal fluid velocities and concentrations within gravity currents have been developed. To measure velocity fields of

sediment flows Ultrasonic Velocimetry Profiling (UVP) is a useful technique which calculates internal velocity based on the shifts of pulses reflected by suspended sediments (Baas et al., 2005; Felix et al., 2005). An UVP probe can measure flow velocities at many (e.g., 128) points along one profile. In addition, Acoustic Doppler Velocimetry (ADV) is another velocity profiling technique that offers high frequency instantaneous measurements of streamwise and also cross-stream velocity of gravity currents (see e.g., Chapters 3, 4 and 5). An ADV probe is set up vertically, capturing internal velocity variation of flows passing by the measurement window of approximately 7.1 cm height.

In order to acquire density data, siphoning techniques can be used to collect fluid samples of experimental flows (e.g., Gray et al., 2006; Stagnaro & Pittaluga, 2014). Such techniques allow vertical density profiles of the flows to be observed by deploying arrays of siphoning tubes stacked vertically above the flume bed. If saline flows are modelled, conductivity tests are conducted on the samples in order to deduce density data (see Chapter 4). In addition, there are alternative non-intrusive techniques to siphoning such that density data are collected without disturbing the evolution of gravity flows. For example, Hosseini et al. (2006) measured particle concentration profiles in sediment flows using an acoustic-sensor methodology which is referred to as acoustic backscattering. This non-intrusive acoustic sensor is used in this method in order to detect the presence of laden sediments and, therefore, offers a technique to estimate sediment concentration without disturbing the flows. Also, Focus Beam Reflectance Measurement (FBRM) offers a tool to measure time-series chord length distribution of sediments within the flows; such chord length distribution can be converted to particle size distribution using relevant assumptions and method (see Chapter 5; Wynn, 2003).

2.5.2 Experiments and theory for non-particle-driven gravity currents

Experiments to model compositionally-driven gravity currents are conducted as an attempt to study the flow dynamics. Such gravity flows are commonly modelled using saline and data collected are used to generalise understanding of flow

dynamics (see e.g., Middleton, 1993; Gladstone et al., 2004; Darby & Peakall, 2012; Sher & Woods, 2015). Experimental data are often validated by observations from theoretical and numerical studies (e.g., Huppert & Simpson, 1980; Islam & Imran, 2010; Abad et al., 2011). In particular, researchers have paid attention to the slumping phase of gravity currents. For example, experimental data describing the evolution of saline gravity currents within the slumping phase as observed in laboratory experiments for full-depth release (i.e., experimental set-up in which initial height of dense fluid contained within a lock box equals ambient height) agree well with theoretical analysis based on box models (Huppert & Simpson, 1980). Such a theoretical model deploys an assumption that gravity currents evolve into a series of rectangles of fixed area and thus flows have constant volume. The vertical axis in Fig. 2.8 represents the ratio between measured and predicted current lengths. As can be seen from the figure, experimental measurements matched very well with theoretical estimations until the point at which fractional time reaches unity (i.e., within the slumping phase). After that, gravity currents are no longer in their initial phase and viscosity effects become dominant (Huppert & Simpson, 1980; Huppert, 1982; Rottman & Simpson, 1983; Kneller et al., 1999). Although mixing between current head and ambient is assumed to be insignificant in the slumping phase, it might become important in inertial and viscous phases (Amy et al., 2005; Di Federico et al., 2006).

The transitions between different phases during the evolution of gravity currents were studied experimentally, supported by other mathematical analysis (Rottman & Simpson, 1983). Results obtained from two-layer shallow water theory suggested that reflected waves from the end wall (i.e., waves generated upon the slumping of dense fluid in the lock box) had the form of hydraulic bores for initial fractional depths higher than 0.5 (see e.g., Rottman & Simpson, 1983; Lowe et al., 2002). However, experimental observations indicated a higher threshold of up to 0.7 due to mixing with the ambient following the slumping of the dense fluid. Experiments in which gravity currents with different initial fractional thicknesses were studied were also conducted by Britter & Simpson (1981) as an attempt to qualitatively study the dependence of intrusion head

dynamics on the interface thickness of an ambient comprised by two layers of fluids of different densities. Lock-release experiments were also conducted by Lowe et al. (2002) in order to validate their numerical solutions of the dynamics of turbulent waves generated on the body of gravity currents.

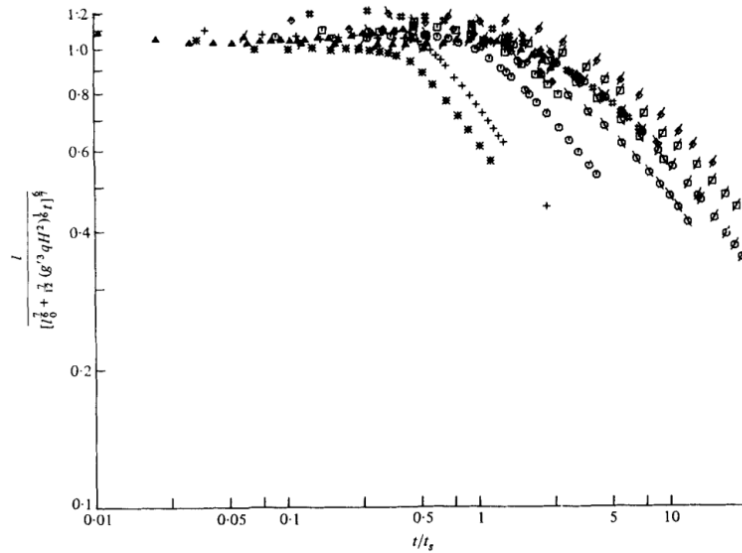


Figure 2.8 - The ratios of measured and predicted current lengths as a function of time (adapted from Huppert & Simpson, 1980).

In most of the research which has been mentioned in this chapter, lock-release experiments were performed where lock-gates were positioned proximally to one end of a flume. This experimental set-up offers a benefit of capturing the evolution of gravity flows over a long distance from source. However, as discussed above, a counterflow of ambient fluid is produced as a result of lifting up the lock gate and eventually such waves or hydraulic bores overtake the gravity currents. Such surface waves can have significant impacts on sedimentation and dynamics of gravity currents.

2.5.3 Experiments for particle-driven gravity currents

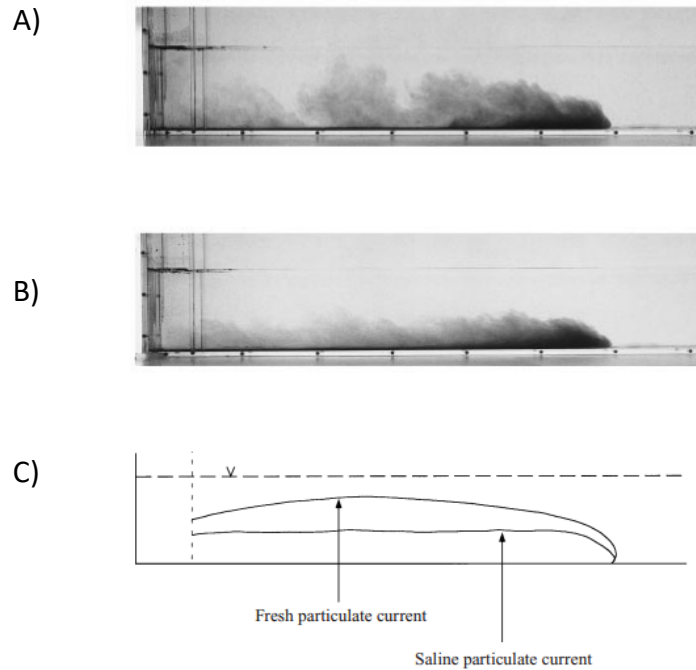


Figure 2.9 - Two gravity currents with different interstitial fluids (adapted from Gladstone & Woods, 2000); A) Interstitial and ambient are water, B) Interstitial fluid is saline and C) Conceptual models of the two cases.

Particle-laden gravity currents have been experimentally investigated by various authors. For example, Bonnecaze et al. (1993) experimentally produced five gravity currents of the same reduced gravity but different composition (one purely saline current and four mono-disperse particle-driven currents made of particles with various sizes) in order to compare their dynamics. The evolution of current lengths over time was studied with the conclusion that, at early stages, all currents advanced at the same velocity since sedimentation in the particulate-bearing flows had not become significant. Thereafter, the saline current travelled more quickly than others and eventually reached the longest run-out length, whereas velocities of the other four currents increased very slowly. Run-out length was inversely proportional to particle size. The explanation was that particles with bigger sizes were deposited more quickly than those with smaller sizes and,

consequently, this sedimentation reduced density excess and buoyancy. Bonnecaze et al. (1993) also reviewed the assumption of initially inviscid flow, such that at some point after the constant speed phase, the current will decelerate and viscous forces dominate inertial forces. A critical value of Reynold number was proposed as 2.25, marking the transition from inertial-buoyancy balance to viscous-buoyancy balance.

The dependence of sediment flow evolution on particle size and concentration has also been investigated (e.g., Hallworth & Huppert, 1998; Gladstone & Woods, 2000). It was reconfirmed that currents driven by fine mono-disperse particles travelled faster and further than those made of coarse mono-disperse particles. Moreover, as observed from bi-disperse gravity current experiments, currents with higher ratios of fine to coarse particles travelled faster than those with lower values. In addition, the effect of adding fine grained particles into currents driven by coarser sediments and vice versa was studied (e.g., Gladstone et al., 1998). Adding coarse particles into a current composed of fine particles has insignificant impacts on the current dynamics (see Fig. 2.9). However, adding even a very little portion of fine particles into coarse-rich sediment gravity currents can enhance run-out length and enable the transportation of coarse particles further downstream. This is because fine particles remain in suspension for longer periods and thus the duration of flows can be increased. This observation holds true for both poly- and bi-disperse gravity currents (Gladstone et al., 1998). Gladstone & Woods (2000) highlighted some implications for sediment deposition. In particular, turbidity currents of fine particles can travel further than clear-sand turbidity currents of the same initial scale (i.e., coarser sediments). Also, although sediment densities are reduced as flows deposit materials further downstream, the distributions of fine and coarse sediments along channel pathways are different (e.g., Gladstone et al., 1998; McLeod et al., 1999). Such distributions depend on the range of materials suspended within the flows. Specifically, experimental data suggested that the majority of coarse sediments tend to be deposited within the first 25% of run-out distances though flows with higher initial fractions of fine sediments can deposit

coarse materials at more distal localities, whereas fine sediments are likely distributed more homogeneously along the pathways (e.g., Gladstone et al., 1998). Such observations are important in the interpretation of the spatial variation in sedimentary patterns as the initial distribution and range of grain size of initial sediments might affect the grading profiles of multi-pulsed turbidites. This means multi-pulsed turbidites might only be deposited proximally, given relevant range of sediment grain size. For example, if the range of sediments sourced from upstream initiation points does not vary significantly, initiation signals of multi-pulsed turbidity currents might not be reflected in the associated deposits.

In summary, based upon theoretical backgrounds in experimental research of turbidity currents, experiments to model both saline and sediment-bearing gravity currents were conducted and are reported in Chapters 3, 4 and 5 in order to achieve the goal of this research. A range of experimental techniques deployed in studying gravity currents at laboratory scale, as reviewed, will be reflected in these chapters. In addition, interpretation of experimental data, presented in each chapter, will seek to further the current understanding of multi-pulsed turbidity currents. In chapter 6, a discussion on the application and significance of this research will be provided.

Chapter 3

Pulse propagation in turbidity currents

Submarine turbidity currents are a key mechanism in the transportation of clastic sediments to deep seas. Such currents may initiate with a complex longitudinal flow structure comprising flow pulses (e.g., by being sourced from retrogressive sea floor slope failures) or acquire such structure during runout (e.g., following flow combination downstream of confluences). A key question is how far along channel pathway complex flow structure is preserved within turbidity currents as they run out and thus if flow initiation mechanism and proximity to source may be inferred from the vertical structure of their deposits. To address this question, physical modelling of saline flows has been conducted to investigate the dynamics of single-pulsed vs. multi-pulsed density driven currents. The data suggest that under most circumstances individual pulses within a multi-pulsed flow must merge. Therefore, initiation signatures will only be preserved in deposits upstream of the merging point, and may be distorted approaching it; downstream of the merging point, all initiation signals will be lost. This new understanding of merging phenomenon within multi-pulsed gravity currents broadens our ability to interpret multi-pulsed turbidites.

3.1 INTRODUCTION

Gravity currents are driven by a density difference between two fluids, and are widespread in both industrial scenarios and natural settings. Turbidity currents are a form of dilute particulate gravity flow in which the flows move under the gravitational action upon dispersed sediments suspended within the interstitial fluid (Middleton, 1993; Huppert, 1998; Kneller & Buckee, 2000; Sequeiros, 2012). Turbidity currents in natural settings can range up to hundreds of metres in thickness (Piper et al., 1988; Sumner & Paull, 2014) with durations that may extend up to hours or days (Piper et al., 1999; Xu et al., 2004; Mikada et al., 2006); they are a principal mechanism by which sediment is transported from continents to deep seas (e.g., Simpson, 1982; Talling et al., 2015). Turbidity currents can be

initiated by submarine slope failures (triggered by earthquakes or other mechanisms) or by direct hyperpycnal underflow into the oceans; they commonly flow through submarine channels into the deep oceans (Mulder & Alexander, 2001; Best et al., 2005; Piper & Normark, 2009).

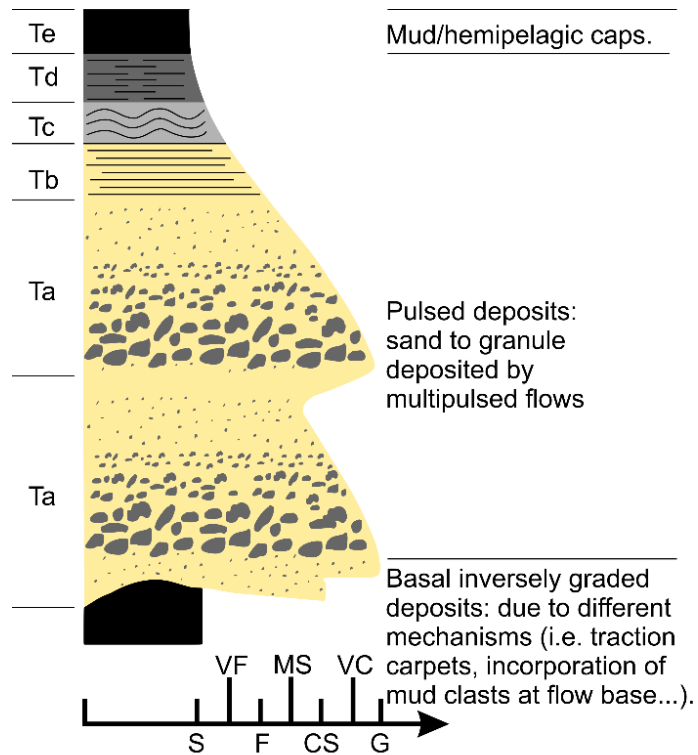


Figure 3.1 - Schematic sedimentary log of a turbidite with intervals of inversely graded grain size. Inverse grading in pulsed deposits is distinct from basal inverse grading, which can be produced by other mechanisms (e.g., Hand, 1997). Note: S = Silt; VF = very fine sand; F = fine sand; MS = medium sand; CS = coarse sand; VC = very coarse sand; G = granules. Mudstone clasts and hemipelagites are not always present. Relative thicknesses of individual intervals of the deposit depend on compositions of sediments and the timescales within which the intervals are deposited.

Sediments deposited by turbidity currents – turbidites – commonly exhibit continuously upward fining of mean grain size (Fig. 3.1). This is referred to as “normal grading” (Bouma, 1962; Lowe, 1982; Gutiérrez-Pastor et al., 2013). However, it is not uncommon for turbidites to show more complex grading profiles, such as inverse grading (e.g., Kneller & McCaffrey, 2003; Mulder et al.,

2003). On the basis that the grain size at any particular level in a deposit relates to the instantaneous basal shear stresses, normal grading suggests deposition from a waning flow, whereas, inversely graded (upward coarsening) deposits suggest deposition from waxing flow (Kneller & Branney, 1995; Kneller & McCaffrey, 2003; Mulder et al., 2003; Amy et al., 2005; Basilici et al., 2012, cf. Hand, 1997). A more complex exception from normal grading patterns is seen when repeated intervals of coarsening are seen superimposed upon an overall normally-grading profile. Beds exhibiting this pattern are here described as “pulsed” or “multi-pulsed” turbidites, as the implication is that pulses of increased velocity occurred in the overpassing flow at the point of deposition. Pulsed turbidites can be differentiated from “stacked” turbidites which, although superficially similar, represent the closely vertically juxtaposed deposits of two or more individual turbidity currents; in practice, distinguishing the two can be challenging where later flows erode into the deposits of earlier flows to produce deposit amalgamation and intervening fine grained material is absent. Where submarine turbidites show deviations from a continuous normal grading, a variety of mechanisms can be invoked to explain pulsed flow generation, for example discrete episodes of retrogressive slumping (Piper et al., 1999; Canals et al., 2004; Bull et al., 2009), variations in ground shaking in currents initiated by single seismic events (Goldfinger et al., 2012), variations in the flood hydrograph for hyperpycnally generated flows (Mulder & Alexander, 2001) and flow combination along the pathway of channel confluences (Nakajima & Kanai, 2000; Ismail, et al., 2016). In addition, flow reflection in confined settings has also been invoked to cause pulsing (e.g., Haughton, 1994). Research on how these mechanisms might be distinguished in the depositional record of pulsing flows is less extensive (see examples in Goldfinger et al., 2012). A key consideration in this regard is how long non-monotonic variations in mean flow velocity along the flow may persist from source, and thus potentially be indicative of the flow generation mechanism. A related consideration is whether the degree to which a deposit approaches a normal grading profile may be an indirect indicator of distance from source.

Here, saline flow experiments are reported with the aim of informing understanding of the dynamics and evolution of pulsed turbidity currents, and exploring the possible implications for the interpretation of vertical depositional grading profiles. A principal goal of this chapter is to review and extend the inferences regarding flow behaviour and proximity to source that can reasonably be made in natural turbidites. This contribution: i) presents novel experimental data that detail the variation of multi-pulsed flow dynamics; ii) assesses how flow dynamics may be interpreted from turbidite grading structure; and iii) reviews two case studies in which the interpretational template of turbidites with complex grading profiles is reviewed and broadened.

3.2 METHODOLOGY

3.2.1 Experimental set-up and research methodology

The methodology of generating gravity currents in lock exchange flumes has been widely applied by various authors (e.g., Middleton, 1966; Holyer & Huppert, 1980; Britter & Simpson, 1981; Lowe et al., 2002; Gladstone et al., 2004). In the work described here, lock exchange experiments of saline flows were conducted in order to gain an understanding of the internal dynamical structure of turbidity currents. Although they do not take into account the effects of particle transport, as occurs in natural turbidity currents, saline flows are a well-established proxy for studying such flows (e.g., Kneller and Buckee, 2000; Islam and Imran, 2010; Hogg et al., 2016). Similarly, turbulent laboratory-scale flows are thought to deliver a good representation of the dynamics of flow at natural scale (e.g., Paola et al., 2009). Figure 3.2 shows the experimental set-up, in which a 5 m long Perspex flume with two lock-exchange gates was used, incorporating overspill boxes at both ends to reduce the effect of waves caused by the removal of the lock gates. Two 12.5 cm-long lock boxes were set up in series at one end to enable the generation of multi-pulsed flows, using saline fluid with 5% density excess (1050 kgm^{-3}) as a proxy for turbidity currents. Using a pneumatic lock-gate driver, the upstroke speed of each lock gate was set at 1.0 ms^{-1} so that any resulting turbulence was minimized, without being so slow that a partially-withdrawn lock

gate affected the counter flow of fluid into the lock. The release time delay of the second gate could be adjusted to within 1/10 s of the first release; here it was set to 4 s so that the interaction between pulses in a bi-pulsed flow occurred within the length of the flume. To model single-pulsed flows, the delay was set to zero. The dense saline fluid was prepared in a 180 l mixer, and monitored to ensure consistent density. It was pumped slowly into the lock boxes via an intake valve on the bottom of each lock box, displacing fresh water above whilst preserving a sharp upper boundary. Each lock box was filled to a depth of 0.05 m with dense fluid dyed yellow in the first box and blue in the second to enhance flow visualization and front position tracking. The total lock box depth equalled the 0.25 m depth of the external ambient. The 1:5 depth ratio maintains fully turbulent, subcritical flow (Reynolds numbers were c. 2,000 and Froude numbers less than 1) while allowing suitable depth scaling approximating to real-world submarine flow, where flow to ambient depth ratios are 1:8 or greater (Piper et al., 1988; Xu et al., 2004).

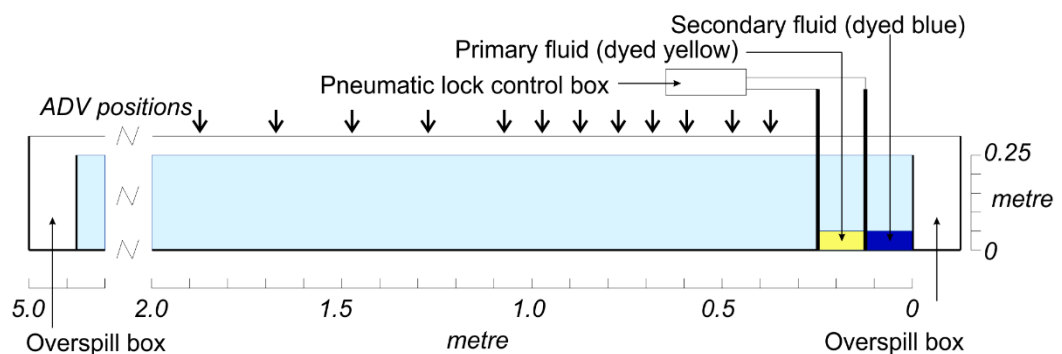


Figure 3.2 - Schematic of the experimental set up. A 5 m-long flume with two lock boxes (each 0.125 m long) set up in series at one end to enable the delayed release of a second pulse to generate a pulsed flow. Two overspill boxes were used to reduce the effect of returning waves associated with slumping of dense fluids in the lock boxes. Acoustic-Doppler Velocimetry (ADV) was used to collect velocity data at successive downstream positions located at 0.365, 0.465, 0.585, 0.675, 0.765, 0.865, 0.965, 1.065, 1.265, 1.465, 1.665 and 1.865 m.

Five HD interlinked cameras were deployed to capture a wide range of view of the flume. The cameras were carefully aligned so as to prevent image distortions and stitching artefacts. VirtualDub and Avisynth were used to stitch five linked video tracks together, based on an audio time cue; camera synchronization was within 1 frame (0.042 s; 24 fps). The alignment of the five cameras was checked using gridlines on the bottom of the flume (Fig. 3.3). The method of profiling Acoustic Doppler Velocimetry (ADV) was used to measure spatio-temporal variation of horizontal streamwise velocities (Craig et al., 2011; MacVicar et al., 2014; Brand et al., 2016). This methodology offers velocity profile measurements at high frequencies and with high resolution. The ADV probe head was positioned 7.1 cm above the bed of the flume at 13 different locations along the flume (Fig. 3.2), capturing a measurement of 30 mm flow depth at each position. Both the dense fluid and the ambient were seeded with neutrally-buoyant particles of 10 μm diameter to generate a consistent acoustic reflection. Spatio-temporal depth-averaged velocity profiles were constructed for both single and multi-pulsed flows using the following equation:

$$(3.1) \quad \bar{u} = \frac{\int_0^h v \, dz}{h}$$

where v is the instantaneous velocity of the flow and $h = 0.03 \text{ m}$.

3.2.2 Dynamics of density currents

The dynamics of lock-gate release density currents can usefully be associated with the slumping, inertial and viscous flow regimes of flow evolution, varying in each due to the changing relative significance of buoyancy, inertial and viscous forces (Huppert & Simpson, 1980; Huppert, 1982; Rottman & Simpson, 1983; Bonnecaze et al., 1993; Kneller et al., 1999; Amy et al., 2005; Di Federico et al., 2006; Huppert, 2006; Sher & Woods, 2015). The slumping phase can extend up to 10 lock lengths from the initiation point; during this phase the gravity current is driven mainly by buoyancy forces resulting from the density difference between the dense fluid and the ambient. The buoyancy force of the flow is balanced by frictional forces at both upper and lower boundaries of the flows. This balance is principally caused

by the return flow of ambient fluid balancing the slumping of dense fluid out of the lock box; the flow travels with nearly constant velocity in the slumping phase. During the inertial phase, inertial effects become important; this regime is characterized by flow deceleration. Once the flow becomes sufficiently shallow, frictional forces exceed buoyancy and inertial forces, and the flow enters the viscous phase, in which it continues to decelerate.

3.3 RESULTS

Below, the results from the single- then multi-pulsed flows are described in sequence, considering firstly the flow visualization data and then the flow velocity data.

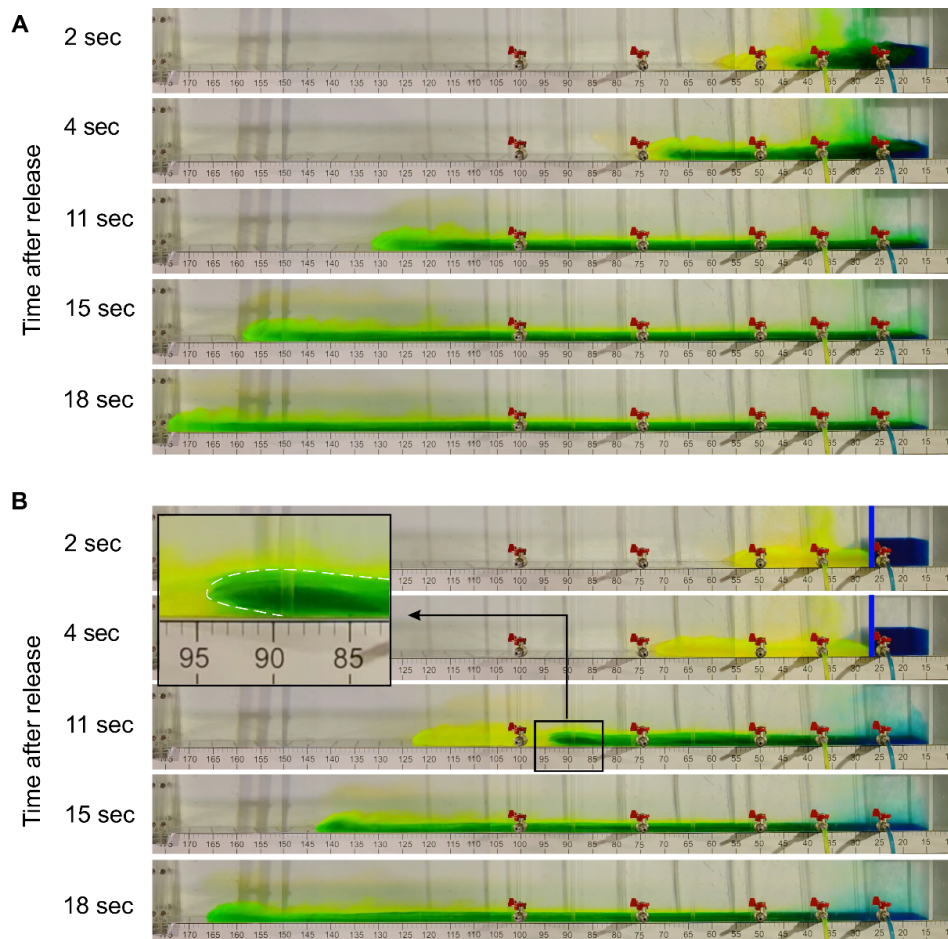


Figure 3.3 - Photographs of the flow at different time intervals for A) a single-pulsed flow experiment with 0 second delay time and B) a multi-pulsed flow experiment with 4 second delay time between two pulses. In (B) the

two pulses completed merged between 15 s and 18 s. Gridlines on the bottom of the flume were used for camera alignment and flow position tracking. Inset shows the advection of the second pulse within the first pulse.

3.3.1 Single-pulsed flow

To distinguish the frontal and rearward components of the single-pulsed flow, the denser than ambient fluid in the front lock box was dyed yellow, and that in the rear blue, as shown in Fig. 3.3A. As noted above, a zero second delay time between two lock gates enabled the instantaneous trigger of the gates and the generation of a single release of the dense fluid. Following the release, the dense fluid in the lock boxes collapsed, forming a negatively buoyant density driven flow that propagated along the bottom of the flume. As the current advanced along the flume, the blue portion of dense fluid comprising the rear 50% of the flow at initiation was advected towards the front of the current (Fig. 3.3A, $t=2-4$ s; cf. Sher & Woods, 2015). The advection formed a visible intrusion around half of the flow depth, similar to advection in Poiseuille flow (Lowe et al., 2002; Sher & Woods, 2015). The dyed components of the flow are inferred to have progressively mixed, changing the flow colour from yellow/blue to green. In addition, the variation in the degree of mixing between the dense fluid and the ambient is qualitatively indicated by the change in relative colour intensity of the green fluid (Fig. 3.3A, $t=2-18$ s). This change is especially pronounced at the flow head, where turbulent mixing processes are largest, due to shear-driven generation of Kelvin-Helmholtz billows (Britter & Simpson, 1978; Johnson & Hogg, 2013).

The tracking of flow front positions using video data and the collection of velocity time series using fixed instrumentation at different downstream locations permit velocity profiles of both single- and multi-pulsed flows to be detailed (Figs. 3.4-3.6). By tracking the positions of the front (yellow) and rear (blue) components of the single-pulsed flow, two dynamical flow regimes can be identified. In the initial slumping phase, the flow advanced at a nearly constant velocity of c. 0.082 ms^{-1} for 1.25 m (c. 5 lock lengths). During the succeeding inertial phase, the flow

decelerated from 0.082 ms^{-1} to 0.008 ms^{-1} over 2 m. The viscous phase of the flow was not observed in the length of the flume covered by the cameras. The rearward portion of the single-pulsed flow was advected forwards within the flow at a nearly constant velocity of 0.1 ms^{-1} , i.e., 25% faster than the flow head, reaching the flow front during the slumping phase some 0.8 m from source (Fig. 3.4A). The single-pulsed flow (Fig. 3.5A) displayed the rapidly waxing and progressively waning velocity structure which is usually observed in lock-gate release experiments (e.g., Simpson, 1982; Kneller et al., 1999). The velocity maximum was located at c. 25% of the local flow depth, as commonly seen in laboratory experiments, field data and theoretical models (e.g., Kneller & Buckee, 2000; Talling et al., 2015). The magnitude of flow velocity was observed to decrease with increasing time and distance from source, as indicated by the change in colour intensity in Fig. 3.5A. The depth of the flow may be estimated by using the vertical velocity profile to establish the height of the zero velocity contour that separates downstream from upstream (return) flow (Dorrell et al., 2016); e.g., in Fig. 3.5A at 0.365 m downstream position and 2.5 s, $h=0.015 \text{ m}$. The spatio-temporal variation of depth-averaged velocity for single-pulsed flow is shown in Fig. 3.6A in which the boundary of the black region indicates the arrival of the flow in time and space. The plot shows a model of standard flow evolution in which the head velocity, indicated by the yellow to orange regions behind the black edge, is constantly high within slumping phase (up to the distance of about 1.4 m in Fig. 3.6A) and then decreases with increasing time and distance.

3.3.2. Multi-pulsed flow

Initially, a single flow pulse dyed yellow was released from the front lock box and propagated along the flume in the form of a negatively-buoyant density current (Fig. 3.3B, $t=2 \text{ s}$). The second pulse was triggered 4 s after the first one, at which time the fluid comprising the initial release had collapsed to approximately one fourth of its initial depth in the front lock box (Fig. 3.3B, $t=4 \text{ s}$). The second pulse was quickly advected towards the front of the flow, in the form of a visible intrusion with sharp boundaries, at approximately half of the height of the first pulse (Fig. 3.3B, inset $t=11 \text{ s}$). The colour change from yellow and blue to green

reflects the progressive mixing between the two pulses (Fig. 3.3B, $t=11-18$ s). Eventually, the two pulses merged at a distance 1.4 m from source and the whole flow evolved in a manner similar to that of a single-pulsed flow during its inertial phase (Figs. 3.3 and 3.4). Kelvin-Helmholtz billows were generated on the back of the flow head, enhancing turbulent mixing in the flow and between the dense and ambient fluid (Britter & Simpson, 1978; Johnson & Hogg, 2013). Thus the colour shift at the flow head, as indicated by the variation in colour intensity of the green (mixed) fluid, was intensified (Fig. 3.3B, $t=2-18$ s).

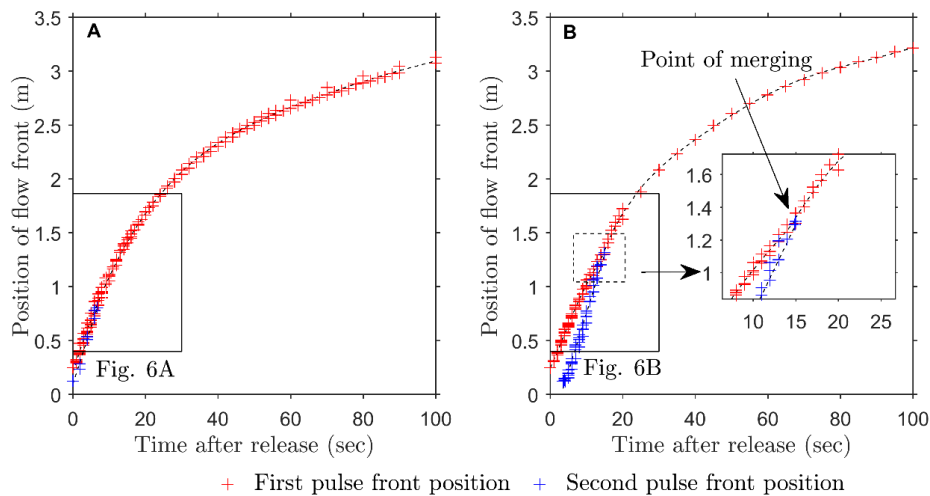


Figure 3.4 - Plots showing the location of the front of A) a single-pulsed and B) a multi-pulsed flow over time. Dashed curves are best fits of front position data collected from multiple experiments.

Front position tracking and the collection of velocity time series enabled velocity profiles of the multi-pulsed flows to be detailed (Figs. 3.5 and 3.6). The first pulse entered its slumping phase at initiation, and had travelled at a nearly constant velocity of 0.079 ms^{-1} for 0.65 m, (approximately five 12.5 cm lock lengths) before the second pulse was released. The second pulse was released 4 s after the first (Figs. 3.4B and 3.5B) and progressively intruded into it. The combined flow accelerated at the point when the intrusion reached the flow head (Fig. 3.4B, inset) advancing at a nearly constant velocity of c. 0.074 ms^{-1} for 0.25 m from the point of merging. Thus, the slumping phase of the multi-pulsed flow lasted over

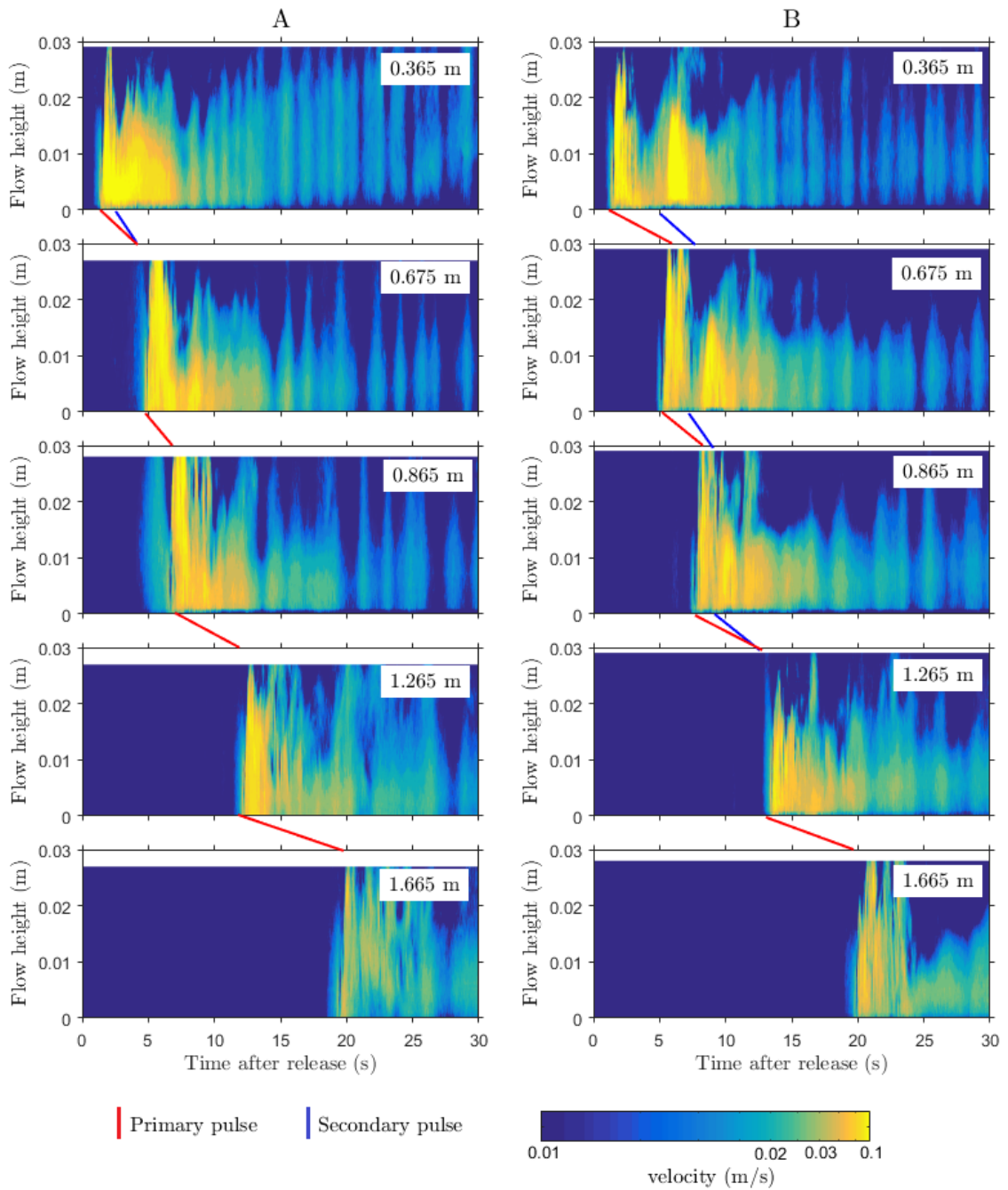


Figure 3.5 - Contour plots showing spatio-temporal variation of internal velocity structure within (A) a single-pulsed flow and (B) a multi-pulsed flow at 0.365 m, 0.675 m, 0.865 m, 1.265 m and 1.665 m downstream from the back of the lock box. Red and blue lines between plots indicate the arrivals of the primary and secondary pulses, respectively; these become progressively closer with time in multi-pulsed flows. Note that the low velocity variations that appear as vertical stripes of amplitude ($< 0.025 \text{ ms}^{-1}$) show the effect of surface waves, white horizontal stripes in each subplot are areas of no data.

1.40 m (approximately six 25.0 cm lock lengths). The slumping phase ended at 1.65 m from the source. The velocity of the second pulse averaged nearly 0.110 ms^{-1} , which is approximately 35% greater than the initial head velocity of the first pulse. The inertial phase of the merged multi-pulsed flow was characterized by a reduction in velocity to 0.012 ms^{-1} over a distance of about 1.85 m between 1.65 m to 3.5 m from source (Fig. 3.4B). As with the single-pulsed flow experiments, the viscous phase of the multi-pulsed flow was not captured within the camera range of these experiments. The multi-pulsed flow displayed a more complex velocity structure than the generic waxing-waning velocity profile observed in the lock-release single-pulsed gravity currents (Fig. 3.5B). Two separate pulses of relatively high velocity ($>0.1 \text{ ms}^{-1}$) were distinctly observed proximally to source (Fig. 3.5B, 0.365 m). The time separation between two pulses decreased as the second pulse was progressively advected towards the front of the first pulse (e.g., Fig. 3.5B, 0.365 m, 0.675 m and 0.865 m). At the point of merging, the two pulses tended to have similar velocities. Beyond the point of merging, the merged flow exhibited essentially the same waxing-waning velocity structure as observed in the single-pulsed flow experiments (Fig. 3.5A-B, 1.265 m, 1.665 m). The velocity maximum was also located at about 20% of the flow depth, as observed in the single-pulsed flow experiments. In order to visualize the spatio-temporal variation in the velocity profile of the multi-pulsed flow, a contour plot showing the depth-averaged velocity of the flow was constructed (Fig. 3.6B). The depth-averaged velocity of the first pulse was relatively high proximal to source (0.1 ms^{-1}). The high intensity region surrounding the dotted line on Fig. 3.6B indicates the signal of the advection of the second pulse within the first pulse. The initial relative timing of this signal was distorted by being progressively reduced towards the point of merging. Beyond this point, the signal of the second pulse intrusion in the velocity profile was completely lost (i.e., "shredded", *sensu* Jerolmack & Paola, 2010; Figs. 3.5B and 3.6B).

3.3.3. Single-pulsed vs. multi-pulsed flows

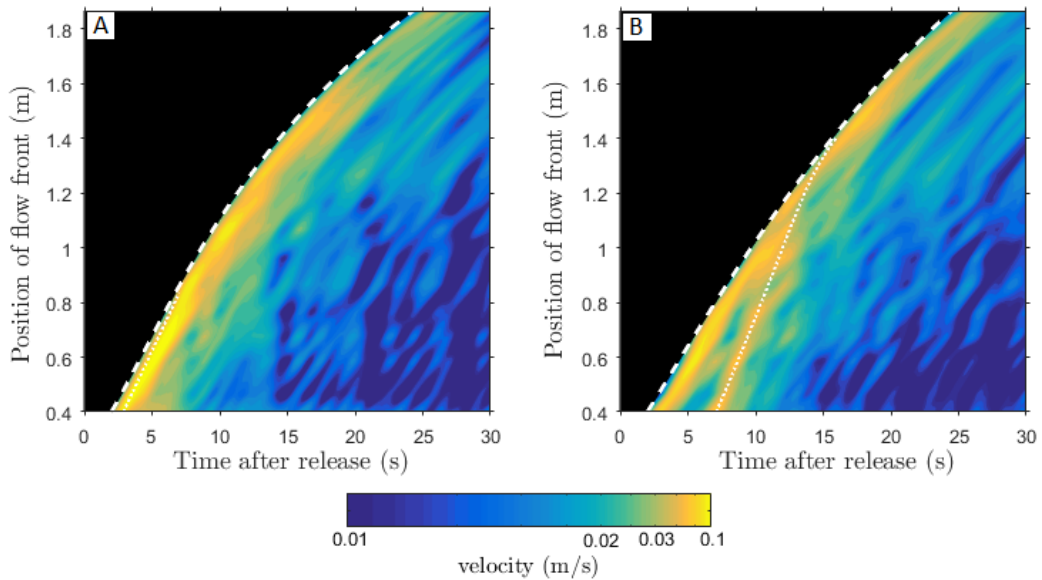


Figure 3.6 - Contour plots showing spatio-temporal variations of depth-averaged velocity of A) Single-pulsed flows and B) Multi-pulsed flows. Note: Dashed and dotted curves are best fits of front positions of primary and secondary pulses respectively.

Multi-pulsed flow evolution is characterized by interaction of the separate pulses which eventually merge at some distance from the source; such flows exhibit a pulsing character up to the point of merging. This pulsing characteristic is not seen in single-pulsed density currents. Figure 3.7A shows raw (unfiltered) data detailing the temporal variation of depth-averaged velocities of the single- vs. multi-pulsed flows, shown proximally to source, at the point of merging and distally from source. The surface waves set up at flow initiation were not completely removed by the overspill boxes, and resulted in a fluctuation in the raw data; the magnitudes of the fluctuations are relatively small compared to the front velocity of the flows, and are not thought to have significantly influenced the flow dynamics. To more clearly assess the flow dynamics, the raw velocity data are filtered and replotted in Fig. 3.7B. Before the point of merging, the depth-averaged velocity profile of single-pulsed flows exhibited a standard waxing-waning velocity structure whereas the profile of multi-pulsed flows has two pronounced pulses (0-7 s at 0.365 m Fig. 3.7B). The time delay measured between

the two velocity pulses depends on initial lag time at initiation, and also upon the point of measurement. Up to the point of merging, the time separation between the two pulses in multi-pulsed flows progressively decreased. For the multi-pulsed flow, after the peak of the second pulse passed the position of profiling, the velocity magnitude of the flow became comparable to that of a single-pulsed flow comprising the same initial dense fluid. In distal regions, both single- and multi-pulsed flows showed similar velocity structures to the normal waxing-waning velocity profile (Fig. 3.7B).

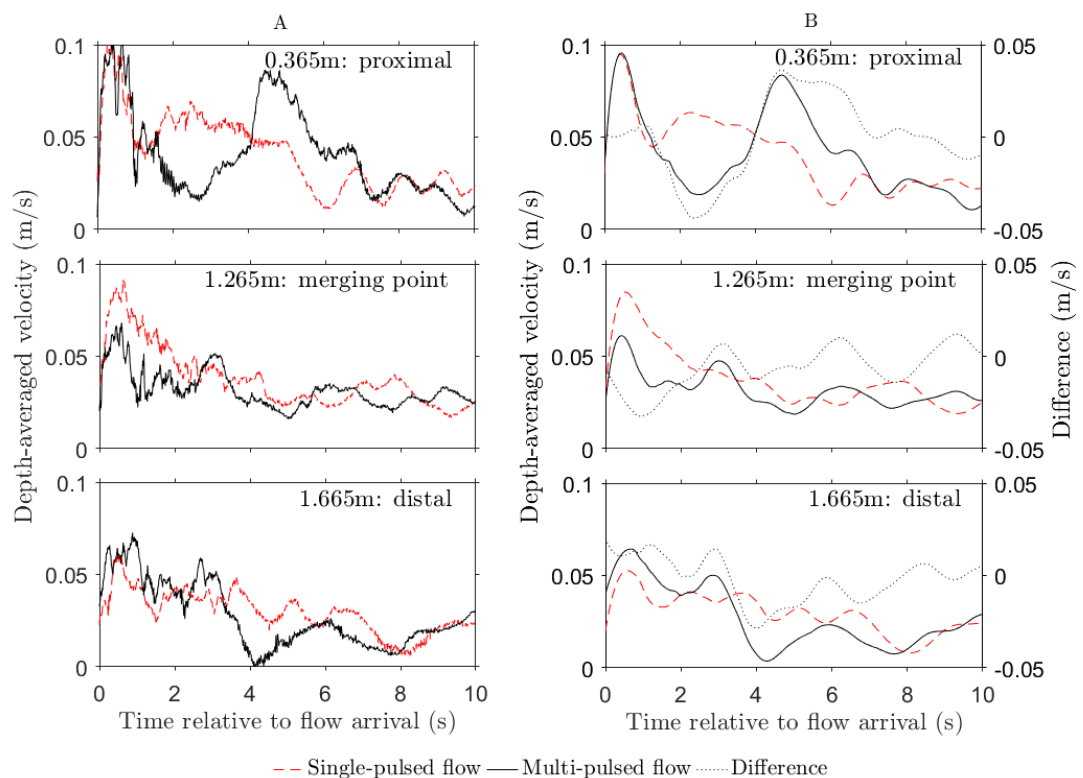


Figure 3.7 - Comparison between depth-averaged velocity profiles of single- and multi-pulsed flows at three different downstream positions: A) Raw data and B) Filtered data. Note: Raw data were filtered by using Savitzky-Golay smoothing process in MatLab with a polynomial order of three and a framelength of 151.

3.4 DISCUSSION

3.4.1 Multi-pulsed turbidity current propagation

Turbidity currents commonly develop vertical density stratification during runout, due to the entrainment of ambient fluid (Britter & Simpson, 1978; Hallworth et al., 1996), particle settlement (Baas et al., 2005) and also due to recirculation of fluid from the body into the head, where it is mixed and ejected backwards (Lowe et al., 2002; Sher & Woods, 2015; Hughes, 2016). It is inferred that both the single-pulsed density currents and the first pulse of multi-pulsed flows developed vertical density stratification; the change within the first pulse from an initial vertically homogeneous density profile to a stratified one can be seen from the development of a green to yellow vertical transition in the single-pulsed flow (Fig. 3.3A) and in the upward-lightening yellow colour intensity in the multi-pulsed flow (Fig. 3.3B). Consequently, the second pulse intruded into the first at a neutrally buoyant level and was advected within it.

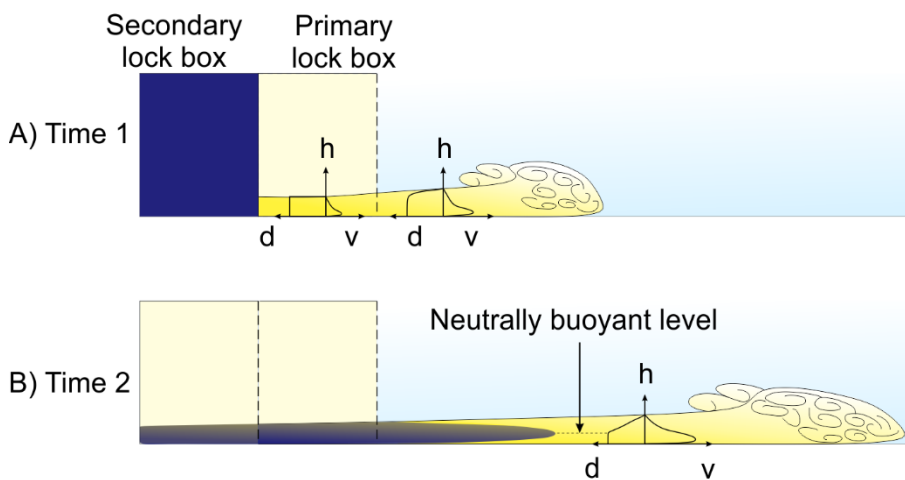


Figure 3.8 - Model of multi-pulsed flow propagation based on experimental results. Vertical axis shows flow height (h), horizontal axes show density (d) and velocity (v). Note: The model illustrates the scenario in which the second pulse intrudes into the first pulse at neutrally buoyant level (see text for discussion of alternative scenarios).

In gravity currents the velocity maximum is usually at approximately one quarter of the flow depth, with the maximum velocity being greater than the speed of the flow front (Figs. 3.3 and 3.5, Kneller et al., 1999; Lowe et al., 2002; Sher & Woods, 2015). Consequently, material from the back of the flow is advected towards the head (e.g., Sher & Woods, 2015); Gladstone et al., (2004) noted in this regard that density stratification in the pre-release fluid leads to preferential advection of lighter fluid towards the flow front. However, previous studies have focused on the case in which flow properties vary monotonically behind the head, and not considered the case in which the longitudinal velocity structure is heterogeneous, i.e., when multiple pulses are initiated separately in time but eventually merge distally from source, resulting in cyclic waxing-waning velocity structure in the flow dynamics.

Here, advection is visualised by separating both single- and multi-pulsed flows into primary and secondary components, corresponding to the front and back of the flow at initiation (Fig. 3.3). In the single-pulsed flow, the second component essentially moved with the fluid immediately in front, and quicker than the current head velocity. In the multi-pulse flows, the internal fluid velocity of the second pulse exceeded both that of the fluid pulse immediately preceding it and of the current head velocity (Fig. 3.6 and section 3.3.2), resulting in the forward advection of the second pulse being accelerated compared to that of the second flow component in the single-pulsed flows. The tracked advection rates of the second pulse in multi-pulsed flows were 10% larger than the internal flow front visualized in the single-pulsed flows, i.e., c 0.11 ms^{-1} vs. 0.10 ms^{-1} (Fig. 3.4). The increase in internal advection may in part be attributed to the additional momentum generated by the second lock-gate release. Effectively, in the multi-pulse system the second flow component is restrained by the second lock gate, against gravity, for longer than in the single-pulse experiments. Thus, the delay between the two releases creates a greater pressure difference in the multi-pulse system than that in the single-pulse system, due to the difference in the height of dense fluid in the two lock boxes. By the time of the second lock gate release, the

enhanced pressure gradient results in the formation of an internal wave and thus an increase in internal advection rates in the multi-pulse system.

Furthermore, in the multi-pulse system, the second pulse is released into the stratified remnant of the primary pulse. Stratification of the primary pulse is driven by entrainment of ambient fluid into the primary pulse after it has been released. The secondary pulse therefore forms and propagates on a neutrally buoyant level, in a similar fashion to intrusions in stratified quiescent fluids (Britter & Simpson, 1981; de Rooij et al., 1999; Bolster et al., 2008) but here modulated by the background velocity field of the primary pulse. As mixing induced stratification gradually decreases density of the primary pulse towards the density of the ambient, and as the secondary pulse is denser than the ambient, the secondary pulse will be confined within the primary pulse. Density difference between the two pulses is thus smaller than that between the first pulse and the ambient. This reduced density difference, and the delay time, between two pulses control the time required for the second pulse to reach the front of the flow. If the secondary pulse is denser than the primary pulse the intrusion will occur along the lower boundary of the flow. A consequence is that the second pulse will experience reduced drag as its interaction with the solid lower and upper flow-ambient fluid boundary is limited, i.e. lower and upper interface shear-stress (Härtel et al., 2000) is reduced in comparison to single, or the primary component of multi-pulse flows (Fig. 3.8).

Given that internal fluid velocity in the body of a gravity current is always greater than the head velocity (Kneller et al., 1999; Lowe et al., 2002; Sher & Woods, 2015), once a following pulse has begun to interact with the velocity field of the first pulse, the second pulse must eventually be advected towards the flow front. Therefore, it is concluded that the intrusion of the second pulse and the merging of two pulses seen in the experiments is an inevitable consequence of the interaction between pulses within dilute multi-pulsed density flows.

3.4.2 Conceptual models of deposition from multi-pulsed flows

Since the flow dynamics of multi-pulsed flows vary along the flow pathway differently to those of single-pulsed flows, the spatial evolution of their deposits is expected to be distinguishable. Given that upward-fining and upward-coarsening grading patterns suggest deposition from waning and waxing turbidity currents, respectively (Kneller & Branney, 1995; Hand, 1997; Mulder et al., 2003; Amy et al., 2005; Basilici et al., 2012), the waxing-waning phenomenon within multi-pulsed flows should lead to the deposition of inverse graded intervals corresponding the passage of a pulse (assuming the flow remains depositional and that an appropriate range of grain sizes is available for transport). In addition, the grading patterns of multi-pulse turbidites likely vary from proximal to distal regions, due to the progressive advection of pulses towards the flow front with increasing run-out distance. This advection should result in a progressive reduction in the time between pulses, decreasing to zero at the point of merging with the flow head; where multiple pulses are present, some may amalgamate before this point. Hence, in any associated turbidite deposit, an original pulsing signal might be relatively accurately preserved proximally, such that the relative spacing between inverse to normal grading cycles is representative of the timing differences between pulses at initiation. The signal might then be progressively distorted up to the point of merging, expressed in reductions in the relative vertical spacing of inverse to normal grading cycles and also in a reduction in the number of such cycles present. The signal will eventually be lost once all pulse components of the flow have completely merged. It should be noted that the relative spacing between cycles will also be dependent on the sedimentation rate. This is because the thicknesses of individual cycles are controlled by settling velocities of sediments (i.e., are determined by grain sizes and densities of sediments within each depositional episode).

Figure 3.9 shows the likely links between a range of turbidity current types, as defined by their longitudinal velocity structures, and their associated turbidite deposits. The deposits are based upon usage in, e.g., Bouma (1962), Lowe (1982) and Gutiérrez-Pastor et al., (2013) and references therein. Thus single turbidites

with normal grading are deposited by single-pulsed turbidity currents (Fig. 3.9A). Stacked turbidites represent the closed vertically juxtaposed deposits of two or more such flows (Fig. 3.9B); the close spacing is taken to imply short inter-flow time durations. Amalgamated turbidites (Fig. 3.9C) are compound deposits of two (or more) flows in which the later flow eroded into the deposits of the earlier flows. Pulsed turbidites (Fig. 3.9D) are the deposits of multi-pulsed flows whose individual pulses have interacted. Depending on the cause of the pulsing, during early pulse interaction (e.g., Fig. 3.9D-i), each deposition interval may be similar to a single turbidite, but without any evidence that might indicate a period of flow inactivity between each one (e.g. turbidite mud or hemipelagite). When the pulses have significantly interacted (e.g., Fig. 3.9D-ii) the time separation between them, and thus the vertical separation of cycles in the deposit, will be reduced. Note: the terms pulsed and stacked turbidites are used here regardless of the originating mechanism of the pulses or whether pulses have distinct mineralogical character.

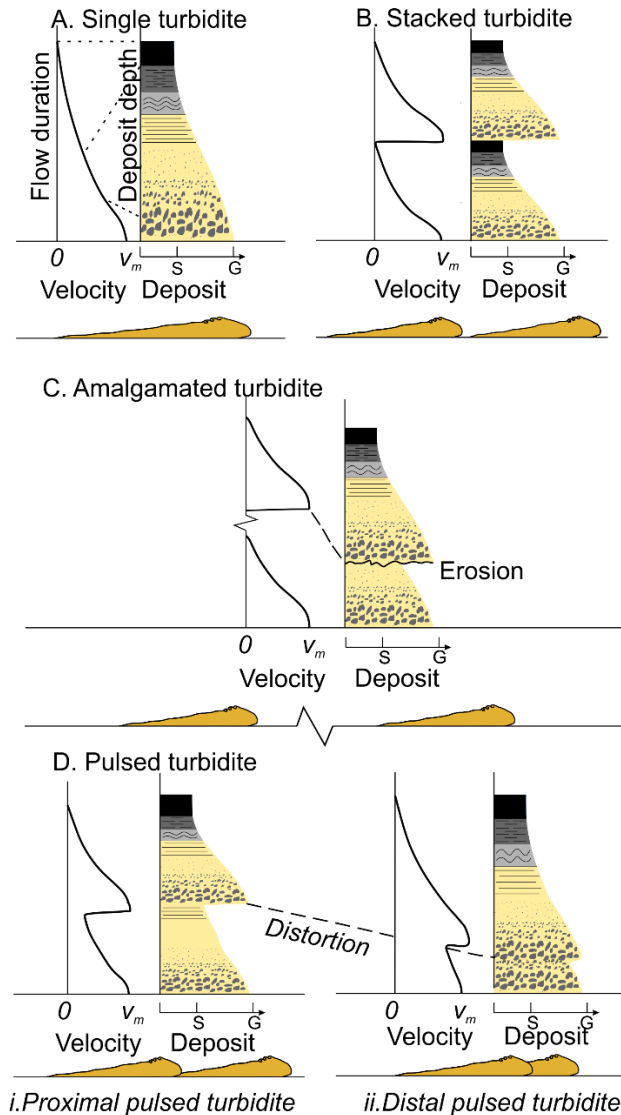


Figure 3.9 - Conceptual models illustrating the depth-averaged velocity-time profile for various turbidity current configurations and their inferred deposits. A) A single-pulse turbidite with an upward fining grain size profile. B) Stacked turbidites comprising two single-pulsed turbidities with a presence of Bouma Te (silt or clay layer) in between. C) Amalgamated turbidite with sharp interface between different inverse-to-normal grading cycles due to the erosion of a latter flow into the deposit of an earlier flow. D) Pulsed turbidites at relatively proximal and distal locations. Note: i) the lack of linear correspondence between the time and depth records (shown schematically for Fig. 3.9A, and implied for Fig. 3.9B-D); ii) pulsed turbidites

might have internal erosion surfaces instead of (or in addition to) inverse grading depending on pulse strength.

The initial delay times between different pulses in a multi-pulsed flow depend on the flow generation mechanisms. For a flow initiated by a series of retrogressive submarine landslides, each pulse can be linked to a discrete slumping episode and thus the delay times between individual pulses are controlled by the timing between successive failures. This timing may relate to the natural rate of slope instability propagation, but for a flow initiated by a single large multi-pulsed earthquake or by closely spaced initial shocks and aftershocks (e.g., Goldfinger et al., 2012), the delay times may relate to the spacing between different components of the seismic shock. When a multi-pulsed flow is formed by the combination at channel confluences of different single-pulsed turbidity flows, which were initially triggered synchronously in different channel heads, the delay time between pulses depends on the arrival time differences of the individual flows at the confluence (which depend in turn on channel lengths and intra channel flow velocities). The implications for deposit interpretation for each of these formation mechanisms are considered below.

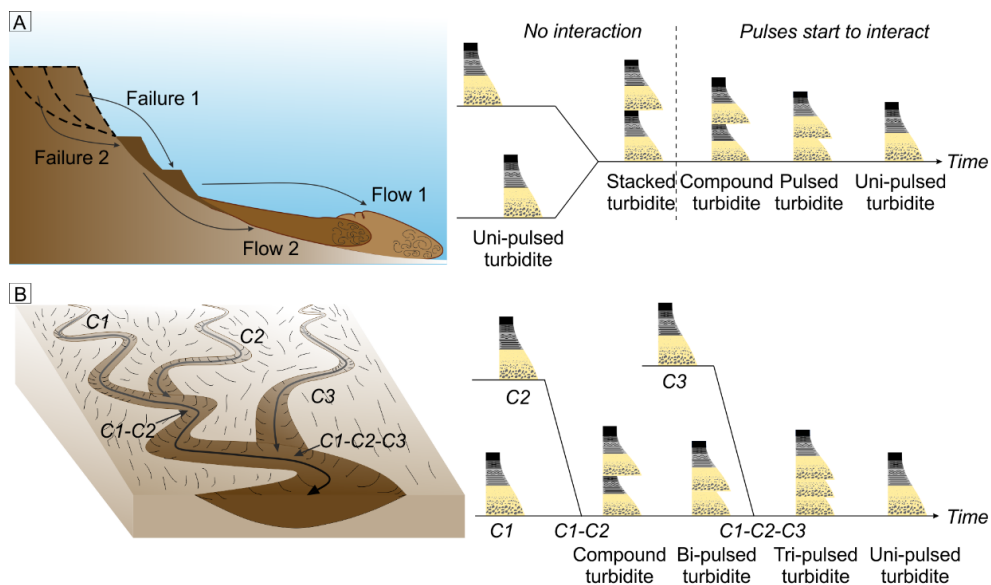


Figure 3.10 - Initiation mechanisms of multi-pulsed flows: A) Multi-pulsed flow triggered by retrogressive slope failures and conceptual turbidite patterns

for longer vs. shorter failure delays in the left-hand and right-hand panels, respectively and B) Tri-pulsed flow triggered by flow combination at channels, and possible turbidite grading patterns.

The depositional structure of flows initiated by retrogressive slope failures (whether seismically generated or not) is shown in Fig. 3.10A. If there is no initial interaction between the two single-pulsed flows, stacked turbidites could be expected to form proximally. If the flows start to interact, the second flow would behave as a second pulse in a combined flow, and would thus be advected progressively towards the front of that flow. The vertical depositional structure would transition along the flow pathway from having a stacked to multi-pulsed character, finally becoming uni-pulsed (or single-pulsed) after the point of pulse merging. When initially distinct flows combine at confluences, the longitudinal variation in the vertical grading structure of associated turbidites is expected to be similar to that postulated in Fig. 3.10A, but with an additional pulsing character acquired at the point of combination. In Fig. 3.10B a case is shown in which flows are triggered synchronously in each of three channels C1, C2 and C3 but take different times to reach their first downstream confluence. This 3D model is extrapolated from the 2D experimental configuration. The actual deposit character will vary depending on the magnitude of each pulse and the nature of the setting. For example, a bi-pulsed flow is shown forming at the C1-C2 confluence, and persisting to the C1-C2 to C3 confluence, where it merges with the flow in C3 to make a tri-pulsed flow that eventually evolves into a uni-pulsed flow. However, had the constituent pulses of the flow formed at the C1-C2 confluence already merged before the C1-C2 to C3 confluence, uni-pulsed flows in channels C1-C2 and C3 would have combined to make a bi-pulsed flow, depositing a bi-pulsed turbidite immediately downstream, and a uni-pulsed turbidite more distally. If the delay times between flows were sufficiently long to prevent their interaction single turbidites would be deposited in each of channels C1, C2 and C3, two stacked turbidites would be deposited downstream of the C1-C2 confluence and three downstream of the C1-C2 to C3 confluence. In complex natural settings, multi-pulsed turbidity currents can be generated by both

retrogressive slumping, with pulse timing either dictated by the timing of seismic shaking or by unforced slope failure processes, and by flow combination at confluences of flows that may or may not have a primary pulsed character.

It should be noted that the depositional models proposed in Fig. 3.10 disregard the effects of flow bypassing (e.g., Stevenson et al., 2013; Talling, 2013) or erosion and of local topography features (Eggenhuisen et al., 2010). Were bypassing or erosion to occur during flow run-out, some parts of the vertical grading profiles described in the figure might be partially or fully absent, with concomitant increases in deposit thicknesses further downstream.

3.4.3 Seismo-turbidites

Earthquake-triggered turbidites are commonly deposited along large, active tectonic margins such as Cascadia and Sumatra (Goldfinger et al., 2007; St-Onge et al., 2012). The deposits of flows generated in this way are called “seismo-turbidites” (*sensu* Shiki et al., 2000, and references therein). Here the potential application of the conceptual models described above is investigated, both to refine models of flow evolution and to suggest new interpretational options. Sumner et al. (2013) documented drop-core – derived records of Holocene turbidites deposited on the southwest Sumatra margin, and consider whether they were seismically triggered. Of interest here are turbidites with complex grading patterns, such as those recovered from the updip 4MC and downdip 2MC locations (Fig. 3.11A). At the 4MC location a succession of three turbidite units without intervening hemipelagic sediments have a deposition motif that could be interpreted either as stacked turbidites (separate events, Fig. 3.9B), the interpretation favoured by Sumner et al. (2013), or as a tri-pulsed turbidite (one event, Fig. 3.9D), deposited by a single, pulsed, seismically generated turbidity current. The sequence of deposits at 2MC appears to comprise one thick basal turbidite and two much thinner overlying turbidites (Sumner et al., 2013); the overall upward-fining profile of the basal 2MC turbidite suggests that it is the deposit of a single-pulse flow (e.g., Fig. 3.10A). Sumner et al., (2013) did not correlate the downdip 2MC deposit to other turbidites found locally in the system

such as those at updip 4MC. The increase in depositional thickness at 2MC could be a result of the overpassing flow being erosional upstream, which would give the flow more sedimentation capacity upon reaching 2MC. Although this interpretation may correctly reflect that the 4MC and 2MC locations did not lie on the same fairway, an alternative explanation now permitted by the work detailed here is that the 4MC tri-pulsed turbidite and the uni-pulsed 2MC turbidite could represent the deposits of a single flow that was tri-pulsed at 4MC but evolved via pulse merging to be uni-pulsed at 2MC (Fig. 3.10). In this interpretation, the pattern of ground shaking that initiated the flow might be distinguishable in the deposits at 4MC, but have been shredded at 2MC.

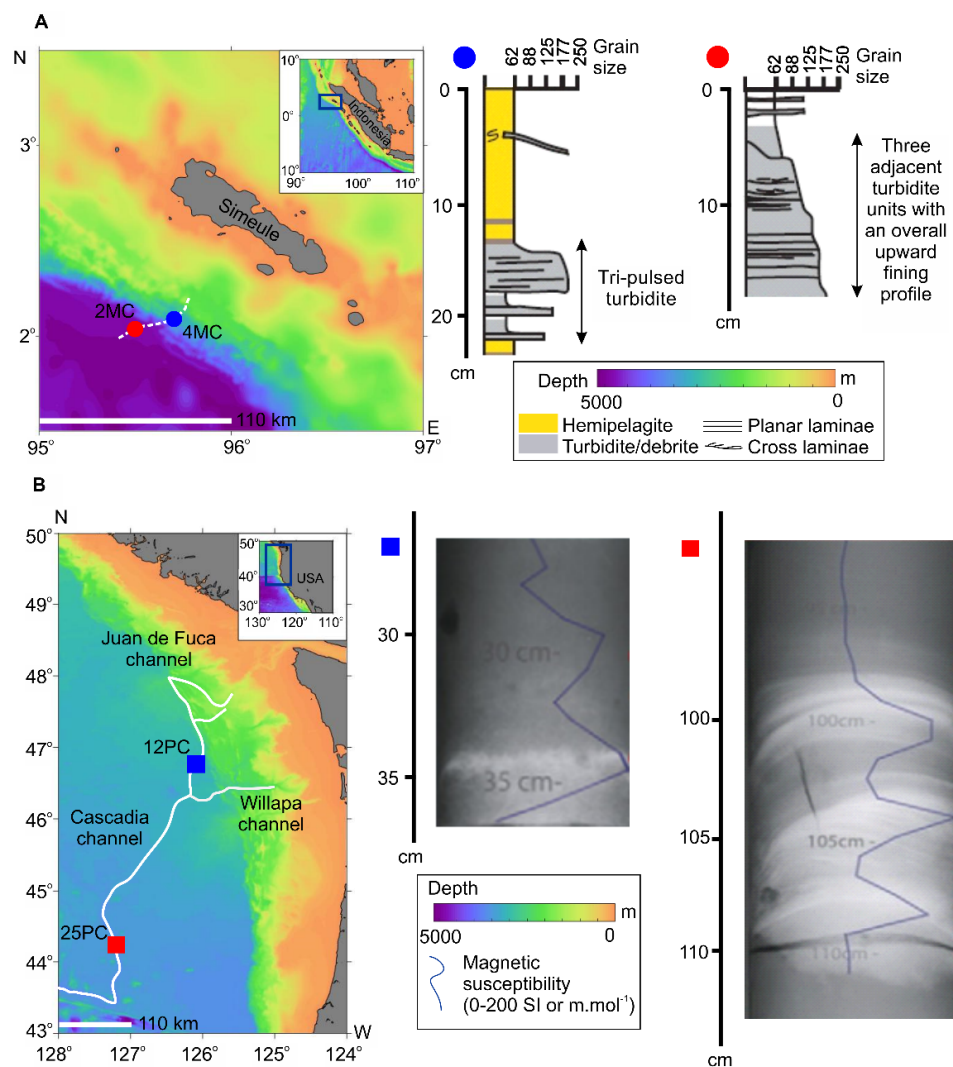


Figure 3.11 - Multi-pulsed turbidites A) offshore Sumatra at the 4MC and 2MC core locations (modified after Sumner et al., 2013), dashed curve shows

proposed channel conduit, unit of grain size is μm ; and B) in the linked Juan de Fuca and Cascadia channels at the 12PC and 25PC locations (modified from Gutiérrez-Pastor et al., 2013), white curve shows channel conduit (Goldfinger et al., 2016). Note: because grain size was estimated directly from the core, sediments finer than 62 μm cannot be distinguished (A). Magnitude of magnetic data reflect grain size of turbidites. Bathymetric data were taken from GebCO, 2014.

Cascadia channel is the channel that extends downstream from the confluence of the Juan de Fuca and Willapa channels (Fig. 3.11B; Goldfinger et al., 2016). Core-based studies of Holocene sediments suggest that great earthquake shocks/aftershocks commonly result in the deposition of multi-pulsed turbidites in the Cascadia Basin (Goldfinger et al., 2007; Gutiérrez-Pastor et al., 2013). For example, where the same number of turbidites are found in each of the tributary channels and downstream of the confluence of a linked channel system, it can be inferred that seismic events synchronously triggered turbidity currents in each of the tributaries, such that turbidity currents combined at confluences (Goldfinger et al., 2012). Thus, should the number of coarse-grained sediment intervals within a correlated bed increase downstream of a confluence, the extra pulses were likely generated by a flow combination mechanism similar to that outlined in Fig. 3.10B. Figure 3.11B provides an example of such an increase, in which the “T3” bi-pulsed turbidite found at the 12PC location in the upstream Juan de Fuca channel is correlated with a tri-pulsed T3 at the 25PC location in the downstream Cascadia channel. Turbidites were correlated using X-ray radiographs (see Gutiérrez-Pastor et al., 2013) by placing them in relative sequence to the distinctive, ash-rich first post-Mazama turbidite, and by relating the thicknesses of intervening hemipelagic intervals. The thickest interval of coarse sediments at 25PC is attributed to a single pulse flow component derived from the Willapa channel that mixed with a bi-pulsed flow from the Juan de Fuca channel (Fig. 3.11B; Gutiérrez-Pastor et al., (2013). Gutiérrez-Pastor et al., (2013), Goldfinger et al., (2008), Goldfinger et al., (2012) and Patton et al., (2015) recognized that the pattern of pulsing seen in the majority of Holocene and late Pleistocene turbidites

correlated along the Cascadia margin appears to be consistent within each deposit. They interpret the multi-pulsed character of these beds to indicate flow initiation by the large magnitude ($M > 9$) seismic events that characterize this margin. In this interpretation the apparent spatial persistence of pulsing character is contrary to the expectation of pulse merging described above. Either the pulses arise another way, the pulse merging phenomenon observed at laboratory scale does not occur within larger scale turbidity currents, or the merging length scale in such natural settings is longer than the spacing of sample locations. Further work is required to assess these possible explanations.

3.5 CONCLUSIONS

Physical modelling of multi-pulsed, solute density flows suggest that under most circumstances individual pulses within such flows must be advected forwards through the flow until they merge with the flow head. In natural dilute particulate gravity currents (turbidity currents), such pulsing flow structure may be acquired at flow initiation and be represented in any deposits by an interval of inverse grading (i.e., upwards coarsening) for each pulse. Assuming that such pulses are progressively advected towards the flow front within natural turbidity currents, a progressive reduction in the time between pulses is expected in progressively more distal locations, eventually decreasing to zero when the pulse merges with the flow head. Therefore an original pulsing signal might be relatively accurately preserved proximally, become progressively distorted up to the point of merging where the signal is completely lost ("signal shredded"). This may explain why normal grading is the predominant turbidite grading style in distal locations. Pulsing flow character may also arise when synchronously triggered flows combine at confluences; forward pulse advection will also progressively distort then shred pulses of this character. In natural settings, such as the Cascadia margin, the development of flow pulsing has already been inferred from the grading patterns within turbidites deposited downstream of confluences. The possibility that multi-pulsed flows may evolve spatially to become uni-pulsed can be invoked in studies of turbidites deposited on the southwest Sumatra margin,

and permits a wider range of potential correlations to be considered. The multi-pulsed saline flows presented in this paper show that pulse merging is effectively inevitable whilst interacting primary and secondary pulses remain active. Given that waning flows suggest upward fining deposition and waxing flows suggest the opposite, the extrapolation to predict the depositional patterns of pulsed turbidites appears reasonable. Nevertheless, the extrapolation should ideally be supported by experimental models of sediment-bearing flows together with a scaling analysis to more robustly link the characteristic lengths of pulse merging at laboratory scale and those at natural system scale. These subjects are presented in the next two chapters.

Chapter 4

Scaling analysis of multi-pulsed turbidity current evolution, with application to turbidite interpretation

Deposits of submarine turbidity currents, turbidites, commonly exhibit upward-fining grainsize profiles reflecting deposition under waning flow conditions. However, more complex grading patterns such as multiple cycles of inverse-to-normal grading are also seen and interpreted as recording deposition under cycles of waxing and waning flow. The depositing flows are termed multi-pulsed turbidity currents, and their deposits pulsed or multi-pulsed turbidites. Pulsing may arise at flow initiation, or following downstream flow combination. Prior work has shown that individual pulses within multi-pulsed flows are advected forward and merge, such that complex longitudinal velocity profiles eventually become monotonically-varying, although transition length-scales in natural settings could not be predicted. Here the first high frequency spatial (vertical and streamwise) and temporal measurements of flow velocity and density distribution in multi-pulsed gravity current experiments are presented. The data support both a process explanation of pulse merging and a phase-space analysis of transition length-scales. In prototype systems the point of pulse merging corresponds to the transition in any deposit from multi-pulsed to normally-graded turbidites. The scaling analysis is limited to quasi-horizontal natural settings in which multi-pulsed flows are generated by sequences of relatively short (<10 km long), progressively up-dip sediment failures, predicting pulse merging after only a few 10s of kms. The model cannot provide quantitative estimation of merging in down-slope flows generated by axially-extensive (>10 km) sequences of breaches or where pulsing arises from combination at confluences of single-pulsed flows. Such flows may be responsible for the pulsing signatures seen in some distal turbidites, >100 km from source.

4.1 INTRODUCTION

Turbidity currents are a form of dilute sediment-bearing gravity flows and they play a key role in the transportation of clastic sediments from continents to deep seas (Simpson, 1982; Piper & Savoye, 1993; Xu et al., 2004; Palanques et al., 2006; Carter et al., 2012; Hughes Clarke et al., 2012). Such currents are driven by gravitational force resulting from the suspension of sediments within the interstitial fluid (Middleton, 1993; Huppert, 1998; Kneller & Buckee, 2000; Sequeiros, 2012).

Sediments deposited from turbidity currents, turbidites, build some of the largest sedimentary landforms on the planet (Canals et al., 2004; Xu, 2011; Lintern et al., 2016). Vertical grading patterns of deposits from individual turbidity current events reflect overpassing flow dynamics (Hand, 1997; Kneller & McCaffrey, 2003; Goldfinger et al., 2012; Stevenson et al., 2013). With the assumption that sediments aggrade progressively from overpassing flows, normally graded turbidites are deposited by flows with an abrupt waxing and a progressively waning velocity structure (Bouma, 1962). In the initial waxing flow regime, the current is weakly depositional, corresponding to its short duration relative to that of the waning phase. Thus, the basal layer comprises only a thin, or no, record of inverse grading (Hand, 1997). However, vertical grainsize profiles of some turbidites are considerably more complex, with single deposits exhibiting multiple intervals of inverse-to-normal graded sediment. These deposits are referred to as pulsed or multi-pulsed turbidites (i.e., Goldfinger et al., 2012; Ho et al. 2018a).

Many seismically triggered turbidites, generated at active tectonic margins, exhibit this complex vertical grading pattern (Gutiérrez-Pastor et al., 2013; Sumner et al., 2013). These turbidites are interpreted as being formed by multi-pulsed turbidity currents with repeated waxing-waning velocity structure (i.e., Kneller & McCaffrey, 2003; Ho et al., 2018a), assuming that flow shear stress is positively correlated with mean velocity, and that a wide enough range of grain sizes is carried in the flow such that progressively coarser grains (mainly carried by the head) fall from suspension at a point as it waxes. Repeat pulses in turbidity

currents can be generated by: i) retrogressive slope failures initiated by seismic shaking variations in pulsed earthquakes (Goldfinger et al., 2012; Beeson et al., 2017); ii) shock/aftershock events (Johnson et al., 2017); iii) the combination of multiple single flows at confluences (Nakajima & Kanai, 2000; Ismail et al., 2016); or iv) variation in discharge of hyperpycnal-fed turbidity currents (Mulder & Alexander, 2001). Delay time between different seismically generated pulses can range from minutes to hours (e.g., Hsu et al., 2008; Lupi & Miller, 2014).

Laboratory experiments were conducted previously to model pulsing in denser-than-ambient gravity currents (see Chapter 3). At laboratory scale, saline flows were used as a proxy for turbidity currents driven by the suspension of fine-grained low-settling velocity particulate material (Felix, 2002; Meiburg & Kneller, 2010; Ferrer-Boix et al., 2015). Results from these experiments indicate that individual pulse components within a multi-pulsed flow inevitably merge at some distance from the source, and that the longitudinal velocity structure of the flow transforms from being cyclically-varying to monotonically-varying with increasing time and space (Chapter 3). Therefore, up to the point of merging multiple coarsening-upward intervals might be expressed in the deposit, whose spatial separation might progressively reduce up to that point. Downstream of the merging point, deposits should be normally graded.

Here, the analysis presented in Chapter 3 (i.e., Ho et al., 2018a) is advanced in order to assess the scaling between multi-pulsed gravity current experiments and prototype environments. Such analysis is essential to assess whether the merging phenomenon is expressed in the geological record, and if so, over what range of scales. An extensive series of lock-exchange saline experiments was conducted to study a complete phase space of boundary conditions, from which a robust scaling analysis was developed. This enables the first empirically-grounded test of the natural scale of the merging phenomenon to be undertaken. This chapter (i.e., Ho et al., 2018b) presents i) experimental data detailing the dynamical variations of single-pulsed flows and multi-pulsed flows, ii) numerical analysis of the interdependence of non-dimensional parameters characterizing initial flow conditions and the merging phenomenon, iii) discussion regarding

reasonable timescales over which the generation of multi-pulsed flows could be possible and iv) examples of natural turbidite interpretations in which the analysis effectively provides a tool to estimate the spatial persistence of pulsed turbidites.

4.2 METHODOLOGY

Experiments were run in order to: i) establish that pulses within multi-pulsed flows eventually merge (across a relatively wide range of boundary conditions considered); and ii) support a scaling analysis that links experimental and real-world merging scales.

4.2.1 Experimental set-up

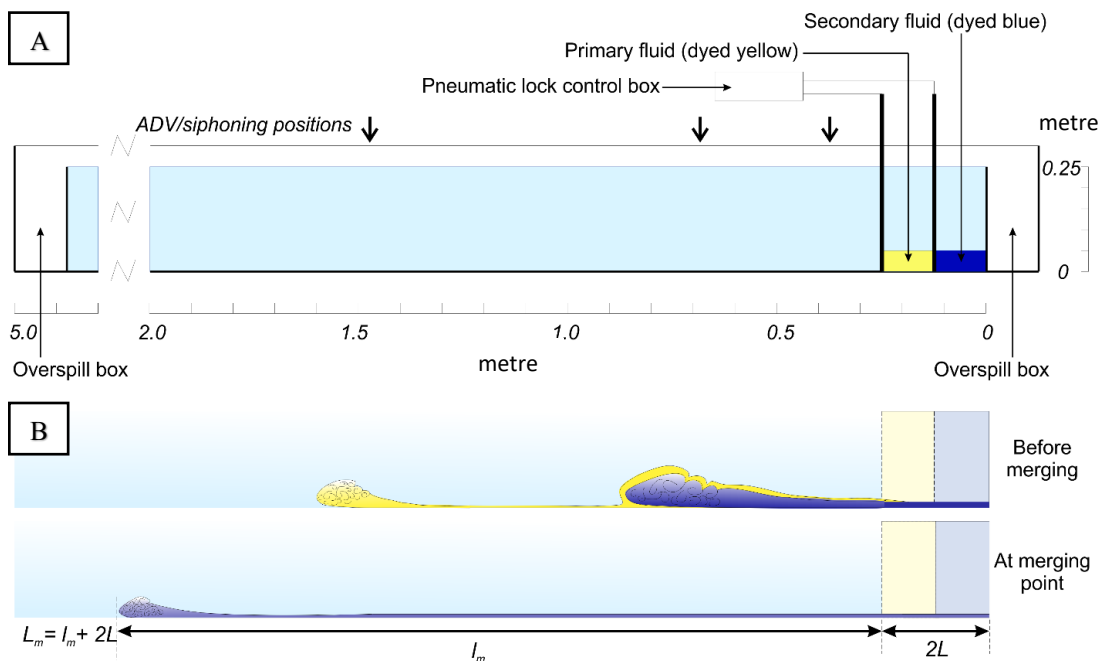


Figure 4.1 - A) Sketch of experimental set up (adapted from Ho et al., 2018a). Note:

- i) three arrows sketched along the top of the flume indicate positions of ADV/siphoning instrumentation, ii) two cameras were set up on a track fixed in front of the flume, iii) initial flow height $h=0.05$ m (see vertical scale bar).
- B) Flow propagation model with lock length, L , merging length, l_m , and total merging length, L_m , highlighted.

Experimental gravity currents were developed from the lock-exchange release of a denser than ambient (saline water) fluid into an ambient (tap water) (see for examples Middleton, 1966; Holyer & Huppert, 1980). Denser-than-ambient saline

flows were experimentally modelled in a 5 m long flume with two lock boxes set up at one end which enabled the generation of multiple flow pulses in series (Fig. 4.1A), based upon the method of Chapter 3. The dynamics of saline flows approximate the dynamics of fine-grain dominated turbidity currents (i.e., Kneller & Buckee, 2000; Islam & Imran, 2010; Hogg et al., 2016). The speed of the lock gate lift was set by a pneumatic ram at 1.0 m/s in order to minimize turbulent mixing caused by the withdraw. The timing between each gate was set by an electronic timer, ensuring experiment repeatability. Effects of returning waves upon the slumping of dense fluid in the lock boxes were minimized by deploying two overspill boxes, one at each end of the flume. Two flow pulses were dyed yellow and blue to enhance the visualization and recorded using two cameras which could be independently moved laterally in front of the flume; each camera tracked one flow component. In order to study dynamical variations of single- and multi-pulsed flows in detail, time-series of streamwise velocity and density data were collected for three characteristic flows of 0.125 m lock length. Furthermore, to underpin a scaling analysis of the flow merging phenomena, a series of experiments was conducted that confirmed individual pulses in multi-pulsed flows eventually merge over a wider range of conditions (see section 4.2.2).

Single-pulsed (0 s delay time), short and long delay time multi-pulsed flows were modelled. Such flows of three different delay times between pulses are thought to act as proxies for natural full-scale counterparts whose delay times can range between zero and several hours (e.g., Hsu et al., 2008; Lupi & Miller, 2014; Goldfinger et al, 2017). Single-pulsed flows were initiated by the instantaneous release of both lockboxes. Short delay time flows were those in which fluid contained in the second lockbox was released when the ratio between the height of that in the first lockbox and the original height had decreased to between 0.5 and 0.25. In long delay time flows, a second pulse was released after the dense fluid in the first lockbox had already fully collapsed and at that point the first pulse had travelled to a distance of c. 11 lock lengths. Excess density, ambient height and flow depth in all experiments were kept at 5% (fluid density 1050 kg m^{-3}), 0.25 m and 0.05 m respectively in order to maintain a turbulent flow condition ($Re \sim$

4000). The ratio of initial flow depth/ambient was 0.2 which approximates to a real-world scale of c. 0.13 in deep marine turbidity currents (Piper et al., 1988; Talling et al., 2013; Xu et al., 2014).

Velocity and density sampling was undertaken for three characteristic short lock length flows of $L = 0.125\text{ m}$, $H = 0.25\text{ m}$, $h = 0.05\text{ m}$ and $\Delta t = 0\text{ s}$, 4 s , 15 s . These three delay time settings characterize single-pulsed, short and long delay time flows respectively. Acoustic Doppler Velocimetry (ADV) was used to capture vertical variations in horizontal velocity (Craig et al., 2011; MacVicar et al., 2014; Brand et al., 2016; Thomas et al., 2017). The ADV probe was set at 7.1 cm above the flume bed, capturing a flow depth of 2.5 cm. Both the saline and ambient water were seeded with 10 micron hollow glass spheres to generate acoustic reflection. A siphoning technique was adopted to collect samples of flow fluids, using a multichannel peristaltic pump connected to an array of seven 2mm-diameter siphoning tubes, centered at 5 mm intervals to collect data from 0.5 to 4 cm above the channel bed. Samples were collected every 2 seconds over a period of 20 seconds and contained in an array of sample trays. Transit time for fluid to travel from the siphoning probe to the sample trays was 12s. The time when the flow reached the probe was recorded (as t) and matched with that when the first sample was collected (as $t+12$). The conductivity and temperature of each sample were measured using a Mettler-Toledo InLab 752-6 mm conductivity probe (Mettler-Toledo, 2017). The measurements were then used to calculate excess density based on standard algorithms for brine (see e.g., Janz & Singer, 1975; Unesco, 1983). Experimental data were acquired at three locations: i) proximally to source (0.365 m), ii) relatively proximally (0.675 m) to the point of merging and iii) distally from source (1.465 m) (Fig. 4.1).

4.2.2 Scaling analysis

4.2.2.1 Experimental parameters

The scale dependency of flow merging on initial flow conditions is tested by varying experimental parameters. The only physical parameters that characterize

the experimental multi-pulsed flows are: initial flow height (h), ambient height (H), lock length (L), reduced gravity of dense fluid (g'), delay time (Δt), kinematic viscosity (ν) and merging length (L_m), see Table 4.1. The total merging length L_m is given by the sum of the distance downstream from the first lock gate at which the pulses merge, l_m , plus the initial flow length (i.e., twice the lockbox length), see Fig. 4.1B. The reduced gravity of the dense fluid is given by $g' = \frac{\rho_f}{\rho} - 1$, where ρ_f and ρ denote densities of the dense fluid and the ambient. To establish a method of estimating merging length in natural settings, initial boundary conditions were systematically varied, including lock length, ambient water height and delay time between two pulses (Tables 4.1 & 4.2). Flow density and initial (lockbox) height were fixed at $\rho_f = 1050 \text{ kgm}^{-3}$ and $h = 0.05 \text{ m}$ respectively. In order to confirm the consistency of merging lengths observed in each experiment, a number of selected experiments were repeated so that relative errors in their resultant merging lengths could be assessed (Table 4.3); mean relative error was then calculated to confirm the repeatability of the experiments. Specifically, experiments of the same initial settings were run several times to see how merging lengths vary. In total 79 experiments were conducted.

The height of the flow exiting the lockbox was proportional to h . From this, a velocity scale of the gravity current head is given by a Froude number condition (i.e., equation (4.1); Huppert & Simpson, 1980),

$$(4.1) \quad U = \sqrt{g'h}$$

The dimensionless ratio between inertial, Uh , and viscous forces, ν , (i.e., the Reynolds number) was $Re = 4000$. Thus, the flows were assumed to be fully turbulent and viscous affects were considered negligible.

Table 4.1 - Experimental parameters deployed to underpin a scaling analysis

Parameter	Value		
Lockbox length, L	0.125 m	0.25 m	0.375 m
Lock release delay time, ΔT	1-34 seconds	1-67 seconds	7-107 seconds
Gravitational buoyancy, g'	0.4905 m/s ²		
Ambient height, H	0.10, 0.125, 0.167, 0.25 m		
Initial flow height, h	0.05 m		

In order to link the scales of experimental parameters to those of prototype environments, a non-dimensional approach was deployed to model the experimental data by using Buckingham Pi theory. The principle of the theory is that an equation describing a physical system in terms of n dimensional parameters can be expressed by an equation of $n-k$ parameters, where k denotes the number of unique physical dimensions involved (e.g., Buckingham, 1914; Miragliotta, 2011). Here it is argued that the merging length, L_m , over which individual pulses in multi-pulsed gravity currents combine, must be an unknown function of the original six unknown variables,

Table 4.2 - Dimensionless parameter groupings

Dimensionless group	Experimental values
Buoyancy scale, $\Pi_1 = \sqrt{g'h}/\frac{L}{\Delta t}$	Varied between 0-45
Flow aspect ratio, $\Pi_2 = h/L$	0.13, 0.20, 0.40
Lockbox aspect ratio, $\Pi_3 = H/L$	0.27, 0.33, 0.4, 0.5, 0.67, 0.8, 1, 1.3, 2
Merging length scale, $\Pi_4 = l_m/L$	collected from experiments

$$(4.2) \quad L_m = f(L, h, H, g', v, \Delta t)$$

By assuming that viscous effects are negligible, equation (4.2) can be reduced to a relationship between four dimensionless groupings, including: the merging length scale ($\Pi_4 = \frac{l_m}{L}$); the flow buoyancy scale ($\Pi_1 = \frac{\sqrt{g'h}}{L/\Delta t}$); the initial flow aspect ratio ($\Pi_2 = \frac{h}{L}$); and the lockbox aspect ratio ($\Pi_3 = \frac{H}{L}$). These dimensionless parameters are thought to sufficiently capture both initial flow

conditions and variation of merging lengths. Here, h is kept constant so as to prevent overcomplicating the experimental set-up given that varying other parameters effects a variation in initial flow conditions within the modelled non-dimensional parameters; i.e., partial flow height h/H is varied upon varying H . The merging length scale is defined as the ratio between the experimentally observed merging length in each experiment, measured from the front of the first lockbox to the point of merging, and one lock length used in that experiment (Fig. 4.1B). Translating this to the real-world, the merging length scale describes the magnitude of merging length relative to the initial dimension of the corresponding slumping breach. Total merging length is then defined by equation (4.2). The buoyancy scale describes flow velocity, equation (4.1), normalized by the velocity scale necessary for a flow to translate one lock length during the delay time Δt . The two other ratios define the scales of the flow itself and of the ambient water, relatively to the lock length. The principal goal of this scaling analysis is to seek a mathematical correlation – function F , based on numerical analysis, which describes the dimensionless merging length (Π_4) as a function of other dimensionless parameters (see equation (4.3) and Table 4.2).

$$(4.3) \quad \Pi_4 = F(\Pi_1, \Pi_2, \Pi_3)$$

4.2.2.2 Data Fitting

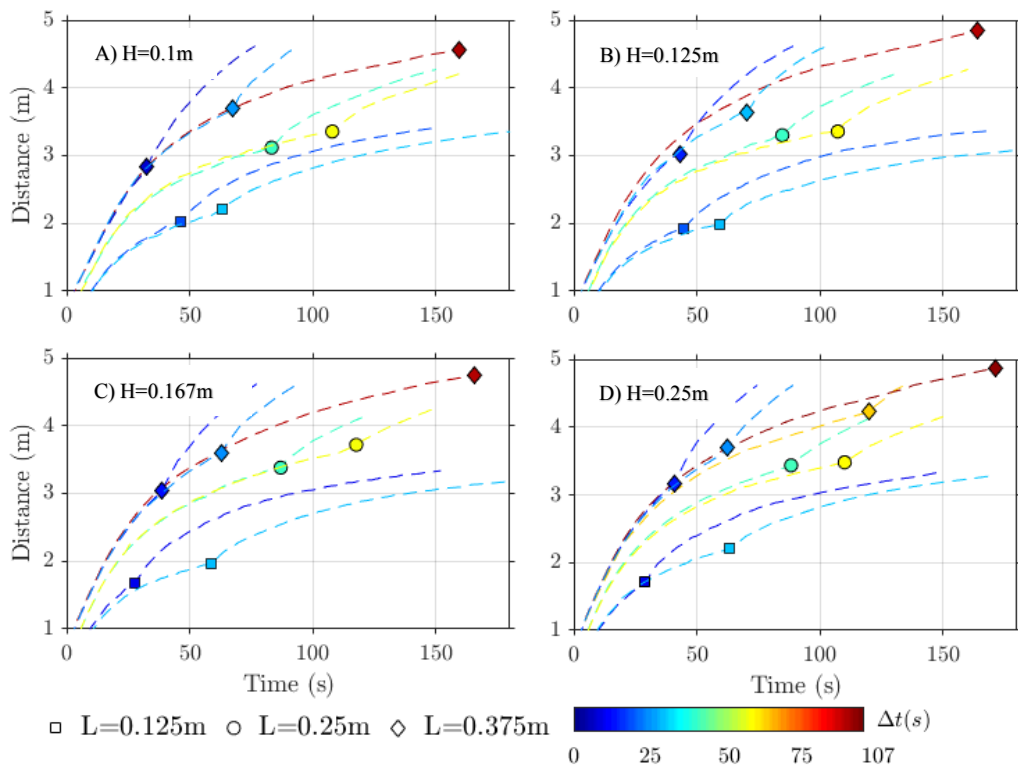


Figure 4.2 - Front positions of some flows plotted based on different ambient heights A) 0.1 m, B) 0.125 m, C) 0.167 m and D) 0.25 m. Note: symbols on plots highlight points of merging in each experiment.

When varying initial flow parameters (Tables 4.1 and 4.2), the evolution of multi-pulsed flow fronts, and thus the merging lengths, varied significantly (Fig. 4.2). In Fig. 4.2, for flows of the same lock length (denoted by symbols) and ambient height (shown in each plot), pulses were seen to merge at further distances as delay times between the two lock gates increased. However, a simple correlation between merging lengths and any of the initial parameters is not directly observed from the raw data; it is not possible to simply visualize the variation of the data set comprising four varying parameters. Neither experimental repeatability (variability in merging length) nor the reliability of the experimental set-up (variability in actual lock release delay times) can be implicated in the absence of simple correlations; relative errors of merging lengths observed in repeated

experiments were insignificant (average 2.7%) and mean relative error in lock release delay times was small (average 6.21%) (Table 4.3). In the absence of a simple correlation between the merging length and initial parameters, a numerical regression of the dimensionless merging length scale with respect to the dimensionless parameters characterizing the initial flow conditions was conducted.

The principal goal of the analysis was to test the interdependence of all parameters. Here a log-scale transform of the data was employed

$$(4.4) \quad P_{ij} = \log(\Pi_{ij}) \text{ for } i = 1 \text{ to } 4 \text{ and } j = 1 \text{ to } J = 79$$

to account for the possibility of non-linear relationships between the dimensionless parameters. This enabled linear regression analysis of the log-transformed data, of the form

$$(4.5) \quad P_{4j} = aP_{1j} + bP_{2j} + cP_{3j} + d$$

to be conducted, where a, b, c and d are the coefficients to be determined. A least-squares method was used to minimize the vector

$$(4.6) \quad \delta_j(a, b, c, d) = (aP_{1j} + bP_{2j} + cP_{3j} + d) - P_{4j}$$

containing the log-transformed experimental data, P_{ij} , collected from all $J = 79$ experiments. Here the function δ_j describes the differences between numerically estimated (1st term on the right hand side of equation (4.6)) and experimentally observed (2nd term on the right hand side of equation (4.6)) log-transformed dimensionless merging lengths. Matlab's™ numerical nonlinear data-fitting solver, *lsqnonlin*, was used to find the optimal solution of equation (4.5) by simultaneously varying a, b, c and d to find the global minima across all experiments conducted, defined by A, B, C and D ,

Table 4.3 - Repeated experiments and error analysis

Lockbox length (m)	Flow height (m)	Ambient height (m)	Nominal delay time (s)	Actual delay time (s)	Total merging length (m)	Relative error of delay time (%)	Relative error of merging length (%)
0.125	0.05	0.167	1.5	1.25	0.911	16.7	8.68
				1.6	1.084	6.67	8.68
0.125	0.05	0.25	0.5	0.38	0.807	24	1.88
				0.67	0.777	34	1.88
0.125	0.05	0.25	4	4.1	1.297	2.5	0.18
				4	1.300	0	0.06
				4	1.295	0	0.33
				4	1.305	0	0.44
0.125	0.05	0.25	11.5	11.1	1.713	3.48	0.14
				11.4	1.708	0.87	0.14
0.125	0.05	0.25	22.5	22.3	2.069	0.89	2.33
				22.2	1.975	1.33	2.33
0.125	0.05	0.25	34	33.5	2.094	1.47	2.42

				34	2.198	0	2.42
0.375	0.05	0.125	16	15.5	3.024	3.13	4.61
				16.7	3.317	4.38	4.61
					Mean	6.21	2.57
					Standard deviation	9.65	2.72

$$(4.7) \quad \min(\sum_{j=1}^J \delta_j(a, b, c, d)^2) \equiv \sum_{j=1}^J \delta_j(A, B, C, D)^2$$

A test of initial conditions revealed that numerical solutions were independent of the starting point chosen, suggesting a single global minimum of equation (4.6) (see further section 4.3.2). Starting points for the scalar variables a - d in the numerical minimization of equation (4.6) were thus set to unity. During each iteration step, the solver simultaneously varied and updated the four variables, using results obtained from a preceding iteration until the minimum least-squares error was found. Optimization, using the “*lsqnonlin*” solver, employed the Levenberg-Marquardt algorithm (i.e., Marquardt, 1963; Fan, 2003); the iteration process was terminated at a relative tolerance point of 10^{-6} . To evaluate the accuracy of the data fit, relative root mean square error (RMSE) was calculated by

$$(4.8) \quad RMSE = \sqrt{\frac{1}{J} \sum_{j=1}^J \left[\frac{AP_{1j} + BP_{2j} + CP_{3j} + D - P_{4j}}{P_{4j}} \right]^2}$$

4.3 RESULTS

In this section, two components of the experimental data are presented: i) a detailed description of the velocity and density data that, under the studied experimental configurations to model three characteristic flows (at $L = 0.125 \text{ m}$, $H = 0.25 \text{ m}$, $h = 0.05 \text{ m}$ and $\Delta t = 0\text{s}, 4\text{s}, 15\text{s}$), show the inevitability of merging of pulses within multi-pulsed flows of different delay times; and ii) a scaling analysis to quantitatively model such phenomenon based upon a variety of initial boundary conditions.

4.3.1 Flow dynamics

In this section, the dynamics of single-pulsed, short and long delay time flows are discussed by considering three examples of characteristic flows of short lock length (0.125 m) that were modelled.

4.3.1.1 Single-pulsed flow

In the single-pulsed flow experiments, the two flow pulses were released simultaneously. The total volume of fluid released was the same in size and density as the multi-pulsed flows, but only a single front developed. The flows exhibited the waxing-waning velocity structure commonly observed in other experimental and field-based studies (Fig. 4.3A; Britter & Simpson, 1978; Chapter 3). The velocity maximum of the flow was located at approximately 25% of the flow height above the channel bed as has been observed in previous experimental and field-based research (Kneller & Buckee, 2000; Talling et al., 2015).

Time-series of density profiles at three downstream positions show that the flow head was always denser than the body. It is inferred that the turbulent mixing between flow and the ambient water was more pronounced at the back of the head (Sher & Woods, 2015) consistent with the net forward advection of material into the head from the body (Kneller et al., 1999). This process resulted in the reduction in density of the fluid comprising the flows, which is shown by the considerable change in vertical gradient in fluid density within the first 10 seconds of each sampling period in Fig. 4.3A. Within the slumping phase, turbulent mixing and ambient water entrainment appeared significant (Fig. 4.3A, 0.365 m). As the flow travelled further downstream, it entrained more ambient fluid and thus flow density was generally reduced (Fig. 4.3A at 0.675 m, 1.465 m).

4.3.1.2 Short delay time flow

Proximally to source, the short-delay time flows exhibited two separate pulses in velocity profiles; the second pulse travelled faster than the first one (Fig. 4.3B, 0.365 m). As the second pulse was progressively advected towards the flow front, the temporal separation between the two pulses was progressively reduced and the magnitudes of internal fluid velocity of the two pulses became relatively comparable (Fig. 4.3B, 0.675 m). Once the two pulses had merged completely, the flow evolved in a manner similar to that of the single-pulsed flow (Fig. 4.3A-B,

1.465 m). The velocity maximum was also located at c. 25% of flow height as seen in the single-pulsed flow's velocity profile (Fig. 4.3B).

The advection of the second pulse as an intrusion (Chapter 3) within the first pulse is shown by an increase in flow density observed after the arrival of the flow front at the siphoning probe (Fig. 4.3B, 0.365 m, 5-10 s). As the second pulse progressively intruded into the first pulse, the two pulses progressively merged and the density profile observed became very similar to that of the single-pulsed flow at the same sampling position along the channel pathway (Fig. 4.3A-B, 0.675 m). The density of the second pulse was better preserved in comparison to that of the first pulse, presumably since the mixing between the two pulses was suppressed as it travelled as an intrusion into a denser-than-water ambient (i.e., the first pulse). As a result, the short delay time multi-pulse flows exhibited a relatively thick basal layer of high density (Fig. 4.3B, 1.465 m).

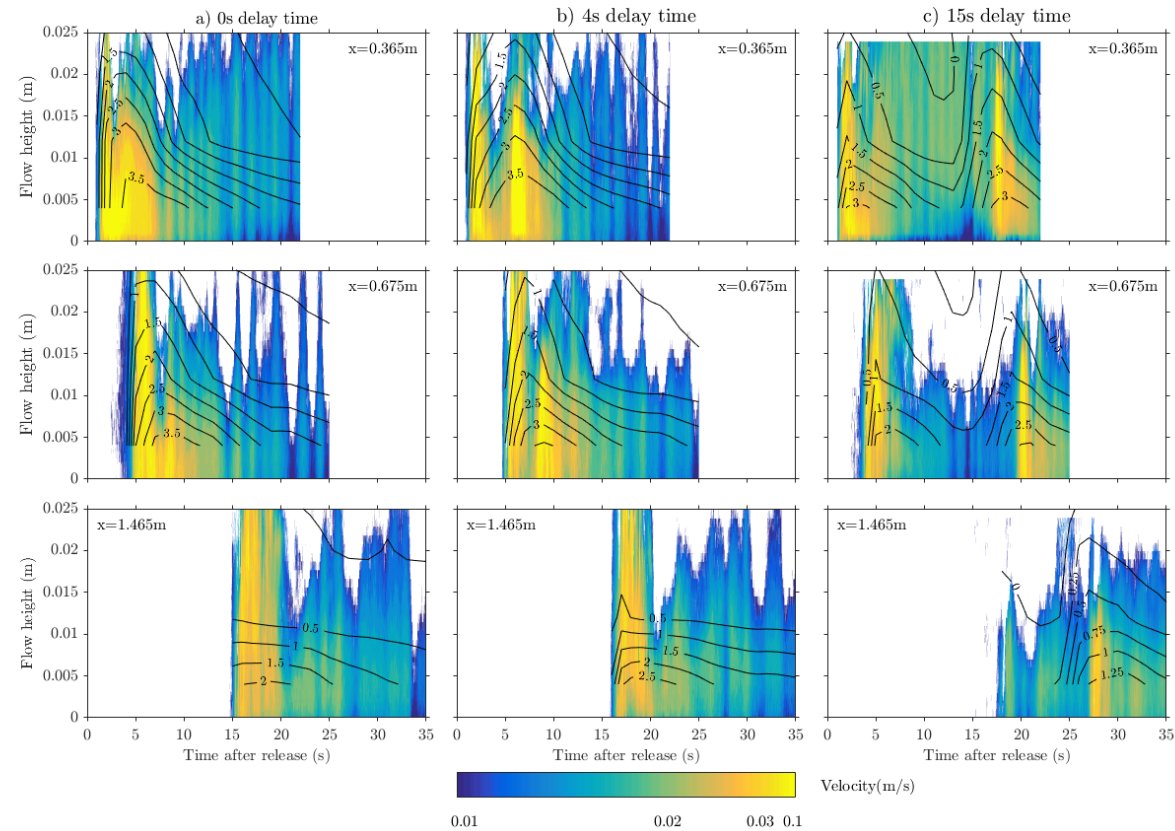


Figure 4.3 - Time-series velocity (contour fields) and density (contour curves) data collected from experiments of A) single-pulsed flow, B) short delay flow and C) long delay flow, in which $L = 0.125$ m, $H = 0.25$ m, $h = 0.05$ m. Note: i) contour curves show excess density in percentage, ii) vertical stripes indicate the effects of surface waves of small magnitude, iii) the x value shown on each plot indicates the position along the flume where the ADV/siphoning data were taken.

4.3.1.3 Long delay time flow

Proximally to source, the two pulses of the long delay time multi-pulsed flows each travelled at velocity of c. 0.1m/s (Fig. 4.3C, 0.365 m). As the flow evolved further from source, the velocity of the first pulse decreased significantly whilst the second pulse maintained a relatively high velocity (Fig. 4.3C, 0.675 m and 1.465 m). Thus, the second pulse was progressively advected towards the flow front. This is demonstrated by the reduction in temporal separation between the pulses (Fig. 4.3C). The ADV data show that the two pulses eventually merged to form a unified flow.

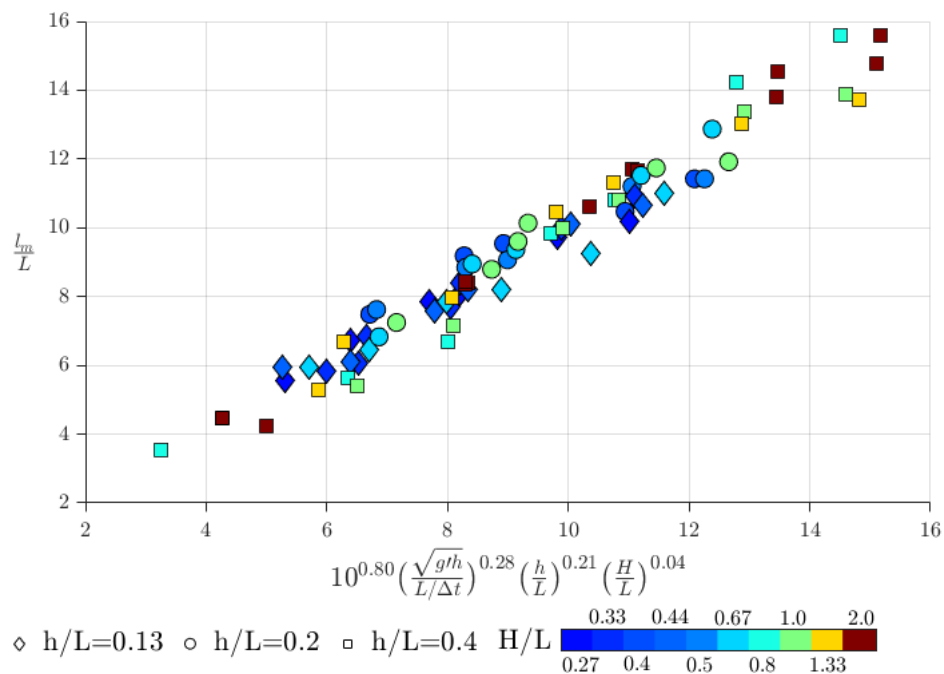


Figure 4.4 - Data regression showing merging length as a linear function of initial dimensionless parameters, obtained using Matlab'sTM numerical nonlinear data-fitting solver, *lsqnonlin*. Note: $R^2 = 0.96$, RMSE = 6.8%.

Prior to the arrival of the second pulse at the sampling position, the first pulse developed a thin layer of high density (Fig. 4.3C, 0.365 m, 0-10 s c. 0.004 m of 3% excess density). Following the second pulse release, both pulses had relatively dense bases (i.e., excess density of approximately 3% shown in Fig. 4.3C,

0.365 m). Further downstream from the source, the dense fluid comprising the second pulse had a higher density than that comprising the first pulse (i.e., Fig. 4.3C, 0.675 m, excess density 3% vs. 2%); the first pulse was significantly diluted because of ambient water entrainment. The whole flow generally became diluted with increasing time and space (Fig. 4.3C). Time-series density data also show the two pulses progressively merging as their temporal separation was progressively reduced (Fig. 4.3C).

4.3.2 Scaling analysis

By numerically solving equation (4.6), a line of best fit is determined that provides the best collapse of the dimensionless experimental data, where $A = 0.28$, $B = 0.21$, $C = 0.04$ and $D = 0.75$. By inverting the log-transform of equation (4.5), an equation is found for the merging length scale, l_m ,

$$(4.9) \quad \frac{l_m}{L} = 10^{0.75} \left[\frac{\sqrt{g'h}}{L/\Delta t} \right]^{0.28} \left[\frac{h}{L} \right]^{0.21} \left[\frac{H}{L} \right]^{0.04}$$

The associated RMSE for this data collapse is 6.8% (Fig. 4.4). However, for the dimensionless flow aspect ratios considered, equation (4.8) only has a weak dependence on the lockbox aspect ratio Π_3 . This motivates development of a model of the merging length scale of reduced complexity, that is independent of the ambient flow depth. To test this hypothesis of reduced complexity a correlation was sought that was independent of H/L . The same minimization approach, based on least-squared method, was used on the function

$$(4.10) \quad \delta_j(a, b, d) = aP_{1j} + bP_{2j} + d - P_{4j}$$

see equations (4.4)-(4.8). The optimal simplified scaling of the merging length incorporates only three dimensionless parameters; the lock box length, reduced buoyancy, and delay time,

$$(4.11) \quad \frac{l_m}{L} = 10^{0.70} \left[\frac{\sqrt{g'h}}{L/\Delta t} \right]^{0.25} \left[\frac{h}{L} \right]^{0.25}$$

and its RMSE showing the deviation between experimentally observed and theoretically estimated merging lengths is approximately 7% (Fig. 4.5). The difference between RMSE of the original and simplified data collapses, equations (4.9) and (4.11), is insignificant - only 0.2%. Furthermore, data fitting is insensitive to local variations; for A and B between 0.2 and 0.4, the RMSE resulting from any data regression changes by only 5% (Fig. 4.5). Figure 4.5 also shows the well-behaved character of the minimization function, equation (4.6), with a single global minimum in the domain $A, B \in [0 \dots 1]$.

This suggests that when the flow aspect ratio, h/L , is small the merging lengths scales are independent of the ambient depth. This may be because the hydrostatic pressure driving force of shallow partial release lockbox gravity currents is, similarly to turbidity currents occurring in natural settings, mainly controlled by the excess density between the flow and the surrounding ambient (i.e., Bonnecaze et al, 1993; Shin et al, 2004; Darby & Peakall, 2012).

4.4 DISCUSSION AND APPLICATION

4.4.1 Merging phenomenon

The variations in flow dynamics of both the short and long delay time multi-pulsed flows show that the signature of the intrusion of a second pulse within a multi-pulsed flow is preserved proximally to source, progressively distorted towards the point of merging and eventually shredded once pulses completely merge (Fig. 4.3; Ho et al., 2018a). Multi-pulsed flows of both short and long delay time evolve from being repeatedly waxing-waning to monotonically waning. Therefore, beyond the point of merging, such multi-pulsed flows of both delay time settings evolve in a similar manner to that of single-pulsed flows of equivalent volumes of dense fluid.

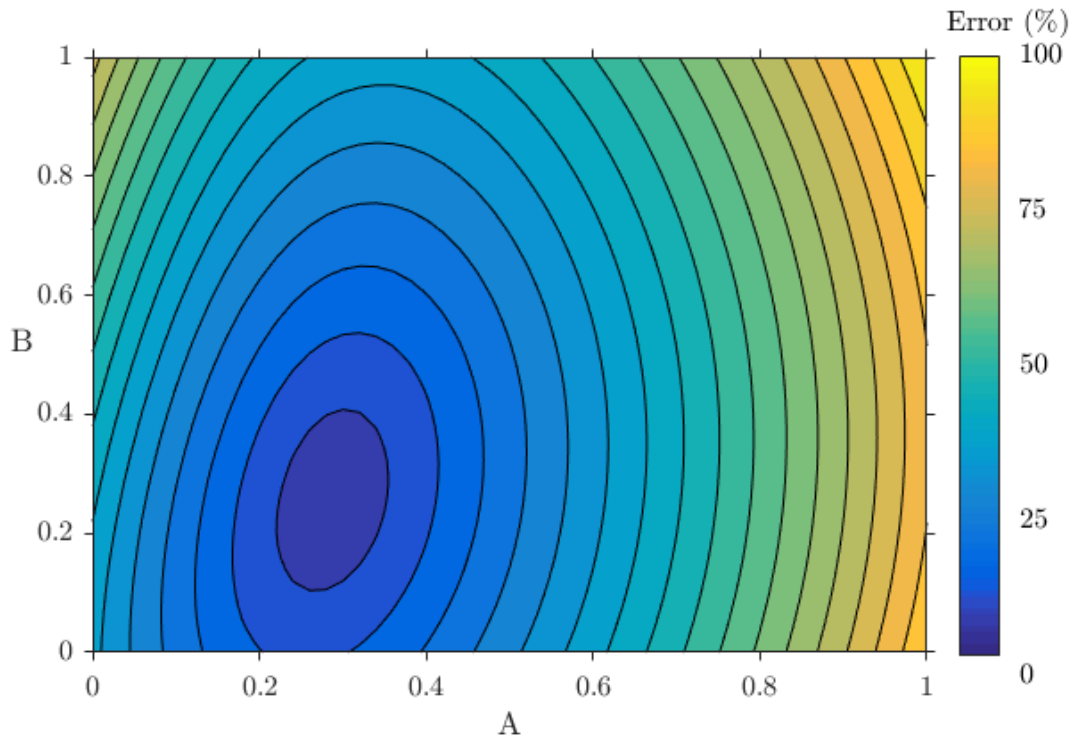


Figure 4.5 - Contour plot showing variation of RMSE of different data fitting, equation (4.11), resulting from varying A and B within 0-1.

The second pulse progressively intrudes into the first and they eventually merge. However, before reaching such merging points, the way in which the second pulse is advected differs between the short delay time flows and the long delay time flows. In multi-pulsed flows of short delay time, the first pulse quickly develops a density stratification because of ambient water entrainment (i.e., Britter & Simpson, 1978; Hallworth et al., 1996) prior to the second pulse release. The vertical density profile of the first pulse's body commonly exhibits a thick basal layer of relatively high density (Fig. 4.6A). The second pulse then intrudes into the first at a neutrally-buoyant level, vertically modulated by the velocity field within the first pulse (i.e., Ho et al., 2018a). Given that the maximum internal velocity of fluid within a turbidity current's body is always higher than the head velocity (Kneller et al., 1999; Sher & Woods, 2015; Hughes, 2016), the second pulse, once reaching the first pulse's body, will eventually be advected towards the flow front.

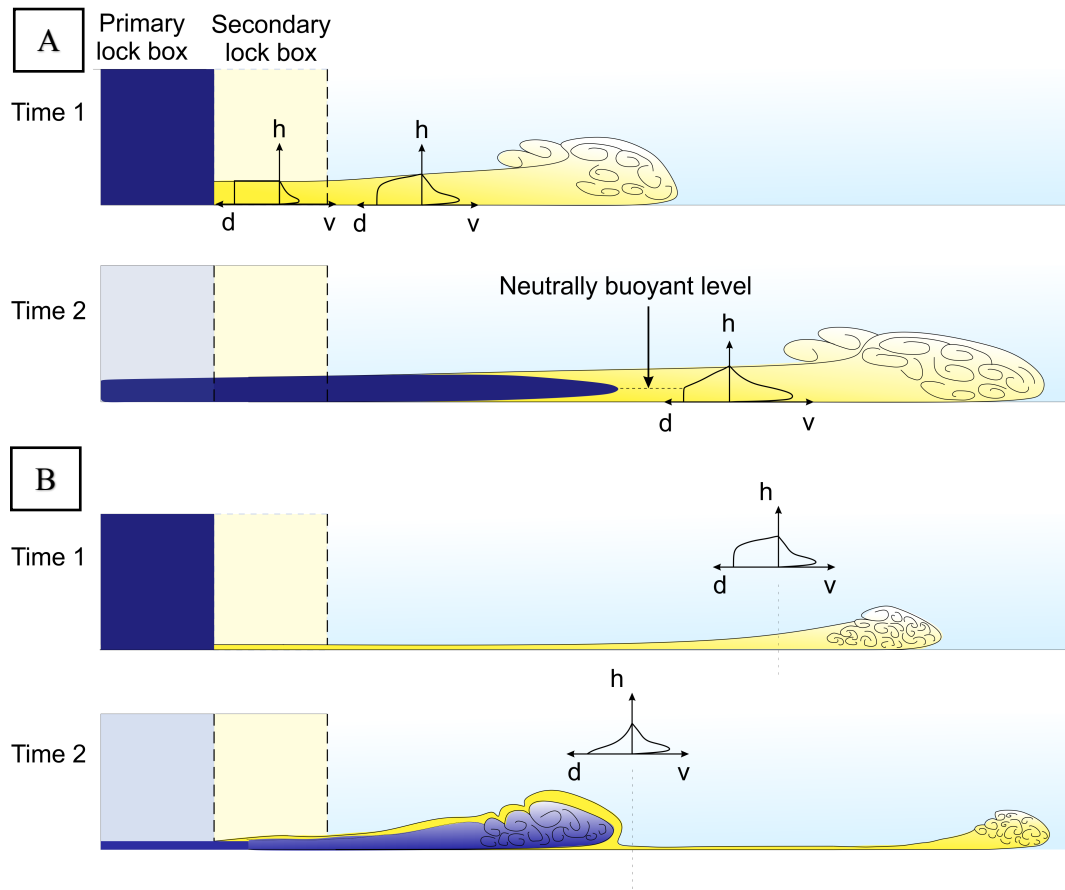


Figure 4.6 - Conceptual models of the intrusion of the second pulse in A) short delay time flows (modified from Ho et al., 2018a) and B) long delay time flows. Note: h , v and d denote flow height, velocity and density; in (B) i) the nose of the secondary pulse is lifted off the bed, ii) the dilute cloud remnant flow from the first pulse above the second pulse.

In multi-pulsed flows of long delay time, at the second gate time, the first pulse has already travelled a significant distance away from source (c. 11 lock lengths). The remnants of the primary flow near the lockbox consist of a very thin layer that has the density of the pre-release flow. Above this thin layer, there is a strongly stratified very dilute cloud, resulting principally from flow induced mixing with the ambient water at the head (although such stratification might also be attributed to turbulent mixing caused by lock gate removal, the speed of the lock gate release was set to minimize this effect). As the height of the dense layer is much smaller compared to that encountered in the short delay time flows, the second release of dense fluid will be located much closer to, or on, the bed. Here,

the second pulse front is much thicker than the thin layer remnants of the first pulse and is much denser than the background density of the cloud generated by the first flow, which has negligible effect on the flow. Therefore, the second pulse forms a bore travelling on top of the thin layer (of original flow density) of the first pulse. Thus, the remnants of the first pulse act as a lubricating layer reducing bottom boundary layer drag in the second pulse (see e.g., Ho et al., 2018a). By reducing drag the second pulse travels faster than the first such that it is eventually advected towards the front of the flow, where internal velocity gradients control pulse merging (Fig. 4.6B). However, this process will take comparatively longer than the intrusion process in shorter delay flows as the near lock gate velocity field of the first pulse is negligible and thus has little effect on the advection of the second pulse.

The variations in longitudinal velocity structure of multi-pulsed flows should be expressed in any associated turbidites such that the deposits exhibit a progressive spatial transition in grading pattern along the flow pathway from multi- to single-pulsed. Thus, multi-pulsed turbidites are expected to be deposited proximally and uni-pulsed deposits distally. The vertical separation between multiple intervals of coarse grain size within multi-pulsed turbidite units should progressively reduce as a consequence of reduced temporal separation between flow pulses with increasing time and space. Beyond the point of merging, uni-pulsed turbidites with a monotonic upward-fining grading pattern should be deposited. Thus, no inference regarding flow initiation mechanisms should be made based on the grading patterns of distal turbidites (Ho et al., 2018a).

4.4.2 Application of the scaling analysis

The scaling analysis presented in this chapter is ideally applicable for saline multi-pulsed flows since it was calibrated to experimental data of such flows. However, assuming that the dynamics of real-world submarine flows can be approximated by saline lock-exchange flows studied in the laboratory (Chapter 3), equations (4.9) or (4.11) can be used to predict the natural merging lengths of channelized 2D flows; furthermore, they may provide qualitative insight into merging in flows

that are free to expand laterally. For simplicity, using the reduced form, equation (4.11), the key parameters to predict merging lengths are: the flow height (h), initial breach length (L), reduced gravity of dense fluid (g') (or flow concentration, see Table 4.4 for relationship between the two parameters) and delay time (Δt). Initial axial breach length and delay time are two independent variables. Here variations and correlations of flow height and concentration are based on data from natural flow events (see Appendix A). The flow height and concentration data were collected from the literature (see Pharo & Carmack, 1979; Lambert & Giovanoli, 1988; Chikita, 1990; Chikita & Okumura, 1990; Johnson & Satake, 1994; Best et al., 2005; De Cesare et al., 2006; Gilbert et al., 2006; Mikada et al., 2006; Gutscher et al., 2006; Umeda et al., 2006; Vangriesheim et al., 2009; Xu, 2010; Xu et al., 2010; Liu et al., 2012; Cooper et al., 2013; Talling et al., 2013; Nelson et al., 2015); some concentrations were estimated using the frictional-gravitational force balance model of Parker et al. (1987) (see e.g., Abad et al., 2011)

$$(4.12) \quad S = \frac{C_f + e_w(1 + 0.5Fr^{-2})}{Fr^{-2}}$$

where S , C_f , e_w and Fr are channel slope, bed friction coefficient, dimensionless coefficient of entrainment and Froude number respectively. Friction coefficient C_f was determined as $1/Cz^2$ in which the Chezy resistance coefficient, Cz , equals 20 (e.g., Abad et al., 2011, Fig. 24).

Since flow height and concentration are interdependent (e.g., Abad et al., 2011), a conditional probabilistic distribution was derived from the empirical data. This enabled a correlation between flow height and concentration to be estimated (Fig. 4.7). Rearranging equation (4.11), we find that a dimensional merging length parameter takes the form

$$(4.13) \quad \frac{l_m}{\sqrt{L}} = 10^{0.7} [\sqrt{g'h} \Delta t h]^{0.25}$$

i.e., merging lengths scale with the square root of initial release length scale. Based on the quantified domains of flow height and concentration (e.g., flow

height and reduced gravity terms in equation (4.13)) shown in Fig. 4.7, the probability distribution and cumulative functions detailing the possibility of different values of $\frac{l_m}{\sqrt{L}}$, were determined using equation (4.13) at a fixed flow delay time (Fig. 4.8).

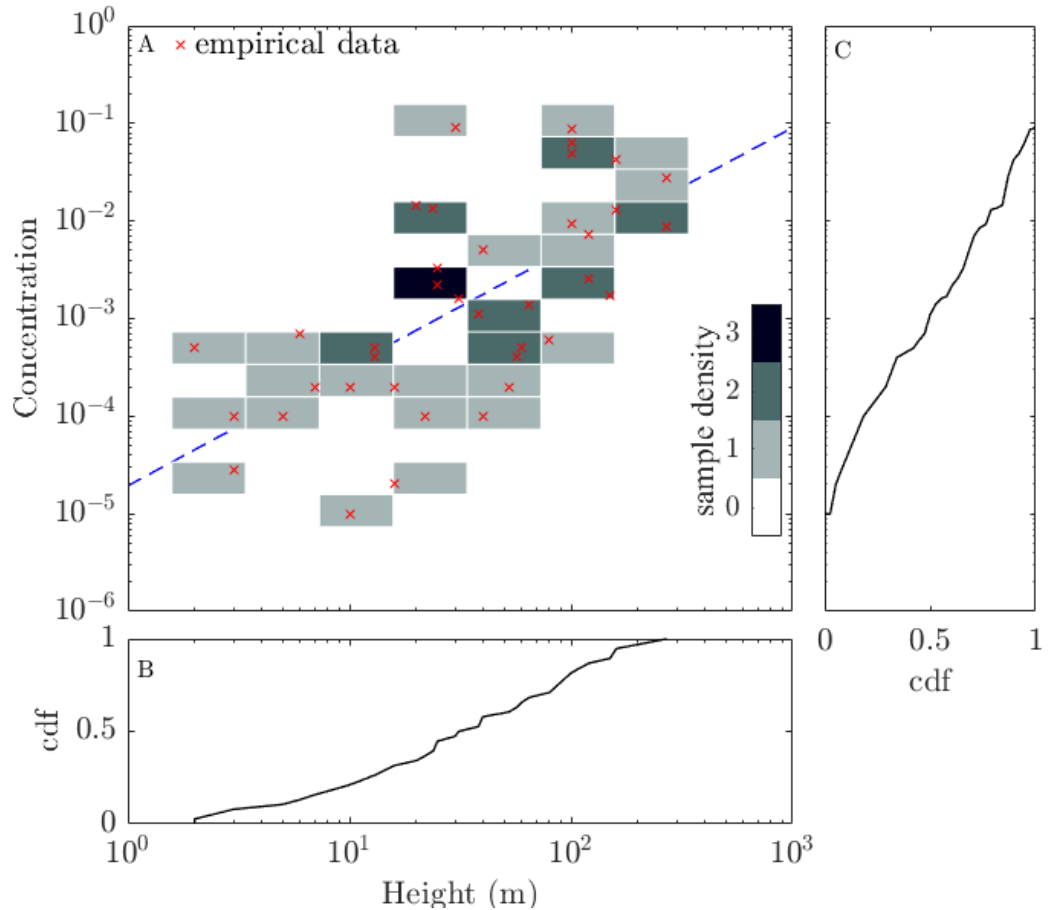


Figure 4.7 - Probability distribution plots of recorded natural flow height and concentration A) conditional density plot showing the density of co-occurrence of different flow heights and concentrations between the considered empirical data, B) cumulative density function of flow height and C) cumulative density function of concentration. Note: i) different colours indicate numbers of occurrence of a flow height at a given concentration, ii) red crosses indicate empirical values of flow height and concentration (data used in this plot are provided in Appendix A; e.g., Talling et al., 2013 and other cited references), iii) dashed line shows non-linear correlation between flow height and concentration, p-value ≈ 0 .

Table 4.4 - Calculated merging lengths for multiple canyon head scale failures

Parameters	Calculations
Initial flow height $h = 200\text{ m}$ $\rho_s = 2650\text{ kg/m}^3$ and $\rho_a = 1000\text{ kg/m}^3$ Flow concentration $c = 0.0315$ Delay time $\Delta t = 600\text{ s}$ Initial breach length $L = 3,000\text{ m}$	<ul style="list-style-type: none"> • Reduced gravity: $g' = g \left(\frac{\rho_s - \rho_a}{\rho_a} \right) c = 0.051\text{ m/s}^2$ • Normalized merging length: $\frac{l_m}{\sqrt{L}} = 10^{0.7} [\sqrt{g'h} \Delta t h]^{0.25} \sim 166.3\text{ m}^{1/2}$ • Merging length: $l_m = 9,108\text{ m}, L_m = 15,108\text{ m}$

An example calculation of merging length is laid out as follows. Assuming that initial flow height, concentration and delay time between two pulses of a seismically triggered bi-pulsed turbidity currents are 200 m, 0.0315 and 10 mins respectively (e.g., Heezen & Ewing, 1952; Piper et al., 1999; Nelson et al., 2015), equation (4.13) yields a value of normalized merging length as $\sim 166.3\text{ m}^{1/2}$ (Table 4.4). Approximately 59% of the sampled data have normalized merging lengths lower than $166.3\text{ m}^{1/2}$ (Fig. 4.8). By assuming that the associated axial breach length is 3,000 m, generated for example by a canyon head failure (e.g., Dengler et al., 1984), the total merging length is calculated as 15,108 m. Hence, within ~ 15 km from the point of initiation, multi-pulsed turbidites are expected to be deposited, and beyond, uni-pulsed turbidites, from which no inference of the flow initiation mechanism could be made.

The short predicted merging lengths calculated on the assumption that the canyon-head failure is typically associated with relatively short breach lengths contrast with the apparently common occurrence of multi-pulsed turbidites on active tectonic margins at much more distal locations from the continental shelves where the depositing turbidity currents were initiated. For example, Gutiérrez-Pastor et al. (2013) discussed the presence of multi-pulsed turbidites in the Cascadia region at locations ranging from 100 to 1000 km from channel heads. Therefore, the assumptions on initial flow conditions (i.e., flow height, concentration, breach length and delay time), or the differences between experimental and real-world flow initiation mechanisms (e.g., sequential

breaching (Goldfinger et al., 2012; Johnson et al., 2017) and confluence merging (Goldfinger et al., 2017)) used in the example calculation may not be plausible.

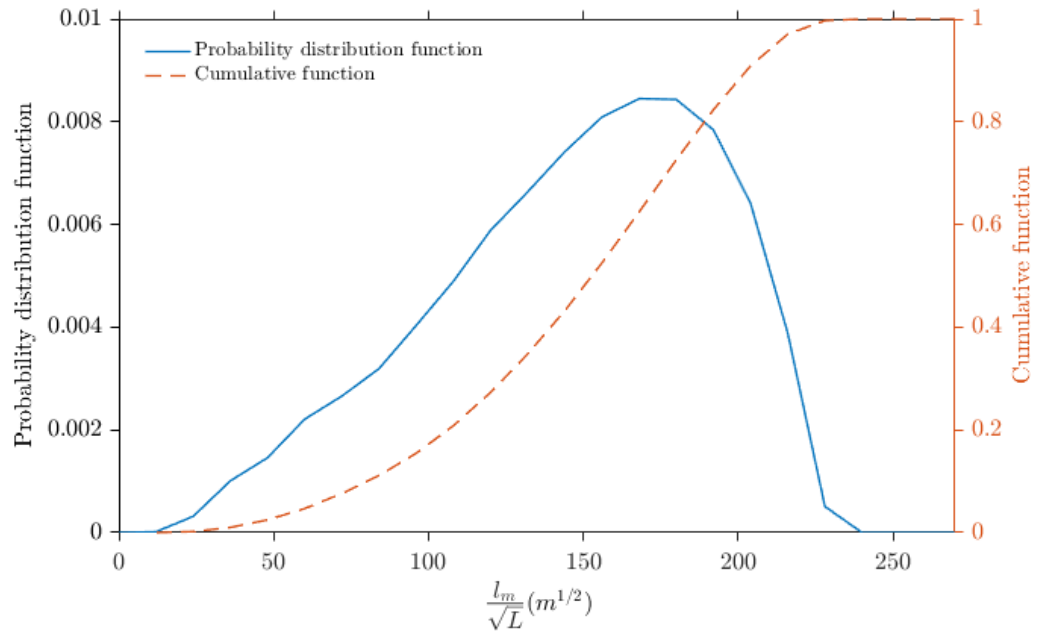


Figure 4.8 - Probability distribution and cumulative functions of normalized merging lengths $\frac{l_m}{\sqrt{L}}$ computed at delay time $\Delta t = 10$ mins.

To test the sensitivity of the predicted merging length to the values of initial flow conditions a parametric analysis was conducted in which all but one of the assumed parameters shown in Table 4.4 were retained, and the other parameter varied. The principal purpose of this sensitivity test is to assess the relative importance of initial parameters on merging length. From equation (4.13) merging length can be seen to scale with reduced gravity to the power of one-eighth, initial flow height to the power of three-eighths, or initial axial length to the power of one-half (Fig. 4.9). Therefore, initial axial length is the dominant control on the merging length. Varying the other three parameters within realistically broad domains does not change the merging length scale as significantly (Fig. 4.9B-D). However, in applying the scaling analysis to estimate real world mergingscales, all variables still need to be considered.

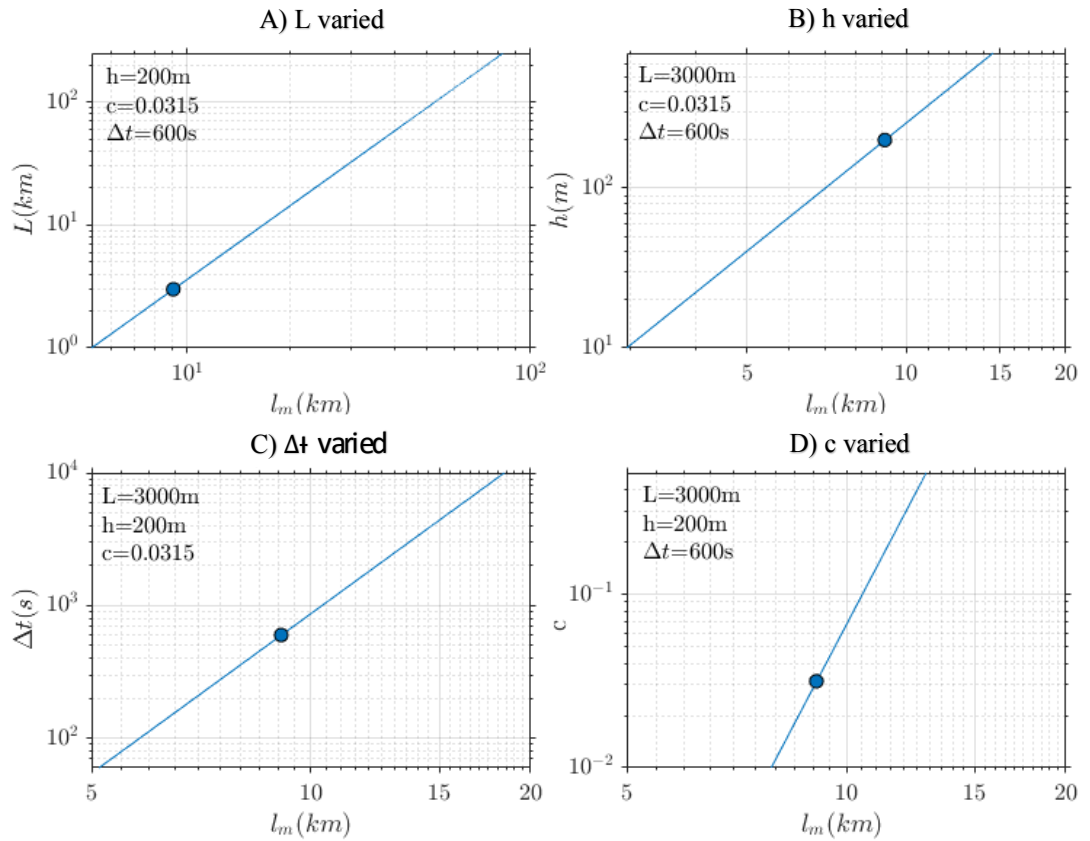


Figure 4.9 - Parametric analysis of merging length scales on the variations of lock length, flow height, delay time and concentration, equation (4.11), in which all but the selected parameter retained their values in Table 4.4, whilst the selected parameter were varied. Note: blue dots indicate the merging length cited in the example (see text and Table 4.4).

4.4.3 Initiation mechanisms of multi-pulsed turbidity currents

Multi-pulsed turbidity currents might be generated by i) retrogressive failures in which each slumping episode results in the formation of a pulse component or ii) combination at downstream confluences of multiple single-pulsed flows sourced from upstream tributaries. The delay time between individual flow components within a multi-pulsed flow is then controlled by i) the temporal separation between sequential slumping episodes, e.g., shock/aftershock events (between minutes to hours; e.g., Heezen & Ewing, 1952; Piper et al., 1999) or ii) the travel time differences between single-pulsed flows generated in upstream confluences upon reaching such points.

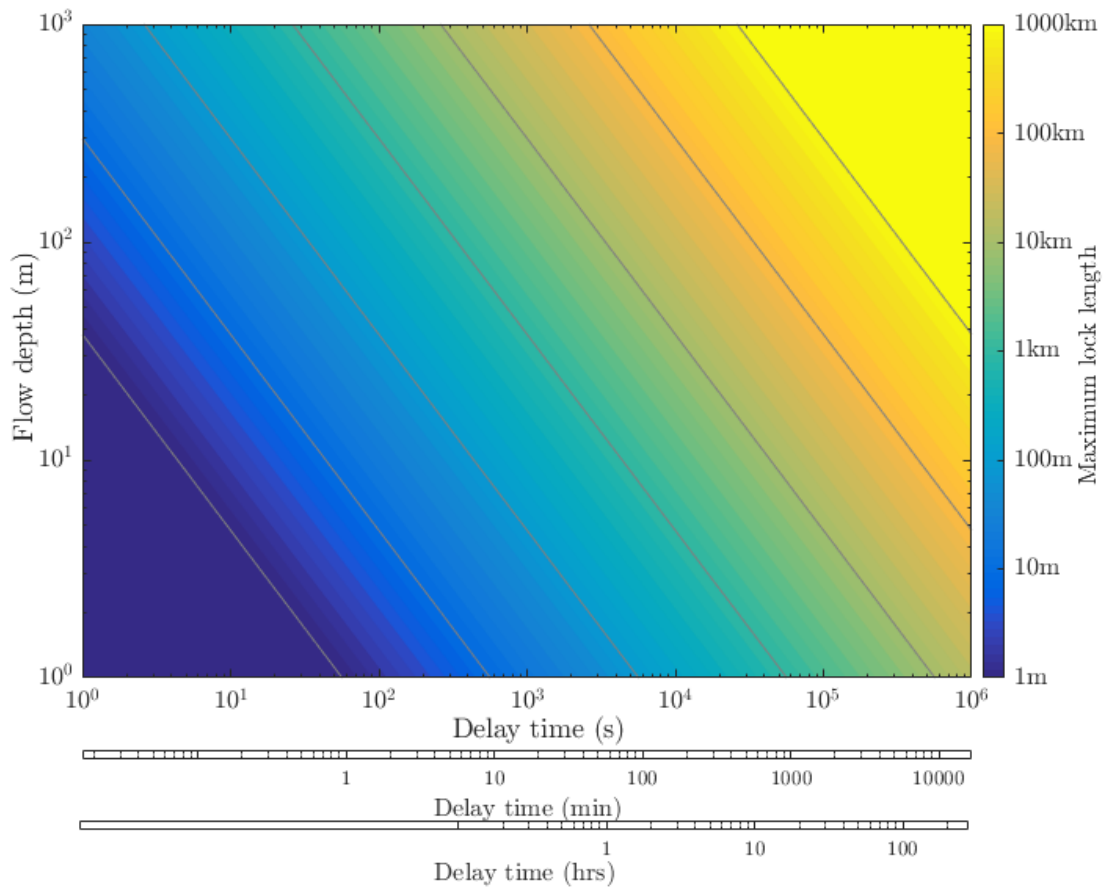


Figure 4.10 - Diagram showing maximum lengths of lock that can produce a multi-pulsed gravity current for different combinations of flow height and delay time between successive releases (see text for discussion).

Experiments conducted to support this scaling analysis were set up to model multi-pulsed flows generated by short, sequential and discrete ruptures. The fluid contained in the second lockbox in each experiment was released after the backwards-propagating wave of ambient fluid generated due to the collapse of the first release had reached the front of the second lock gate. In this way the second release was always initially higher than the current generated by the first release, and propagated as a pulse into it. When lock release delay times are sufficiently short that the backward propagating wave has not travelled a distance of at one lock length by the time of the second release, there is no difference in fluid levels across the lock gate at withdrawal. In this circumstance the dynamics of the combined flow are essentially the same as those following release of a single, combined lock, such that a uni-pulsed flow will be generated.

The propagation distance of the backwards-moving wave determines whether staggered dam-break releases will behave as uni- vs. multi-pulsed flows. The rearward-propagating wave of a dam-break collapse has a velocity $dX(t)/dt = -\sqrt{g'h}$ (Shin et al., 2004), dependent on the reduced gravity and thus concentration of the flow. A non-linear correlation between flow height and concentration is derived from empirical data (Fig. 4.7). The maximum wave travel distance (Fig. 4.10) that can produce a multi-pulsed flow thus specifies the lock length (at laboratory scales) or breach length (at prototype scales). Given the value of initially constant flow height, the wave travel distance at a particular delay time is $X = \sqrt{g'h}\Delta t$.

In natural systems, the delay time might correspond to the interval between successive sediment failures that produce a multi-pulsed turbidite, or to the duration of a single triggering seismic event that directly generates a multi-pulsed turbidite (in the latter case, this duration may extend up to 10 minutes duration e.g., Heezen & Ewing, 1952; Piper et al., 1999). Assuming a delay time of 10 minutes and a characteristic flow height of c. 200 m, the maximum length of each individual breach that might produce a bi-pulsed current is 7.5 km (i.e., a combined breach length of 15 km). The scaling analysis predicts that such short breaches should be associated with relatively short merging lengths (e.g., 15.1 km in the example cited). It follows that multi-pulsed turbidites produced by single seismic events should be of relatively restricted extent and that therefore, the model cannot account for the deposition of multi-pulsed turbidites observed at significant distances from continental shelves (see e.g., Gutiérrez-Pastor et al., 2013).

It is worth bearing in mind, however, that the scaling model proposed carries the assumptions that flows propagate on a zero-gradient channel and that they originally comprised two saline fluid components of identical volume. Natural multi-pulsed turbidity flows may initiate with flow components of different volume and will often propagate down sloping pathways. The same differences apply to considerations of flow merging and associated pulse development in

confluence settings, with the additional restriction that, on geometric grounds, the modelled height differences (i.e., a thicker intruding flow) may not be met, and that the mechanics of combination of separate flows may differ from the modelled scenario of juxtaposed axial releases. Such discrepancies between the simplified experimental model and natural setting warrant further exploration to assess whether the longer merging lengths documented in prototype settings (Goldfinger et al., 2017) might arise due to the effects of a more varied set of boundary conditions. These subjects will be discussed in Chapter 6.

4.5 CONCLUSIONS

Data from experiments conducted to model saline multi-pulsed gravity currents in which initial boundary conditions were systematically varied reconfirm that multiple pulse components within a multi-pulsed flow must merge at some point from source provided the flows remain active. This observation implies that turbidity currents in natural settings represent one mechanism by which multi-pulsed turbidites can be deposited. Such deposits can persist up to the point where pulses merge; beyond that point normally-graded turbidites should be deposited and no inference regarding flow initiation mechanisms is possible. An empirical scaling analysis (equations (4.9) and (4.11)) provides a tool to estimate the persistence of multi-pulsed turbidites in real-world environments, which suggests that initial axial breach is the key parameter that controls merging distances. Although the model can be used to predict merging distances in multi-pulsed turbidity currents generated due to retrogressive, discrete submarine failures of small scales (order of magnitude of less than 10 km), it cannot be directly applied to natural settings where initial breaches are extensive, on sloping flow pathways and where multi-pulsed flows are generated due to the combination of single-pulsed flows at downstream confluences. Multi-pulsed turbidites observed at long distances from continental shelves must have been deposited under the influence of a wider range of boundary conditions, including, but not restricted to, development of flow pulses of non-equal volume, flow propagation pathways of significant slope and the combination of flows at

confluences; the persistence of flow pulsing under such conditions is a topic that warrants further research.

Chapter 5

Dynamics of sediment-bearing gravity flow and geological implications

It has been established in Chapters 3 and 4 (see also Ho et al., 2018a and Ho et al., 2018b) that merging of pulses within a multi-pulsed dilute, saline gravity current is an inevitable phenomenon, such that velocity time series transition from being cyclically waxing-waning to rapidly-waxing then monotonically-waning along the flow pathway. A linkage between longitudinal variations in turbidity current flow dynamics and turbidite structure was inferred, with deposits proximal to source thought to be multi-pulsed (i.e., flow initiation signals are preserved) and those found distally, beyond the point where pulses merge, being single-pulsed (i.e., signals are lost or shredded). This pattern in deposition was thought to occur on the assumption that depositional waxing flows produced upward-coarsening deposits and waning flows the opposite. This chapter further explores the linkage proposed in Chapters 3 and 4 by evaluating experiments of dilute, single- and multi-pulsed sediment-bearing flows (turbidity currents) and their deposits. The experimental data confirm that the pulse merging phenomenon does occur in laboratory-scale turbidity currents. However, only a weak correspondence was seen between longitudinal variations in flow dynamics and the vertical structure of deposits. A conceptual model describing multi-pulsed flow deposition is presented, which builds upon the understanding developed in Chapters 3 and 4 by considering the settlement of sediments suspended in the flows. The possible influence of limitations in the experimental configuration are also considered.

5.1 INTRODUCTION

Experimental data describing the dynamics of multi-pulsed saline gravity currents, presented in Chapters 3 and 4, suggest that initial multi-pulsed velocity structures transform into standard waxing-waning profiles as flows run out. An implication was that any associated turbidites would likely exhibit multi-pulsed grading

profiles relatively proximally to the source, but that the deposits would become normally graded past the point where pulses within the flows merge completely. A second implication was that the spatial separation between multiple cycles of inverse-to-normal grading within a single turbidite would progressively reduce approaching this point, reflecting the progressive reduction in the temporal separation between multiple velocity pulses. These implications are based on the assumptions that a) normally graded turbidite intervals are deposited in the waning phase of flows and non-deposition or the deposition of upward-coarsening turbidite intervals is expected during the waxing phase, given that the duration of the waxing phase is much shorter than that of the waning phase (Kneller & Branney, 1995; Kneller & McCaffrey, 2003; Amy et al., 2005; Basilici et al., 2012), b) flows are depositional from the outset, with flow conditions being recorded in the deposit during progressive aggradation (Basilici et al., 2012; Goldfinger et al., 2013) and that c) a wide enough range of grain sizes is carried in suspension for a link between the flow shear stress and grain size to be expressed in the deposit. These assumptions are further discussed in section 5.4.2.2.

In Chapter 3, based on interpretations from multi-pulsed saline flow experiments, a range of different depositional patterns were proposed that varied longitudinally along a flow pathway. In Chapter 4, threshold timescales for the initiation of multi-pulsed flows were defined based on the times taken for the rearwards-propagating wave generated upon the collapse of the dense fluid in the first lockbox to reach the back of the lockbox. Such timescales vary as a function of initial flow conditions including initial depth and lock length of the dense fluid contained in the first lockbox. It was established in Chapter 4 that multi-pulsed flows in which the delay times between pulses are smaller than the threshold durations are effectively indistinguishable from single-pulsed flows.

However, questions regarding the variation of flow dynamics in sediment-bearing multi-pulsed flows and their expression in depositional structures along the channel pathways remain. Of particular interest are: i) if the merging phenomenon observed in the saline flow experiments (e.g., Chapters 3 and 4) can be reproduced for multi-pulsed turbidity currents; ii) if the hypothesis regarding

threshold timescales remains valid; iii) if any grading pattern within deposits can be discerned and iv) if linkages can be discerned between real-time suspension structures of sediments within the flows and depositional grading patterns. To address these questions, this chapter details experiments conducted to model sediment-bearing flows. The focus is on the difference in dynamics of single- and multi-pulsed turbidity currents linked to the vertical grading profiles of their deposits. Experimental data were collected using approaches including i) velocity profiling by collecting time-series of streamwise velocity data; ii) quantifying temporal variation in particle size distribution at a given height within the flows; and iii) collecting and analysing deposit samples at different positions along the flow pathway.

It will be shown that the pulse merging phenomenon does occur in laboratory scale turbidity currents. Also, multi-pulsed flows whose delay times were smaller than threshold durations (see Chapter 4) effectively behaved as single-pulsed flows. In addition, whereas the single-pulsed flows deposited uni-pulsed turbidites, the multi-pulsed flows showed weak development of multi-pulsed profiles relatively proximally to sources which became normally-graded (i.e., uni-pulsed) in distally. However, uni-pulsed characteristics were observed before the point of merging, and were therefore deposited by flows which retained multi-pulsed flow character (cf. the deposit structures predicted on the basis of the dynamics of multi-pulsed saline flows alone: Chapter 3). It is argued below that one cause of such deposition of single-pulsed turbidites prior to the points of merging may simply be due to progressive exhaustion of the supply of coarse-grained sediment during deposition. In addition, the possible role of limitations in the experimental set-up and methodology in the early loss of flow initiation signals are evaluated.

5.2 METHODOLOGY

5.2.1 Experimental set-up and parameters

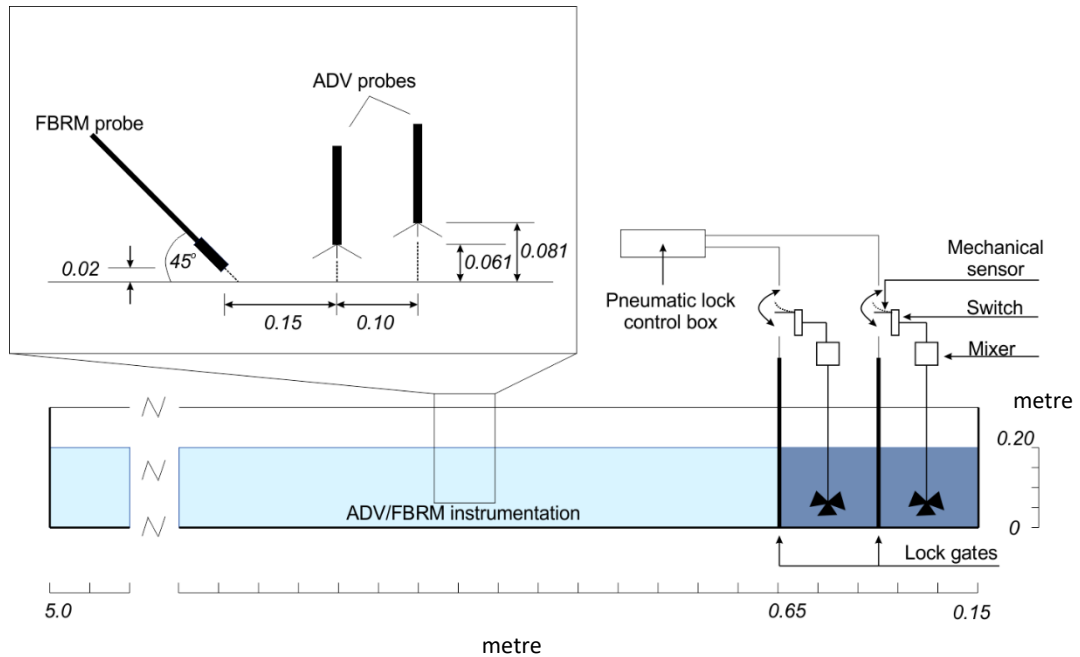


Figure 5.1 - Experimental set-up. Note: i) ADV/FBRM data were collected at $x=1.7$ m, 2.7 m and 3.7 m centred at midpoint of offset between the two probes, ii) sediments were sampled at $x=0.7$ m, 1.7 m, 2.7 m, 3.7 m and 4.7 m and iii) the back of the second lockgate (i.e., right end of the flume) starts at 0.15 m position so the absolute distances between sampling positions and source are $x - 0.15$ (m).

Experiments were conducted in a 5 m-long flume with two 25 cm-long lockboxes set up at one end (Fig. 5.1). This set up of the lockboxes enabled the generation of two pulses in series. Both single- and multi-pulsed flows entailed release of flow pulse components of the same volume. Using electronically timed pneumatic rams, the timing between the two lock gates was set at 0 s, 2.5 s and 8 s in order to model two flow types. It should be noted that by 2.5 s after the first lock gate was withdrawn, the returning wave generated by the collapse of the first dense fluid had not reached the back of the first lockbox such that the dynamical variations of 0 s and 2.5 s delay time flows were expected to be similar (section 5.3.1); see also Chapter 4 for discussion. These two flows were effectively single-pulsed flows, whereas an 8 s delay time enabled the generation of multi-pulsed

flow. Dense fluid used for the flows was made of a mixture of fresh water and 625 g suspended sediment consisting of both spherical ballotini and spheriglass in the ratio 4:1 by weight; sediment size ranged between 5 and 120 μm (Fig. 5.2). The density of sediments was 2500 kgm^{-3} (Potters, 2018). This combination of sediments gave the suspension an initial excess density of 3%, corresponding to a volumetric concentration of 4.5%.

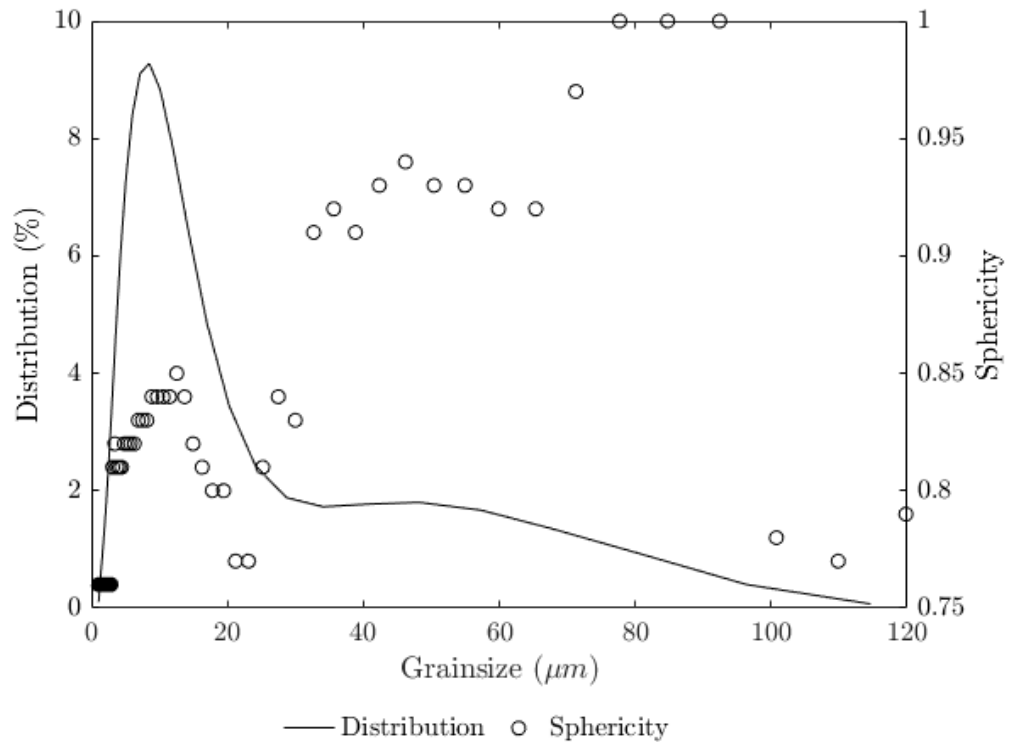


Figure 5.2 - Grain size distribution and grain shape data of sediments in the lockboxes used in the experiments (measured via laser diffraction granulometry method, using a Malvern 2000e grainsizer).

Sediments in the lockboxes were kept in suspension by using two MESE^R overhead stirrers that were set to run at 1000 rpm at the start of the experiments. Each mixer was fitted with a switch that automatically stopped it as the gate in front was lifted (Fig. 5.1). The height of saline fluid contained in the two lockboxes and of freshwater in the flume was 20 cm.

5.2.2 Experimental approach

Acoustic Doppler Velocimetry (ADV) was deployed to measure a time-series of the streamwise velocity field within the flows at positions 1.7 m, 2.7 m and 3.7 m along the flume (see Fig. 5.1). Velocity within the basal 4 cm of flow was measured using two ADV probes, mounted vertically on a rod and spaced at 10 cm horizontally. The upstream transducer was mounted 8.1 cm above the channel floor and recorded the velocity profile between 1.95 cm and 4 cm above the channel. The downstream transducer was mounted 6.1 cm above the channel floor and recorded the velocity profile between 0 cm and 2.05 cm above the channel (see Fig. 5.1). The overlap between the two instruments was 1 mm. The ambient fluid in front of the ADV probes was seeded with hollow spherical particles of 10 microns diameter to generate acoustic reflections.

In order to quantify the particle size distributions (PSD) within the experimental flows a Focus Beam Reflectance Measurement system (FBRM) was deployed. FBRM uses a rotating laser beam to measure the chord length distribution of all the particles present within the measurement window every two seconds within a defined time period (e.g., e.g., Wynn, 2003; Greaves et al., 2008; Agimelen et al., 2015). Assuming all the sediment particles are spherical, the chord length distributions can be inverted to give an estimate of the particle size distributions. The FBRM was deployed so that the centre of the measurement window was located 2 cm above the channel floor, the approximate height of the velocity maximum as noted in earlier experiments (Fig. 5.3A-C). FBRM data were acquired at 1.85 m, 2.85 m and 3.85 m along the flume (Fig. 5.1). The FBRM probe was set inclined at 45°, pointing upstream (see inset, Fig. 5.1), in order to effectively capture particles suspended within the flows upon their arrival. This configuration minimised the stagnation zone between the measurement window and the flow (set up recommended by the manufacturer, Mettler-Toledo, 2013). The cross section of the FBRM probe was small (3 cm diameter) such that deploying the equipment did not interfere with the evolution of the flows. In addition, no measurements were taken beyond the positions where the FBRM probe was set up.

The second flow component was dyed blue in order to enhance the visualisation of the flows. In order to confirm that pulses within the multi-pulsed flows merge eventually, the front positions of two pulses were tracked separately using two moving cameras which were set on a track in front of the flume (method after that described in Chapter 4).

Deposits were sampled and analysed for the 2.5 s and 8 s delay time flow experiments in order to compare their depositional structures. Since the dynamics of the 2.5 s delay time multi-pulsed flow were effectively the same as a single-pulsed flow with 0 s delay time, see result and discussion, its deposits are representative of a single-pulsed flow turbidites. Deposits were collected at positions 0.7 m, 1.7 m, 2.7 m, 3.7 m and 4.7 m downstream. Five pieces of 0.25 mm thick acetate sheet of dimensions 12 cm by 12 cm were glued on the bottom of the flume at the positions where deposits were to be sampled; sediment was deposited on top of these sheets. Once the sediments had completely settled (after two days), ambient water was slowly discharged from the flume by siphoning. Plastic rings of 10 cm diameter were placed onto the acetate in order to secure the deposits. The sediment samples were further allowed to fully dry at room temperature over two days. The sediment samples were then carefully removed from the flume. Each dry sample was impregnated with low-viscosity two-part adhesive under partial vacuum and mounted into transparent cubes of 3 cm diameter. The surface of the mounted samples was polished, and carbon coated to enable imaging using a Tescan VEGA3 Scanning Electron Microscope (SEM).

5.2.3 Data processing

5.2.3.1 Acoustic Doppler Velocimetry

Two sets of ADV data were collected in each experiment, measuring the velocity field of the upper and lower halves of the basal 4 cm flow height. These data sets were merged to visualise the velocity field within the whole flow. These streamwise velocity data were plotted as a series of contour maps which displayed spatio-temporal variations of velocity within the basal 4 cm of the flow for each

current. Depth-averaged velocity data of both data sets were also calculated (using equation (3.1), Chapter 3, in which h equals 2 cm). The lateral offset between the two ADV probes (see inset, Fig. 5.1) resulted in a stitching artefact in the data plots such that within the first two seconds of any sampling period only velocities within the top half of the basal 4 cm flow depth were captured. This is because the flows always arrived at the upper ADV probe first.

5.2.3.2 Focus Beam Reflectance Measurement

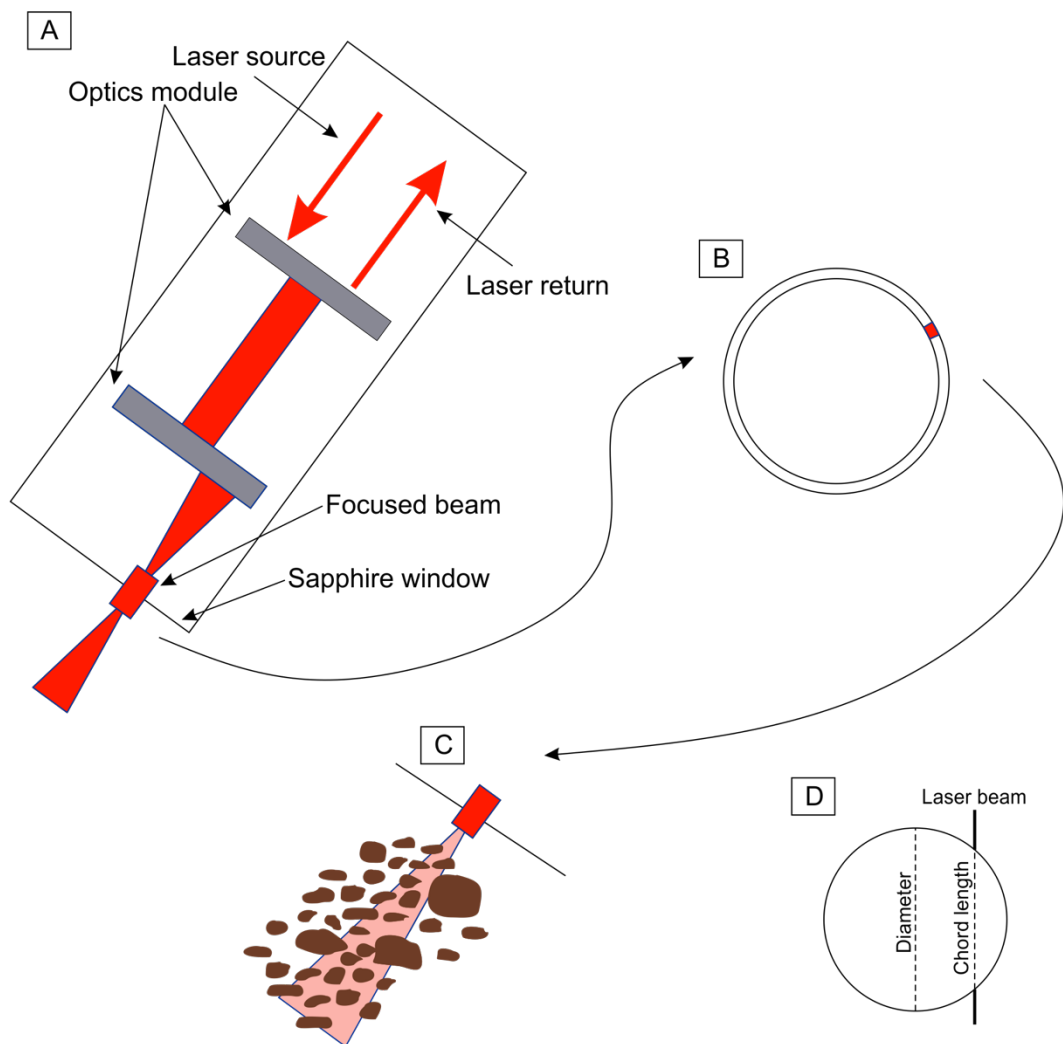


Figure 5.3 - FBRM technique A) schematic layout of internal structure of a FBRM probe, B) cross section of the measuring window, the focused beam travels along a circular path, C) measuring of chord length distribution of sediments entering the measurement vicinity and D) Chord length as a function of particle diameter, laser beam is exaggerated as being a straight

line upon travelling through the particle in the figure (modified after Wynn, 2003; Mettler-Toledo, 2013).

The distribution of sediments suspended within a flow at a given height is expressed as a CLD. A chord length is defined as the transect length of the laser beam across a particle's silhouette (Fig. 5.3D). Only sediments entering a scanning vicinity of depth T can be detected. The method used to correlate CLD and PSD is based on the principal assumption such that particles of a certain size entering the measuring window of the FBRM can cause chords of different lengths (see e.g., Wynn, 2003; Fig. 5.3). This method assumes that the largest chord length is equal to a particle's diameter.

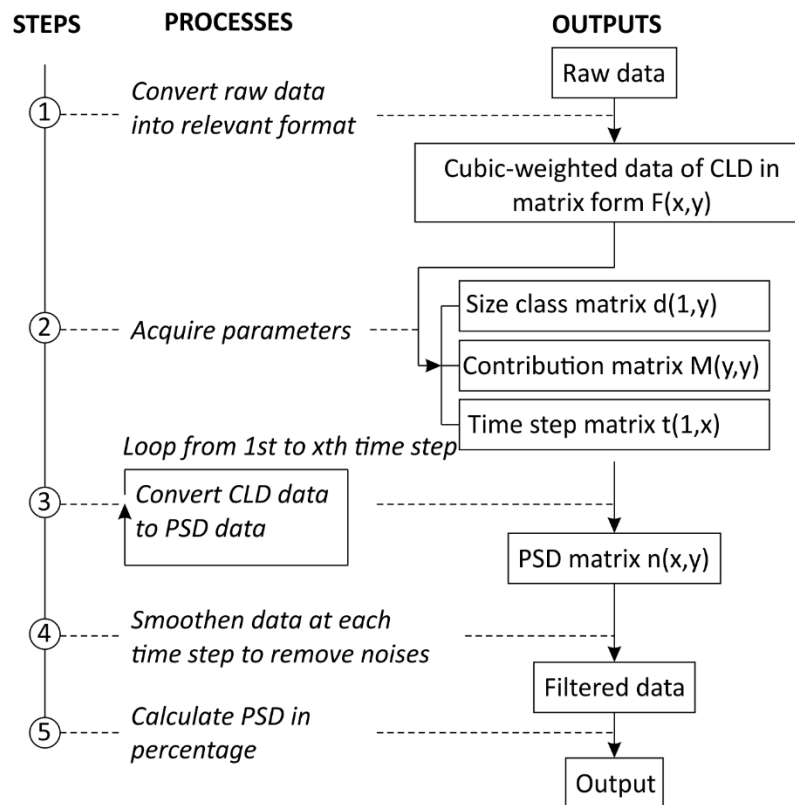


Figure 5.4 - Steps in the conversion between CLD and PSD data.

The CLD-PSD conversion adopted from Wynn (2003) was undertaken in MatLab™ 2016 (Fig. 5.4; using equation (5.1) below). CLD data were cubic-weighted to approximate the distribution of chords cut through a 3D object (i.e. particle), as opposed to the 2D surface area as observed by the FBRM probe (e.g., Wynn, 2003; Whelan et al., 2012; Fig. 5.3). In this approach, slight changes in the

variation in the distribution of coarse grain sizes are evident (e.g., Huang et al., 2009; Silva et al., 2013). In addition, since the particles used in the experiments were essentially spherical, their orientation in the flows did not need to be considered (sphericity was greater than 0.75; Fig. 5.2) and thus this method was applicable (Wynn, 2003). Given that chord lengths were subdivided into a series of intervals, the assumption made to support the inversion is that the distribution of chord lengths within each interval was constant, i.e. there is no further variation in CLD within any chord length interval. This enabled the distribution to be described by a finite number of discrete classes. Chord lengths and particle sizes of the sediments were divided into intervals, L_i where the ratio between the means of any two successive intervals was constant, $\frac{L_{i+1}}{L_i} = r$. The process by which CLD data were converted to PSD was summarised in Fig. 5.4.

In Fig. 5.4, x and y denote the numbers of time steps and chord length (or particle size) intervals respectively. The following equation was used to convert CLD to PSD (adopted from Wynn, 2003):

$$(5.1) \quad F = UTMn$$

in which M was the matrix form which expresses the contribution of size intervals to chord length intervals; F, n were CLD and PSD in matrix forms (i.e., counts at each chord length and size class); U, T were linear velocity of the laser beam and scanning depth. FBRM data were first exported in cubic-weight format (step 1, Fig. 5.4). Elements of M , calculated as part of step 2 (Fig. 5.4), took the form

If $j > i$

$$(5.2) \quad M_{ij} = \frac{1}{2} L_i^2 \left[\ln \left\{ \frac{r^{r^2-1} (1 + \sqrt{1 - a_{ij}})^{r^2+1}}{(1 + \sqrt{1 - a_{ij}/r^2})(1 + \sqrt{1 - a_{ij}r^2})r^2} \right\} + \frac{r^2}{a_{ij}} \left(\sqrt{1 - \frac{a_{ij}}{r^2}} - \sqrt{1 - a_{ij}} \right) - \frac{1}{a_{ij}} \left(\sqrt{1 - a_{ij}} - \sqrt{1 - a_{ij}r^2} \right) \right]$$

Given

$$a_{ij} = r^{-2(j-i)}$$

If $i = j$

$$(5.3) \quad M_{ii} = \frac{1}{2} L_i^2 \left[r\sqrt{r^2 - 1} - \ln (r + \sqrt{r^2 - 1}) \right]$$

These calculations were adopted from Wynn, 2003. Also, in step 2 (Fig. 5.4), matrices describing time steps and chord length/particle size intervals were computed.

From equation (5.1), PSD was calculated in step 3 (Fig. 5.4) as

$$(5.4) \quad n = \frac{M^{-1}F}{UT}$$

Best fit lines of PSD data, which were expressed in the form of numbers of particle counts at each size class, at all the time steps were then obtained by using a nonlinear least-squares solver, *lsqnonlin* in MatLab™ 2016 (step 4, Fig. 5.4; e.g., Mathworks, 2018a; Chapter 4 for similar description of the method of data fitting). They were then converted to percentage distributions (Fig. 5.4, step 5).

5.2.3.3 Sediment data processing

The samples of the deposits collected from the experiments were scanned using a Tescan VEGA3 Scanning Electron Microscope (SEM). In order to acquire data detailing vertical grading patterns of the samples, the output images taken using SEM were processed using MatLab™ 2016 (Fig. 5.5). The method used to process grain size data from SEM images (summarised in Fig. 5.5) was based on the Granulometry of Snowflakes example (Mathworks, 2018b; Thomas, personal communication 2017, Appendix B).

For each image, in step 1, the contrast of the image was enhanced using Adobe Lightroom; all other steps were carried out in MatLab™ 2016. The algorithm measured total intensity surface areas (i.e., total counts of pixel points) of particles in each size class. Thus, distributions of particles as a function of size were deduced. Length of scale bar in pixel and diameter of the largest particle in

the image were measured and inputted, as prompted during the process (step 2). A median filter then ran through the image to infill any holes found within particles (step 3). Such imperfections were an artefact inevitably resulting from polishing sediment samples. A threshold of colour intensity was set in order to separate particles and the background (step 4). In order to construct vertical grading profiles of the deposits, each SEM image was subdivided into several vertical slices with the grain size distribution analysed for each slice (step 5). The slices had the width of twice the largest diameter in the image, which was measured manually in step 2. Therefore, the numbers of slices depended on the greatest particle sizes and was different for each image. The overlap between two successive slices was 50% which accounted for the loss of any particles cut by the edges of the slices. The algorithm operated by collecting relevant pixel points associated with one size class in every associated step within the particle size loop (step 6, Fig. 5.5); it excluded particles of smaller sizes which had been previously accounted for in preceding openings. Mean grain size of the sediments captured in each slice and also vertical grading patterns of the whole sample were deduced. The script also summarised statistics of particle size distribution for each slice and for the whole image. In this chapter, vertical grading structures of the deposit samples were plotted at d16, d50 and d84 percentiles as an indication for fine, medium and coarse sediments deposited. In addition, half of the difference between d84 and d16 gave standard deviations for each sample (see e.g., Curran & Waters, 2014). This standard deviation plot was indicative of variation in grain sizes at different heights in the vertical grading structures.

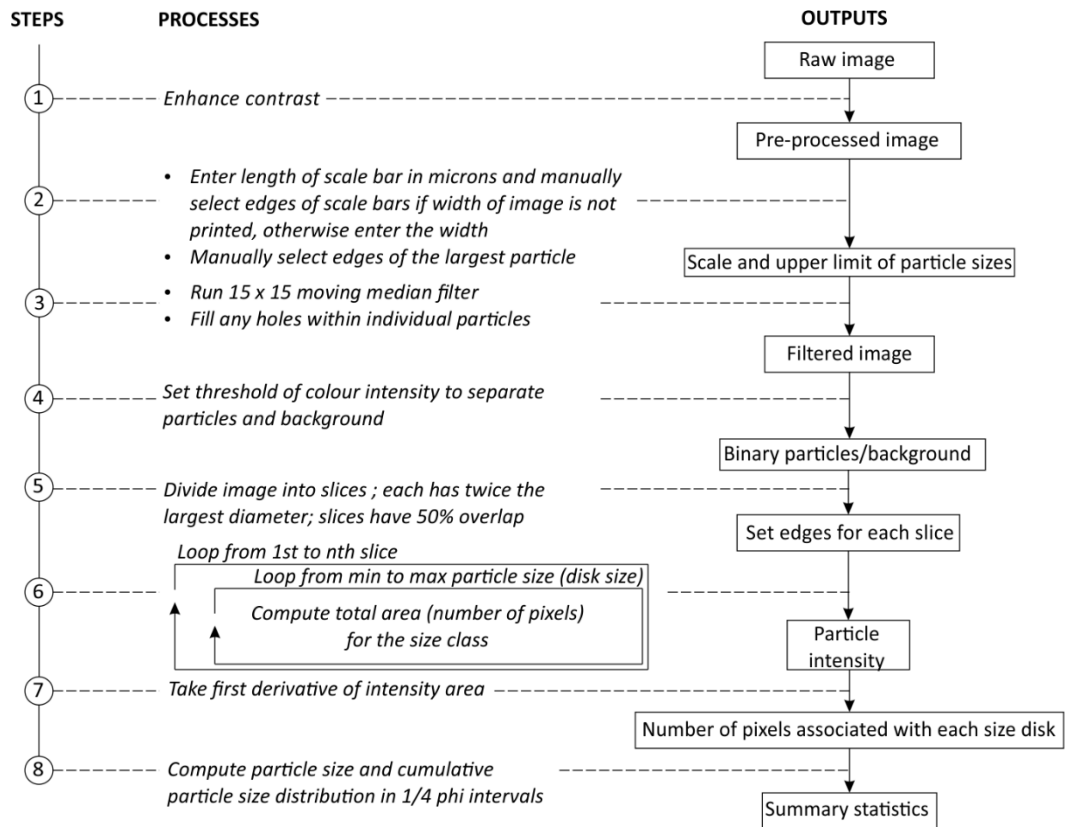


Figure 5.5 - Steps conducted to process SEM images to produce grain size grading data.

5.3 RESULTS

5.3.1 Visualisation

The single-pulsed (0 s and 2.5 s delay time; Figs. 5.6 and 5.7) and multi-pulsed (8s delay time; Fig. 5.8) flows evolved in similar manners to how single- and multi-pulsed saline flows behaved, described in Chapters 3 and 4. Therefore, in this section, such descriptions of flow visualisation will not be repeated. Hereafter, both 0 s and 2.5 s delay time flows are referred to as single-pulsed flow and 8 s delay time flow is referred to as multi-pulsed flow.

5.3.2 Velocity data

Single-pulsed flow (0 s delay time and 2.5 s delay time)

The velocity profiles of these flows exhibited a normal waxing-waning velocity structure as commonly observed in laboratory and field-based data (Figs.

5.9A-B & 5.10A-B; e.g., Chapters 3 and 4; Simpson, 1982; Kneller et al., 1999; Lowe et al., 2002; Sher & Woods, 2015). The velocity maximum was located within the bottom 2 cm of the flow height (Figs. 5.7A-B) with body velocities higher than that of the flow front. The flows decelerated downstream (Figs. 5.9A-B). The thicknesses of the heads were also seen to decrease with increasing time.

Multi-pulsed flow (8 s delay time)

Two distinct pulses were seen in the velocity structure of the flow, proximally to source (Figs. 5.9C and 5.10 C, $x=1.7$ m). The second pulse travelled at higher velocity than that of the first pulse (Figs. 5.9C, $x=1.7$ m). Further downstream, the first pulse decelerated while the second pulse maintained a relatively high velocity which enabled it to catch up with the first pulse (Figs. 5.9C and 5.10C, $x=2.7$ m). The separation between the two pulses was progressively reduced over time such that the pulses were eventually unified (Figs. 5.9C and 5.10C). Flow visualisation data captured during the experiments suggest that pulses within the 8 s delay time flow merged at 4.05 m from source (i.e., at the position $x = 4.20$ m shown on the gridline, Figs. 5.1 and 5.8). However, due to a constraint in space at the end of the flume, ADV data could not be collected beyond the 4.0 m point.

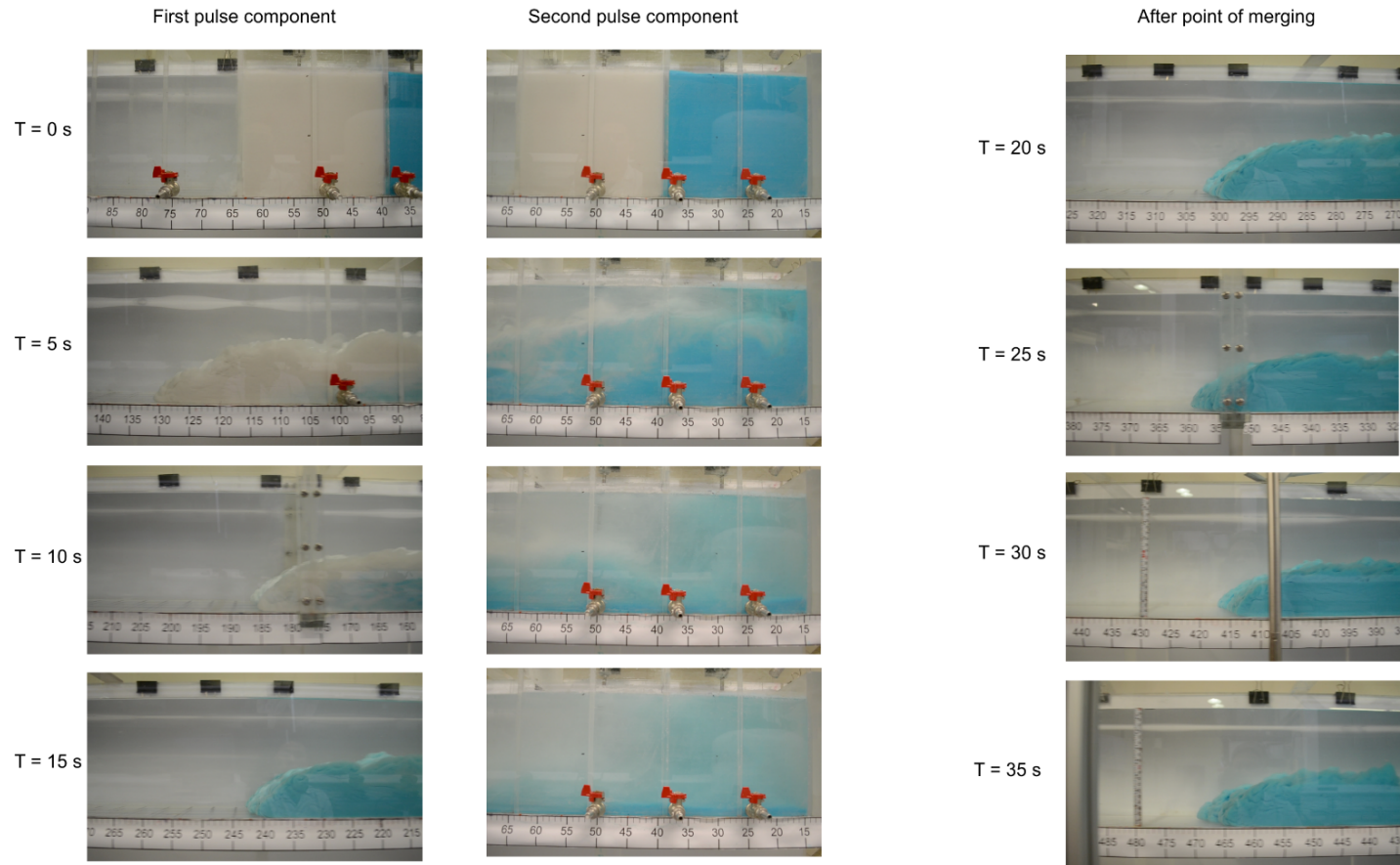


Figure 5.6 - The evolution of single-pulsed flow (0 s delay time).

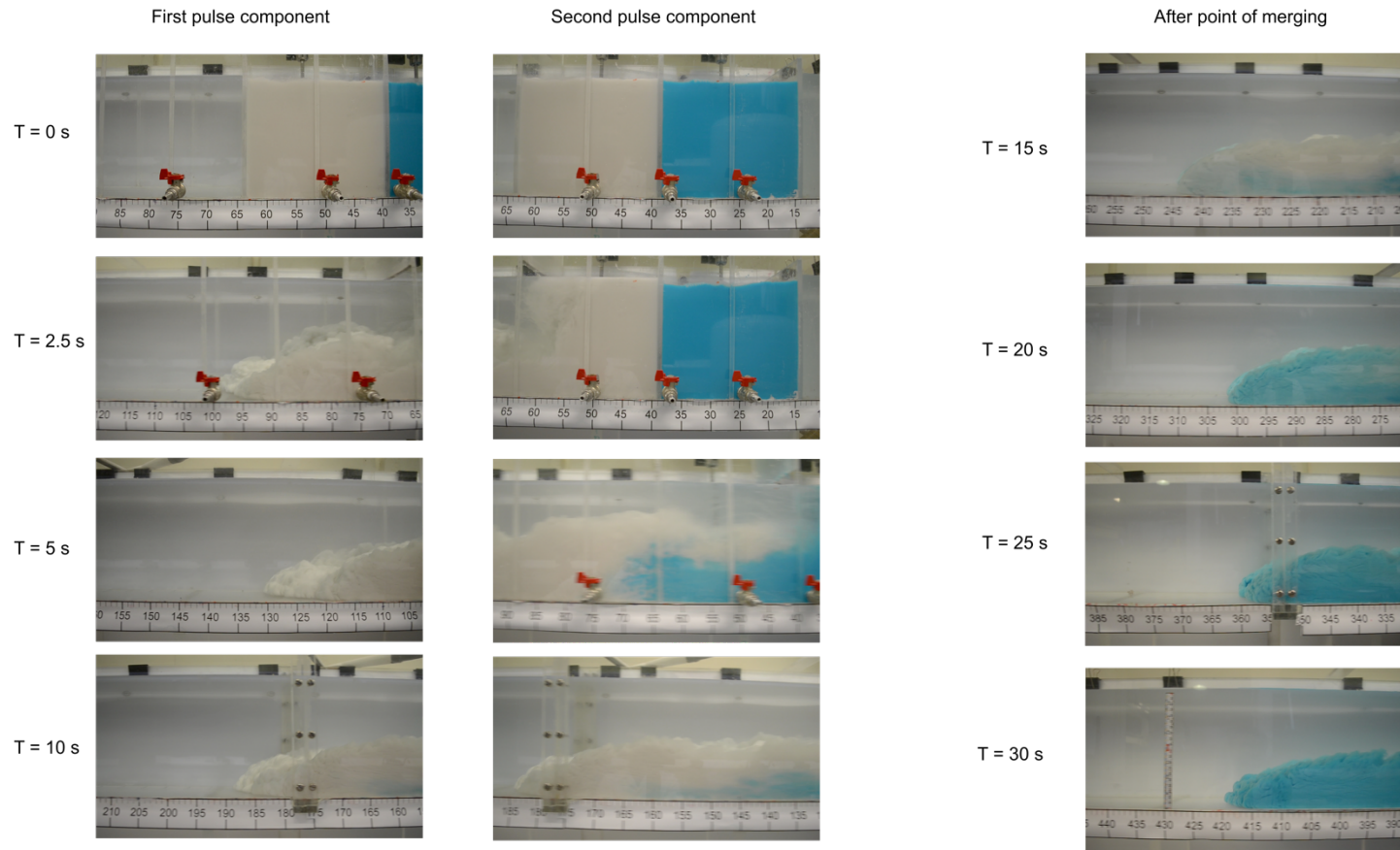


Figure 5.7 - The evolution of 2.5 s delay time flow.

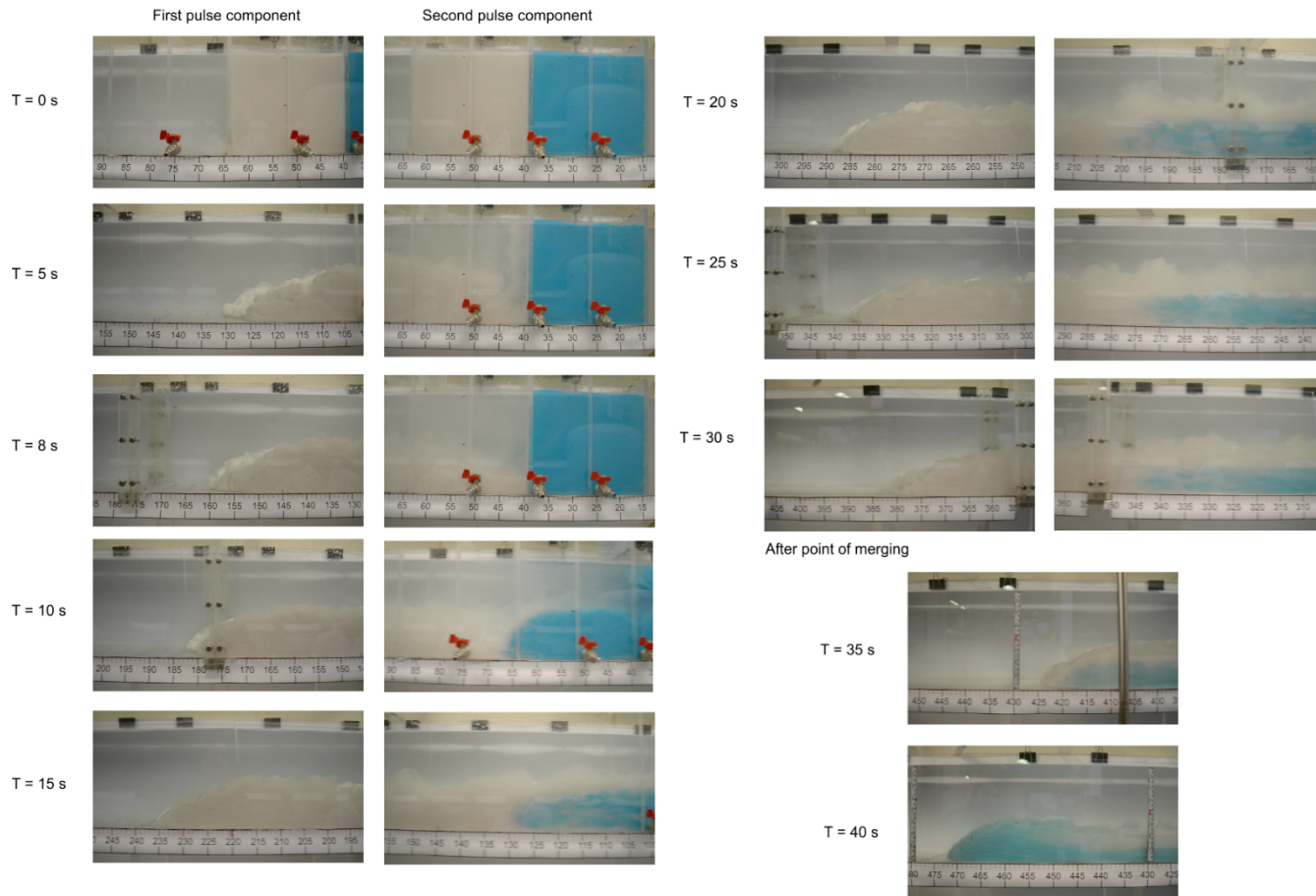


Figure 5.8 - The evolution of 8 s delay time flow.

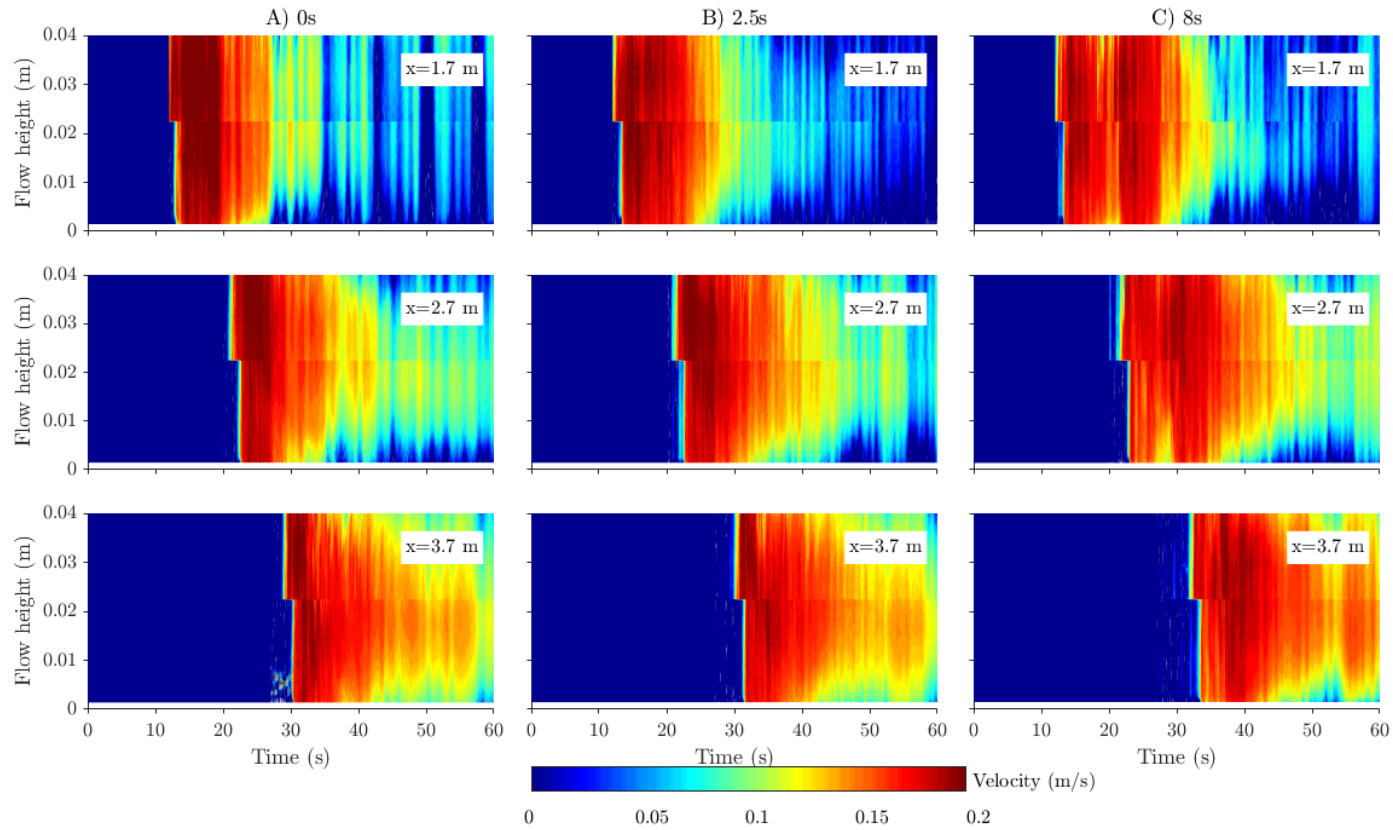


Figure 5.9 - ADV data showing variation in velocity field of A) single-pulsed flows, B) 2.5 s delay time flows and C) 8 s delay time flows. Note that the experimental set-up in which two laterally offset ADV probes were deployed results in a stitching artefact such that the flows arrived at the upper probe first, then at the lower one 2 s later.

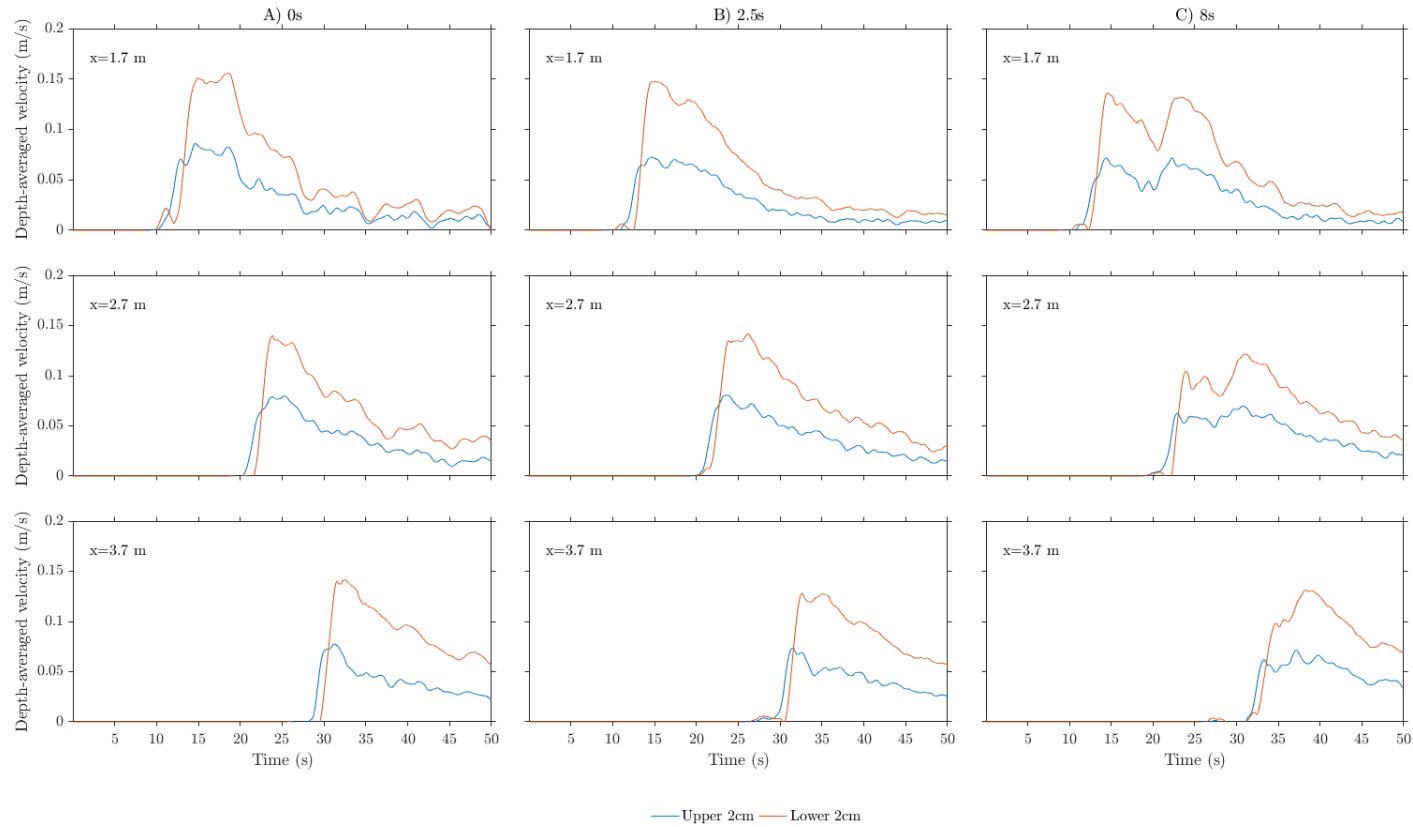


Figure 5.10 - Depth-averaged velocity of A) 0 s delay time flows, B) 2.5 s delay time flows and C) 8 s delay time flows. Note that effects of surface waves are indicated by the fluctuation of data, especially during waning phases. However, the magnitudes of the waves are relatively small compared to the flow velocity (see e.g., Chapter 3).

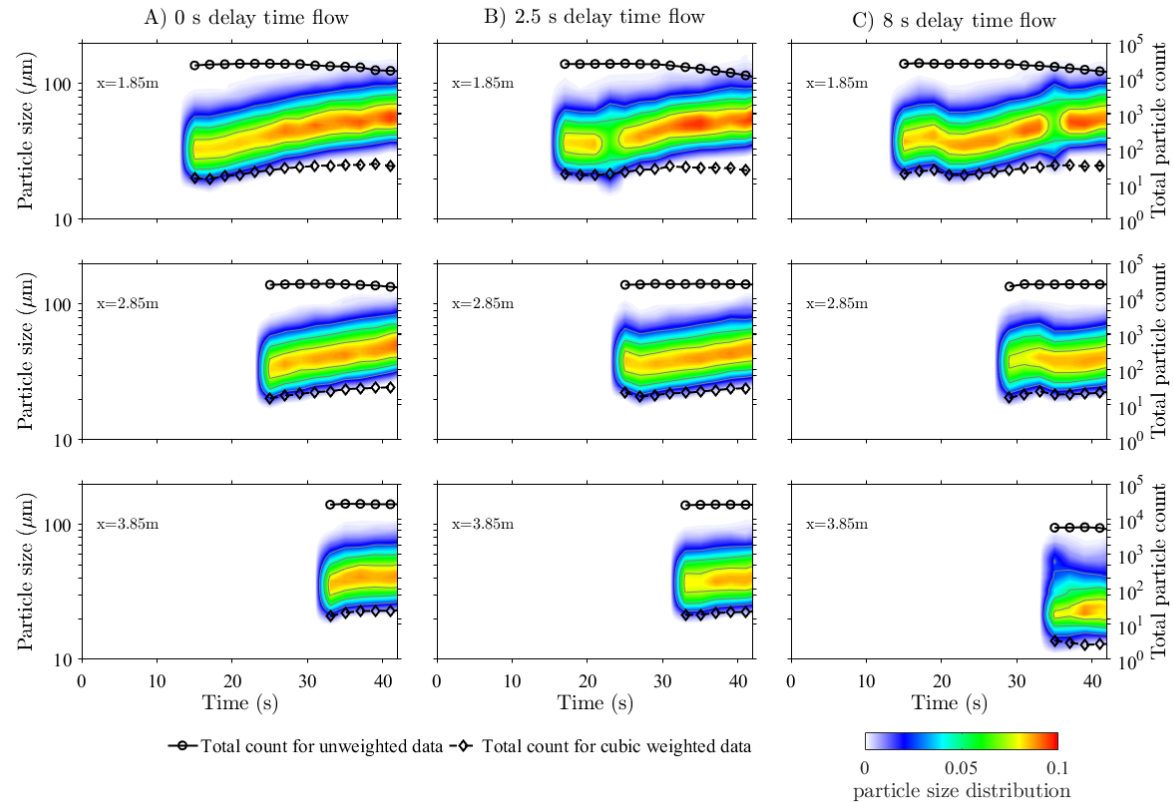


Figure 5.11 - Real time particle size distribution at 2 cm height of A) single-pulsed flows, B) 2.5 s delay time flows and C) 8 s delay time flows.

Note: the reduction in proportions of mean grainsize at 22-25 s, $x=1.85$ m for the 2.5 s delay time flow and that within 34-46 s, $x=1.85$ m for 8 s delay time flow are interpreted as a result of technical glitch.

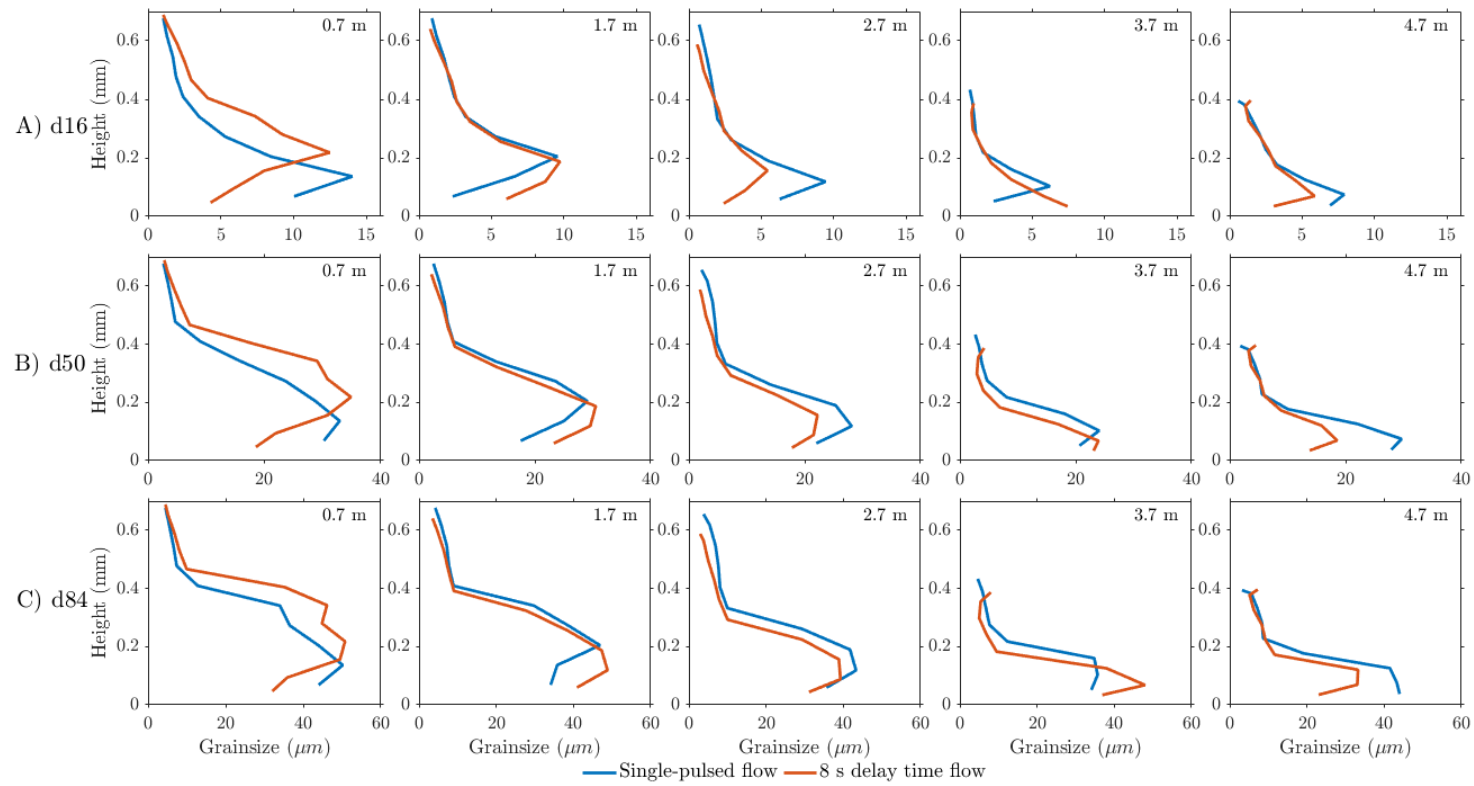


Figure 5.12 - Vertical grading profiles of deposits of single-pulsed (2.5 s delay time) and multi-pulsed (8 s delay time) flows collected at 0.7 m, 1.7 m, 2.7 m, 3.7 m and 4.7 m.

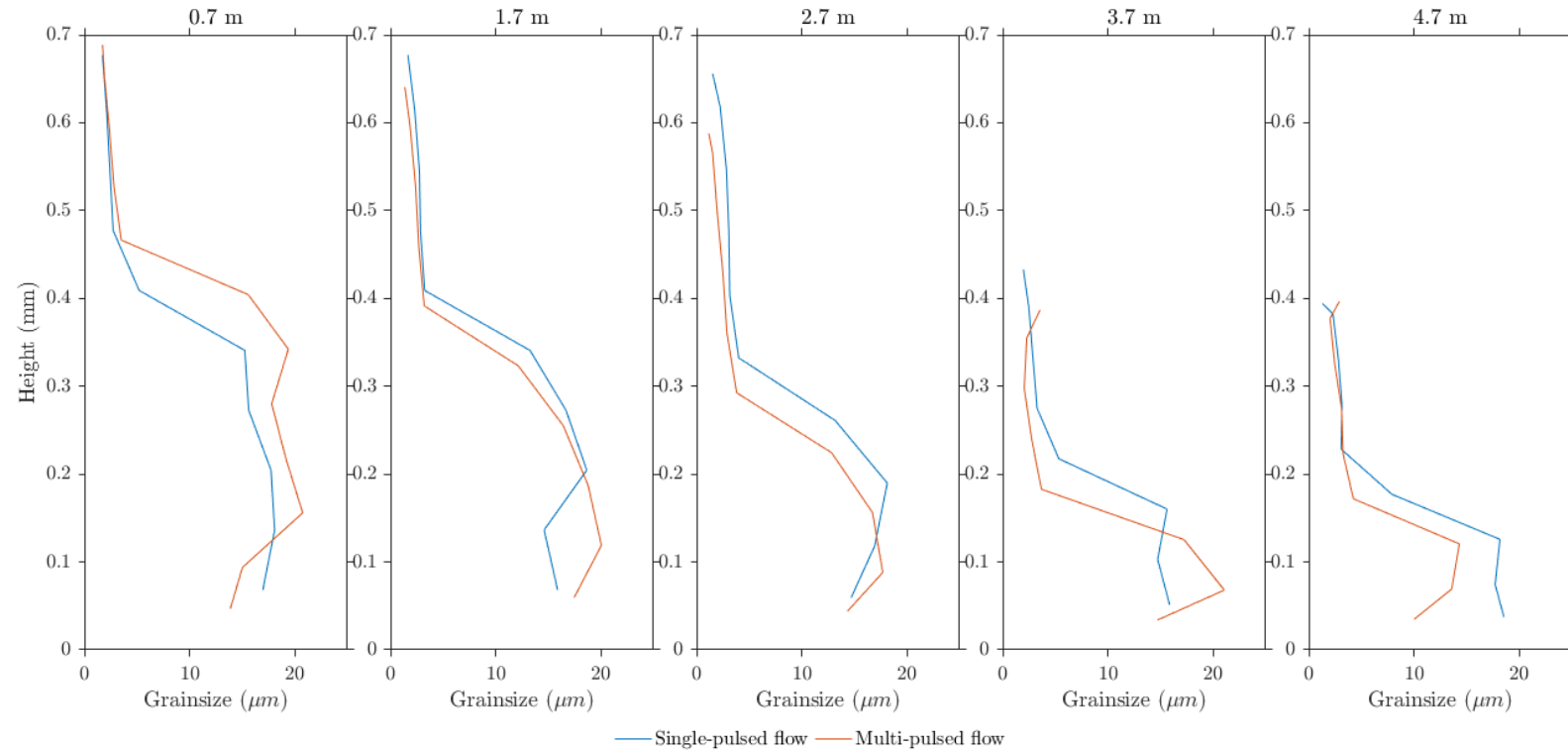


Figure 5.13 - Standard deviation of grain sizes.

5.3.3 Sediment suspension profiles

In this section, profiles of sediment suspension at 2 cm flow height are described for the single-pulsed (0 s and 2.5 s) and the multi-pulsed (8 s) flows respectively. The time-series patterns of sediment suspension at this characteristic height, measured at different downstream positions, are thought to be indicative of the temporal variations of sediment suspension at any given height within the flows. The PSD at each time step had the form of a binominal distribution, though the range of size classes varied in each data set (Fig. 5.11) as will be described below.

At proximal localities, the number of particles arriving at the sampling position appeared to decrease progressively as the heads passed by the probe (Figs. 5.8A-C, $x=1.85$ m). Particle counts were relatively stable within the bodies of the flows (Figs. 5.8A-C, $x=2.85$ m & $x=3.85$ m).

Single-pulsed flow

Mean grain size gradually increased as the flow head passed by the sampling position. Initially, sediments of 20-60 μm had been carried by the flow fronts over the first 5 s of the sampling period, prior to the arrival of the second pulse (Figs. 5.11A-B, $x=1.87$ m, 15-20 s). After the passage of the heads, mean grain size (i.e., sizes of sediment ranged within 30-90 μm) started to increase, which marked the arrival and passage of the flow bodies. At further distances, fine-grained sediments of 20-60 μm were always suspended in the flow fronts (Figs. 5.8A-B, $x=1.85$ m, 13-20 s; $x=2.85$ m, 25-30 s; $x=3.85$ m, 32-36 s) whereas coarser sediments of 30-90 μm were carried by the body and the tail (Figs. 5.8A-B, $x=1.85$ m, 40 s; $x=2.85$ m, 40 s).

Multi-pulsed flow

Sediments of 20-80 μm grain size were suspended in the flow within the first 5s after the flow hit the probe; grain size then increased as the flow head passed the sampling position (Fig. 5.11C, $x=1.85$ m, 15-20 s). The arrival of a second pulse was marked by a decrease in grain size (Fig. 5.11C, $x=1.85$ m, $t=18$ s). After the second pulse front had passed the probe, the grain size of sediment

started to increase (Fig. 5.11C, $x=1.85$ m, $t=21$ s). Similarly, at $x=2.85$ m, the grain size of the sediments suspended within the flow front increased as the first pulse arrived but decreased as a second pulse started to intrude into the first pulse (Fig. 5.11C, $x=2.85$ m, 33-40s). Further downstream, at the position where the two pulses were close to merging, the range of grain size remained relatively constant (Fig. 5.11C, $x=3.85$ m).

5.3.4 Sediment data

In this section, data describing depositional structures of single-pulsed (0 s and 2.5 s delay time) and multi-pulsed (8 s delay time) flows are presented in the order of i) generic trends observed for all the deposits and ii) different features in depositional profiles of each flow.

The experimental data showed that thicknesses of the deposits collected in the experiments decreased as the flows travelled further from the source (Fig. 5.12). This observation corroborates previous studies (e.g., Kneller & Branney, 1995; Mulder & Alexander, 2001; Shanmugam, 2002). For each experiment (i.e., each flow type), data detailing the vertical variations in grain size of fine, median and coarse sediment fractions (i.e., d_{16} , d_{50} and d_{84}) showed similar trends (Fig. 5.12, d_{16} , d_{50} and d_{84} for each flow type at five sampling positions). Sediments within the upper 30% of the depositional heights of all the deposits were always normally-graded and well sorted. The variations in grain size within these upper parts (Fig. 5.13) were insignificant compared to the variation of grain size within the bottom part of the deposits (i.e., step profile characterised by a dense base followed by an abrupt reduction in grain size Kneller & Buckee, 2000). Basal inverse-graded deposition was observed for the deposits of both flow types (Fig. 5.12) and was attributed to longitudinal grain size segregation e.g., Hand (1997), Baas et al., (2004).

Single-pulsed flow

All deposits collected in the single-pulsed flow experiment exhibited upward-fining grading profiles after the basal inversely-graded interval (Fig. 5.12A, data indicated by blue line; e.g., Kneller & McCaffrey, 2003; Amy et al., 2005;

Babonneau et al., 2010 for similar observations). The proximal deposit (at 0.7 m) was thicker than ones collected at further downstream distances by up to approximately 50%. This observation of thicker deposits near the lock gates is commonly seen in lock-exchange sediment-bearing flow experiments (Fig. 5.12A; Bonnecaze et al., 1993; Kneller & McCaffrey, 2000; Peakall et al., 2001).

Multi-pulsed flow

The thickness of the deposits of the flow sampled, proximally to source, at 0.7 m, 1.7 m and 2.7 m was greater than that of deposits taken at the other two downstream positions by 50%. At 1.7 m, the flow deposited proximal turbidites with a higher fraction of coarse sediments (Fig. 5.12C, 0.7 m). Vertical grading of the coarse fraction deposited by this flow showed two intervals of inverse-to-normal grading (Fig. 5.12C, 0.7 m, yellow line). It was noted that pulses in this experiment merged at 4.2 m down the flume, and further downstream from points of initiation the flow deposited sediments with upward-fining grading structures (Fig. 5.12C, 1.7 m – 4.7 m). However, this depositional profile was observed even prior to the merging of the two pulses (cf. the interpretation of multi-pulsed turbidite deposition presented in Chapter 3).

5.4 DISCUSSION

5.4.1 Criteria for the generation, and depositional structure of single-pulsed flows

In the 2.5 s delay time flow experiment, when the second lock gate was removed, the backwards-propagating wave generated due to the slumping of the first dense fluid component had not reached the second lock gate. Thus, the dynamics of the 0 s and 2.5 s flows were essentially the same as anticipated in this situation (see also section 5.3.2 for their velocity structures). The speed of the wave estimated using the visualisation data of the 2.5 s delay time flow is 0.06 m/s. This velocity is smaller than the 0.22 m/s value calculated using the model presented in Chapter 4 (see section 4.4.3). The difference in the two estimations might result from stratification developed within the first lockbox, as it can be anticipated that

sediments began to be deposited immediately upon turning off the mixers. Hence, density of the first flow pulse and thus the actual wave speed were reduced. Regardless, the 2.5 s delay time flow behaved similarly to a single-pulsed flow. Therefore, in order to enable the generation of multi-pulsed flows, the timing between the two lock gates (i.e., between two breaches in natural settings) needs to be constrained (see also Chapter 4). This subject is discussed in section 5.4.1.1.

As discussed in Chapter 4, the initiation of single-pulsed and multi-pulsed flows is distinguished by different temporal separations between the two pulses in the flows. Long temporal separation permits a transition in the variation of multi-pulsed flow velocity from cyclic waxing-waning to rapid waxing followed by monotonic waning. In this transition, the latter is the standard time-series of velocity variation commonly observed in the dynamics of single-pulsed gravity flows (Felix & Peakall, 2002; Kneller & McCaffrey, 2003). The timescales between pulses can range between a minimum threshold (as discussed in section 5.4.1.1) and minutes/hours, depending on the nature of the initiation mechanism. In prototype environments, delay in the generation of pulses arises due to separation between successive submarine slumping episodes due to pulsed earthquakes, shock/aftershock events or between the arrivals at confluences of different single-pulsed flows sourced from individual upstream attributes (e.g., Hsu et al., 2008; Goldfinger et al., 2012; Lupi & Miller, 2014; Beeson et al., 2017). Therefore, single-pulsed flows are thought to be generated either by a single-failure mechanism, or by two (or more) failures whose temporal separation is less than the threshold interval.

On the basis of the threshold criterion in the generation of single-pulsed flows, this section discusses the process by which body fluid within single-pulsed flows is advected towards the flow front (section 5.4.1.1) and the dynamics, and associated depositional structure of single-pulsed flows, with a comparison to other studies (section 5.4.1.2).

5.4.1.1 Advection of the body fluid towards the flow fronts in single-pulsed flows, with relevant timing thresholds between pulses

The advection process of fluid within the body of a gravity current towards the flow front is very common, as observed in earlier research on gravity currents (Lowe et al. 2012; Sher & Woods, 2016; Hughes, 2016). Distinguishing between single and multi-pulsed flows is therefore more complicated than just identifying advection of material from the tail to the front of the flow.

In single-pulsed flows initiated by multiple factors with temporal lag smaller than minimum threshold, the short delay time causes no difference in flow dynamics compared to a zero second delay time flow (Figs. 5.6-5.8, A-B). In order to enable the generation of multi-pulsed flows, the minimum distance that the backward-propagating wave needs to have travelled prior to the second lock gate release is at least one lock length (see e.g., Fig. 5.14; Chapter 4 for mathematical model of minimum timescale). The constraint on timescales, therefore, accounts for a constant hydraulic pressure across the bottom of the two lockboxes, i.e., the whole flow, see Fig. 5.14. Whereas, a greater pressure difference caused by the difference in levels of fluids in the two lockboxes, in multi-pulsed flow experiments, will enhance internal advection rate of body fluid towards the flow front (Chapter 3). In fact, once the second lock gate has been withdrawn, the whole flow evolves in a similar manner to that of a single-pulsed flow of comparative scale (i.e., which has the same density and a volume that doubles that of a single lockbox) when the release interval is less than the threshold. In the prototype environment, in order for a multi-pulsed flow to be formed by two retrogressive submarine failures, the extension of the primary breach can be specified by the distance over which the rearwards-generated wave associated to the primary slumping has travelled.

From the single-pulsed flow experiments, it can be seen that fluid within the body of a single-pulsed turbidity current is advected towards, and might eventually reach, the flow front (e.g., Lowe et al. 2012; Sher & Woods, 2016; Hughes, 2016; Figs. 5.6-5.7). This phenomenon is seen in the visualisation of 0 s and 2.5 s delay time flows (see section 5.3.1) as the second fluid component (dyed

blue) was eventually advected towards the flow head. Such fluid once reaching the flow head will be continuously recirculated backwards to form the dilute fluid layer on the upper part of the flow (Britter & Simpson, 1978; Hallworth et al., 1996).

The points at which the two flow components 'merge' in single-pulsed flows (i.e., either zero or non-zero delay time between pulses) should not be considered the same as merging points as observed in multi-pulsed flow experiments. This is because there is a monotonic variation of velocity along the flow in these cases (i.e., no distinct pulses).

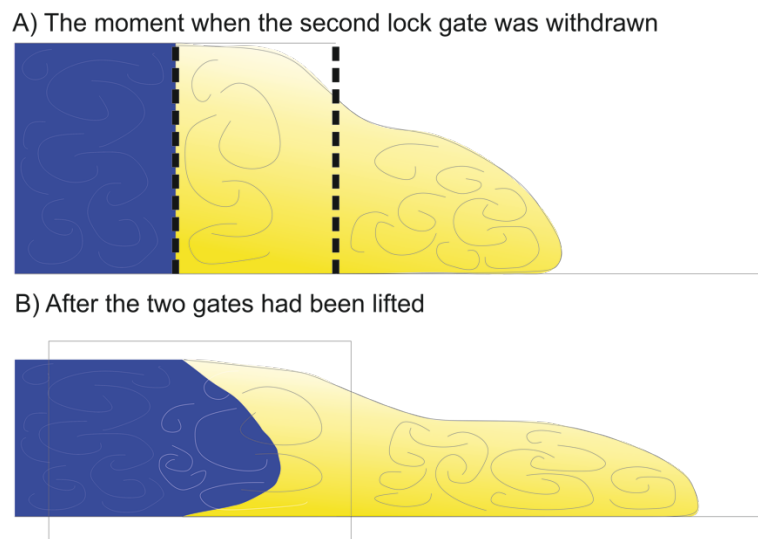


Figure 5.14 - Sketch of single-pulsed flow at an initial stage within which the dense fluids in each lockbox starts to collapse: A) when the second pulse component was released, B) at a time after the delay time. Note: dashed lines indicate that the lock gates have already been withdrawn, in this particular setting the delay time is non-zero but smaller than the relevant threshold (see text for discussion of this upper limit), rectangle highlights the mixing of fluid portions from each pulse components which make up the single-pulsed flows body.

5.4.1.2 Single-pulsed flow deposits

The deposits are much thicker in proximity close to the sources compared to those found further downstream, as a result of sudden collapse of sediments from the lock box (e.g., Fig. 5.12, deposits at 0.7-2.7 m were 50% thicker than those at 3.7-

4.7 m; Kneller & McCaffrey, 2000; Mulder & Alexander, 2001; Peakall et al., 2001). In addition, a high proportion of coarse-grained sediments can be deposited within proximal localities as commonly seen in the longitudinal variations of turbidite grading profiles (e.g., Fig. 5.12; Middleton, 1993; Kneller & McCaffrey, 2003). Deposits might be much thicker within the lockbox in comparison to those deposited on the flow pathway (e.g., Gladstone et al., 1998). However, such data of depositional profiles within the lockboxes were not collected in the experiments that were conducted to support the analysis of this chapter. In general, as suggested by the experimental data (Fig. 5.12), single-pulsed flows deposit sediments with the expected upward-fining grainsize profile (deposits of single-pulsed flows; e.g., Bouma, 1962; Lowe, 1982).

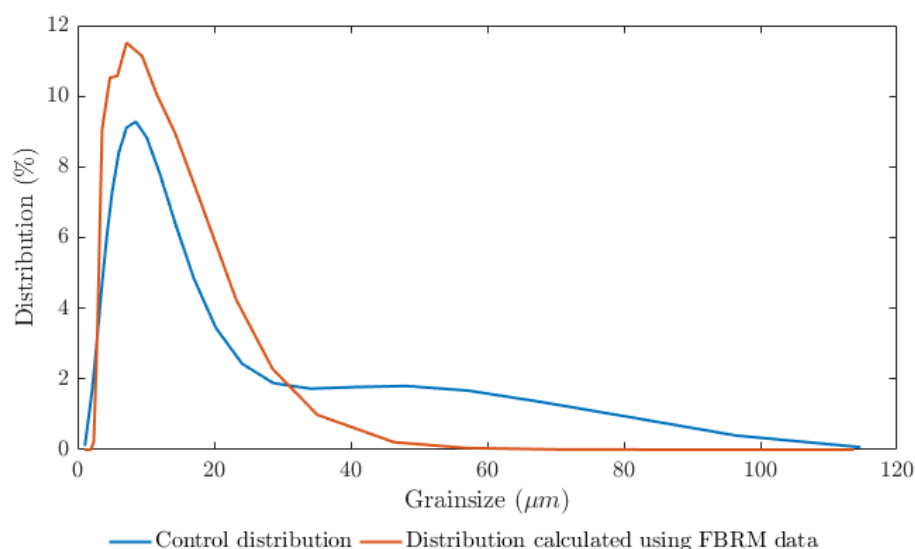


Figure 5.15 - Comparison between two data sets of grain size distribution analysed using the same control mixture of sediments; such control mixture is representative of the composition of sediments used in the lockboxes. Note: i) analysis using laser diffraction granulometry method, blue curve (by deploying Malvern 2000e), ii) analysis using FBRM measurement and inversion, red curve and iii) this plot indicates that the reliability of the inversion algorithm is acceptable.

Inverse grading in the basal part of the deposits are also possible (e.g., Fig. 5.12). Such depositional features might be accounted for by the lagged arrivals at

the heads, and thus deposition, of sediments with different grain size (e.g., Kneller & Branney, 1995; Hand, 1997). Data describing sediment suspension within single-pulsed flows (Figs. 5.11A-B) suggest that relatively finer sediments (20-60 μm) are carried by the flow fronts, whereas those of coarser grainsize (30-90 μm) are suspended within the bodies. Such coarse-grained sediments and those coarser than 90 μm are less mobile and probably suspended within lower regions within the flows and thus might or might not arrive at the head prior to the deposition of the fine-grained sediments, depending on the shear velocity of the flows (e.g., Hand, 1997). However, the FBRM data in this chapter represent an at-a-point measurement at 2 cm flow depth and thus cannot present whole vertical profiles of sediment suspension within the flows at the points of instrumentation. Therefore, any assumption and analysis made using FBRM data await verification. Coarse sediments might also be incorporated on a low level within the flows head due to density stratification commonly developed within turbidity currents (e.g., Chapter 3; Fig. 5.15). In the experiments, such level was likely lower than that where the FBRM scanning window was positioned (i.e., at a height of 2 cm). In this sense, although the method of CLD-PSD inversion is reliable, the proportion of coarse sediments observed using FBRM is relatively low (Fig. 5.15).

5.4.2 Multi-pulsed flows

The velocity structure of multi-pulsed flows vary such that proximally to the source they exhibit cyclically waxing-waning structures. Such complex velocity profiles are progressively distorted downstream and eventually become monotonically-varying. Given that waxing flows suggest the deposition of upward-coarsening sediments and waning flows suggest the opposite (Kneller & Branney, 1995; Kneller & McCaffrey, 2003; Mulder et al., 2003; Amy et al., 2005; Chapters 3 and 4), the deposition of multi-pulsed turbidites could be expected to be persistent up to the point of merging. Also, beyond the merging point, normally-graded turbidites are expected. This hypothesis is set out in Chapters 3 and 4, based on the interpretation of saline flow data. However, experimental data collected from the sediment-bearing multi-pulsed flow do not fully support the outlined hypothesis, such that normal grading patterns might be seen before the

merging point (see section 5.3.4, above). Therefore, there is an unclear correspondence between the longitudinal variation of flow velocity structure and that of the deposits.

Nevertheless, commonly-observed characteristics of the deposits as seen in both this study and previous research include reduction in depositional thickness as flows evolve further downstream, thicker layers of coarse-grained sediments and inversely-graded sediments at the base. In fact, only the deposit found relatively proximally to source shows subtle evidence of multi-pulsing (Fig. 5.12, $x=0.7$ m); more distal turbidites are uni-pulsed even prior to the point of merging (Fig. 5.12, $x=1.7-3.7$ m). Below, a conceptual model is presented that describes the depositional process developed, based on the interpretation of the experimental data (section 5.4.2.1). Such early damping, or non-preservation, of multi-pulsed flow initiation signals prior to point of merging is discussed in section 5.4.2.1, based upon difference in settling velocities of sediments of various grain sizes. In addition, the possible impact of limitations in the experimental set-up are also discussed in order to account for the absence of multi-pulsed turbidite deposition prior to the point of merging (section 5.4.2.2; cf. the interpretation presented in Chapters 3 and 4).

5.4.2.1 Conceptual model of multi-pulsed flow dynamics and deposition

The description of the conceptual model presented in this section is based on the principal assumption that sediments aggrade progressively from overpassing flows (e.g., Choux & Druitt, 2002; Kneller & McCaffrey, 2003; Amy et al., 2005). A further assumption is that the composition and range of grain sizes of sediments comprising the pulses in a multi-pulsed flow can permit the deposition of multi-pulsed turbidites. However, the scenario in which this second condition might not be met will be discussed at the end of this section.

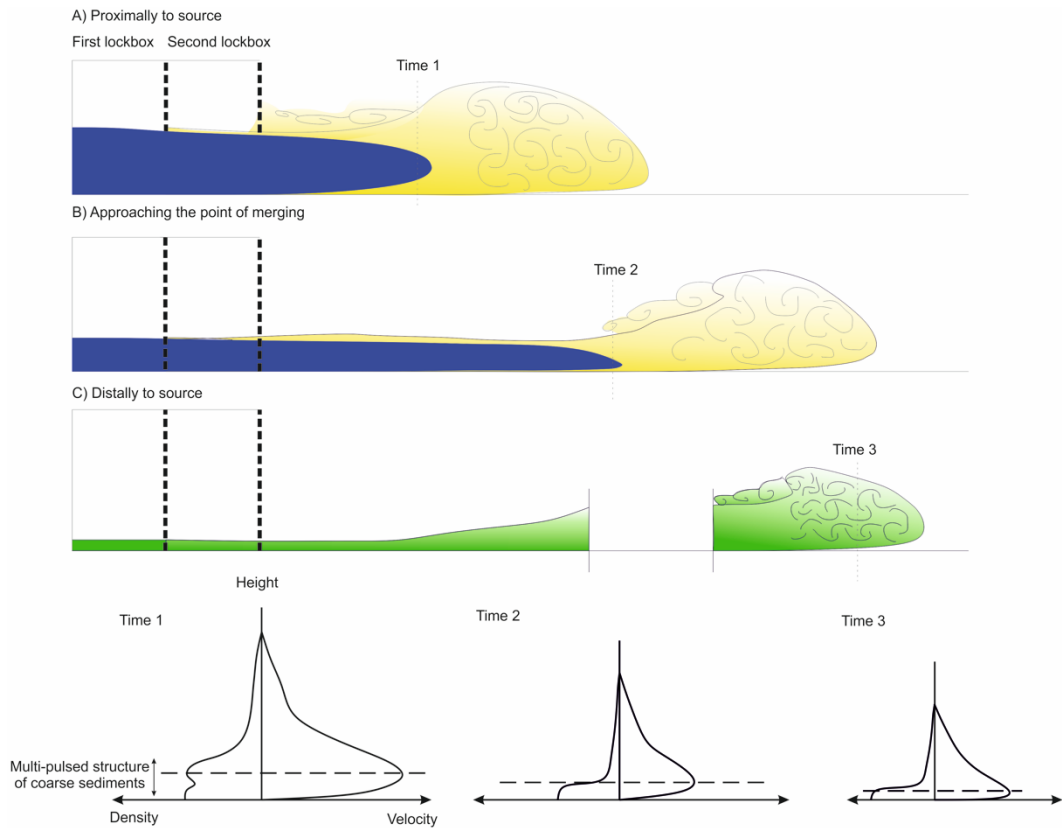


Figure 5.16 - Conceptual model describing the deposition of multi-pulsed flows: A) Shortly after second pulse release, B) Approaching the point of merging and C) Beyond the point of merging. Notes: i) three conceptual density/velocity profiles account for the dynamics at the second flow front at three characteristic timescales, ii) the same density/velocity and height axis scheme applies for all three plots, iii) dashed lines in the density/velocity models indicate positions of velocity maximum.

Within the time between two slumping episodes, the first pulse has developed a vertical density stratification due to incipient deposition and entrainment of ambient fluid. Ambient water entrainment commonly occurs both at the flow front and above the whole flow body (Chapters 3 and 4; Gladstone et al., 1998; Peakall et al., 2000; Sher & Woods, 2015). Such density stratification is also enhanced by the lagged settling of sediments with different grain sizes (Middleton & Hampton, 1973; van de Berg et al., 2017). Therefore, a highly-concentrated near-bed layer comprising coarse sediments (with high settling velocities) may develop; above this layer, the flow becomes relatively dilute due

to ambient entrainment (e.g., Kneller & Buckee, 2000). The upper boundary of the dense layer and the level of velocity maximum may not match. In addition, prior to the second pulse release, coarse sediments of certain sizes initially suspended within the first flow component might have been deposited, if their settling velocity is greater than shear velocity of the flow.

Upon removing the second lock gate, the second pulse collapses into the first one and starts to form an inter-flow intrusion. Since the density difference between the two pulses is smaller than that between the first pulse and the ambient, mixing between the two pulses is initially suppressed. The first pulse becomes progressively less dense due to deposition and ambient water entrainment, while the density of the second pulse is reduced mainly only by deposition. Therefore, the second pulse is always denser than the first. In addition, regardless of the density difference between the pulses, the second pulse's position is modulated by the velocity field within the first pulse and is elevated from the bed (Figs. 5.8 and 5.16A). As such, the intrusion is elevated along approximately the level of velocity maximum of the first pulse (see Fig. 5.16A). In addition, density stratification is also developed within the second pulse. Since the second pulse travels with higher velocity than that of the flow front, it progressively mixes with the first pulse and eventually reaches the flow front.

The sedimentation rate of the first pulse controls how long the second pulse is modulated. If the deposition of the first pulse's coarse sediments (prior to the second pulse's intrusion) is pronounced, density of the first pulse will have been significantly reduced by the point of second pulse release. Nevertheless, during a short period after withdrawing the second lock gate, the velocity field within the first pulse is likely still of sufficiently high magnitude that it can modulate the position of the second pulse. Such modulation can be maintained up to some distance proximal to the source. As a result of this modulation, the real-time net vertical sorting of sediments within the flow can be seen as a multi-pulsed profile (i.e., two coarse sediment intervals in the density profile, each attributed to a pulse; see Fig. 5.16A).

There are two main depositional processes that might take place at proximal locations, which relate to the deposition of coarse and fine sediments respectively. Coarse sediments are suspended within the lower part of the multi-pulsed flow and they incorporate the inverse-to-normal sediment intervals in density profile (Fig. 5.16A). Such sediments can be relatively quickly deposited due to their high settling velocity (see e.g., Postma et al. 1988; Gladstone & Sparks, 2002). The deposition might occur almost instantaneously as, or shortly after, the passage of the flow at a proximal sampling position, depending on relative scales between settling velocity of the coarse sediments and the shear velocity scale of the flow. Deposits from the second pulse (i.e., comprising the upper interval; Fig. 5.16A) might be superimposed onto that of the first pulse (i.e., comprising the lower interval). This sedimentary process of coarse sediments results in the deposition of multi-pulsed turbidites at proximal positions. It should be noted that the compositions of sediments in the two pulse components, at the time of deposition, do not have to be the same. This is because the first pulse might have partially deposited coarse sediments prior to the second pulse release. The transition in vertical grain size profile between multiple inverse-to-normal grading cycles can be smooth (cf. abrupt change in grain size in stacked turbidites; Chapter 3). This might be because lower part of coarse sediments within the dense, basal layer of the second pulse have been mixed with finer sediments (though still coarse, relatively to grain size range of the whole flow) in the first pulse, due to the modulation and strong density stratification in the first pulse. In addition, the multi-pulsed element in the deposit might be overlaid onto any coarse sediments previously deposited by the first pulse. At a later stage following the passage of the body and the tail, fine sediments incorporated mainly within the upper part of the flow will be deposited. This later depositional process occurs much more slowly over time, in comparison to the earlier deposition of the multi-pulsed element, due to the relatively low settling velocity of fine sediments. In prototype environments, these two sedimentary processes imply that multi-pulsed sediments can be found at least at locations proximal to the source. However, such spatial constraint on multi-pulsed turbidite deposition cannot be assessed directly within the scope of this study.

As the flow evolves further downstream, the first pulse becomes thinner and thus its level of velocity maximum is lowered. As the first flow now decelerates and its velocity field weakens, any modulation of the position of the second pulse front is likely significantly reduced. The second pulse now does not travel at the first pulse velocity maximum level but along the base of the flume. That means the vertical offset between the second pulse and the base of the whole flow is progressively reduced (Figs. 5.8 and 5.16). Depending on the magnitudes and scales of the two pulses (i.e., the strength of the associated slumping episode and the composition of sediments characterising each pulse), as soon as the second pulse is no longer elevated above the channel bed, the whole multi-pulsed flow will have an upward-fining sediment sorting. This means coarse sediments attributed from both pulses are very likely to be carried within a basal layer of the flow in and well-sorted. Since flow is now fully vertically stratified and suspended sediments are well sorted, uni-pulsed turbidites should be deposited. Hence, it is argued that the deposition of uni-pulsed turbidites can be enabled as soon as the second pulse fully reaches the bottom of the channel bed; this might occur even prior to the point of merging. Therefore, the temporal separation in arrival of the two pulses at any sampling position does not have to be reflected in the associated deposits. Nevertheless, it is straightforward to conclude that beyond merging point (see e.g., Chapters 3 and 4), the multi-pulsed flow evolves in a manner similar to how a single-pulsed flow of comparative scale behaves (Fig. 5.16C). Therefore, uni-pulsed turbidites must always be deposited beyond merging points. Occurrence of multi-pulsed turbidite deposits are thus constrained to be strictly within the merging length scales of the flow.

The scaling analysis presented in Chapter 4 is only applicable for estimating merging lengths ideally in saline flows in the two-lockbox model. By assuming that this scaling analysis can be applied for multi-pulsed turbidity currents at prototype settings, it still does not necessarily constrain the spatial persistence of multi-pulsed turbidites, given the variability in the modulation of the second pulse (see above). Nevertheless, distal turbidites found beyond merging points cannot be used to infer initiation mechanisms of multi-pulsed flows evolving on flat slopes;

whereas those found proximally very upstream of points of merging might reflect flow initiation mechanisms, depending on density scale of individual pulse components (section 5.3.4). Based on the experimental data presented in this chapter, it is unclear exactly on what length scales multi-pulsed turbidites may be deposited. This limitation of the research remains an open question and could be addressed by conducting further work.

If the condition on relative compositions and grain sizes between pulses is not met, multi-pulsed turbidites will not be deposited. Indeed, if sediments comprising the multi-pulsed component in Fig. 5.16A are not sufficiently coarse to enable a rapid deposition, only single-pulsed turbidites will be deposited. Due to low settling velocity, the sediments will progressively become well-sorted and their initial multi-pulsed sorting due to pulse intrusion, as described, will be lost upon deposition.

5.4.2.2 Limitations of the conceptual model and experimental methodology

The early deposition of single-pulsed turbidites prior to point of merging might result from limitations that inevitably arise in experimental modelling. The experimental configuration in this research deployed two identical pulses whose proportions of coarse sediments in the initial dense fluid are small (see Figs. 5.2 and 5.15). In addition, the proportion of coarse sediments in each flow component were significantly smaller than those of median and fine sediments. Since multi-pulsed turbidites might be mainly characterised by the deposition of multiple inverse-to-normal grading cycles of coarse grained (Fig. 5.12C, 0.7 m), the use of small proportion of coarse sediments might explain the absence of multi-pulsed turbidite deposition prior to merging points. Therefore, modifying the relative proportions between sediments of coarse and fine grainsizes in the composition of the initial sediment mixture might affect the flow dynamics. For example, increasing or decreasing the amount of fine sediments within turbidity current compositions can enhance or reduce the distances over which coarse sediments are transported (e.g., Gladstone & Woods, 2000). This is because fine sediments remain in suspension over longer times and thus sustain the associated flows.

Therefore, the composition of sediments comprising multi-pulsed flows might or might not permit the deposition of multi-pulsed turbidites prior to the point of merging (i.e., the amount of coarse sediment must be sufficiently large for multi-pulsed character to develop in any deposits).

The discussion on multi-pulsed flow depositional structure presented in this chapter disregards any effects of erosion and bypassing which might well occur during whole or parts of flow evolution in prototype environments (e.g., Rimoldi et al., 1996; Sultan et al., 2007; Stevenson et al., 2013). If erosion and/or bypassing are possible in multi-pulsed flows, given that relevant conditions for these phenomena are met, the deposition of multi-pulsed turbidites can be distorted and thus such multi-pulsed deposits would not be seen. This subject is discussed further in Chapter 6, where it is acknowledged that it remains a topic for future study.

5.5 CONCLUSIONS

Insights from experiments conducted to study the dynamics and deposition of sediment-bearing single- and multi-pulsed flows have suggested:

[1] Multi-pulsed flow dynamics transition from multiple waxing-waning cycles to a pattern of rapid waxing then monotonic waning (cf. single-pulsed flow dynamics). Such a transition is similar to what was observed in the dynamics of saline multi-pulsed flows.

[2] Delay times between pulses need to be greater than thresholds set for the backward-propagating waves generated upon the collapse of first fluid component to reach the second lock gate. Otherwise, multi-pulsed flows whose delay times between the pulses fall below such thresholds will be effectively behave as single-pulsed flows at the same scales. This observation is demonstrated by the visualisation and ADV data of the 0 s and 2.5 s delay time flows in this chapter.

[3] The longitudinal variation in the dynamics of multi-pulsed flows is not entirely reflected in the spatial variation of the flow deposits. A model in which the deposition of multi-pulsed turbidites is possible within short distances from

source was presented. However, such deposition need not be persistent up to distances where pulses merge completely (i.e., points of merging).

[4] Turbidites found beyond the point of pulse merging cannot be used in the interpretation of flow initiation mechanisms as they are single-pulsed deposits and thus carry no pulsing signals.

[5] Although the spatial persistence of multi-pulsed turbidites could not be deduced from this study, turbidites found very proximally to sources can carry flow initiation signals. However, the scaling analysis conducted based on data from saline flows presented in Chapter 4, if applicable in turbidity currents, only provides an upper limit on merging lengths (see points 3 and 4, above); single-pulsed turbidites may form before this point.

[6] Limitations in the conceptual model and experimental set-up were evaluated such that the grain size range of suspended sediments might have been too deficient in coarse material to permit the deposition of multi-pulsed turbidite up to the points of merging. Modifying the relative scales of two pulses and the grain size of suspended sediment might enable greater spatial persistence of multi-pulsed turbidites. Such considerations might be a topic for further research.

Chapter 6

Discussion and Conclusions

6.1 COMPARISON OF THE DYNAMICS OF SALINE AND SEDIMENT-BEARING MULTI-PULSED FLOWS

6.1.1 Longitudinal variation in velocity structures

The experiments conducted to model saline multi-pulsed flow (Chapters 3 and 4) and sediment-bearing multi-pulsed flow (Chapter 5) showed that these flows exhibited similar downstream evolution in longitudinal velocity profiles. Proximally, two distinct pulses were seen; the temporal separation between the pulses was progressively reduced as the second pulse in the multi-pulsed flows was advected forwards, towards a point of merging (Chapters 3, 4 and 5). At distal locations, beyond the merging point, distinct signals of two separate flow pulses were lost, i.e., flows exhibited uni-pulsed character. During the evolution of the multi-pulsed flows, the velocity maximum was observed at a height above the base of approximately 25% of flow depth. The velocity within the bodies of the flows was always higher than that of the flow fronts. These similarities in gross velocity structure permit multi-pulsed saline flows to be used as proxy for their sediment-bearing counterparts in the study of multi-pulsed turbidity current dynamics.

6.1.2 Dynamics of the second pulse within a multi-pulsed flow

The second pulse in saline flows intruded into the first and was modulated by the velocity field within the first pulse. Therefore, there was a vertical separation between the material comprising the second pulse and the channel bed. This process was sustained up to the point of merging as the second flow component travelled within the first as an intrusion. However, within sediment-bearing multi-pulsed flow experiments, after a relatively short period during which the second

pulse was advected towards the flow front, it started to intrude into the first pulse along the bottom of the channel bed. These two pulses progressively merged in a manner similar to that observed in the saline flow experiments.

In multi-pulsed sediment-bearing (turbidity current) experiments, the relatively early shredding of initiation signals in depositional structures was possible (i.e., uni-pulsed turbidites replaced multi-pulsed deposits before the point of merging; Chapter 5). This phenomenon might be explained by the greater rate at which the density of the first pulse was reduced during run-out due to deposition and ambient water entrainment, compared to compositionally-driven counterparts. Thus, in saline flow experiments, turbulent mixing occurring both at the flow front and on top of the whole current decreased the flow density. However, the bottom layer of the flow remained relatively dense since it was not mixed with the ambient and there was no deposition (cf. sediment-bearing flows). This basal layer of the flow thus maintained a relatively strong velocity field which would have been capable of modulating the second pulse position over a longer duration, in comparison to the modulation in the sediment-bearing flows. In sediment-bearing flow experiments, the deposition of sediments suspended in the dense bottom layer of the flow decreased the flow density significantly. Hence, the first pulse became much less dense prior to the arrival of the second pulse. The velocity field within the first pulse is therefore thought to have subsequently become progressively weaker.

In addition, the vertical offset between the second pulse position and the channel bed progressively decreased such that the second flow component eventually travelled along the bases of the flume. Even though the cyclically waxing-waning structure in longitudinal velocity variation persisted up to the merging point, it can be noted that the second pulse may have reached the bed even prior to this point. In this case deposits found beyond the point where the second pulse had reached the bed was similar to that observed in single-pulsed flow experiments.

An additional factor in the relatively subtle development of multi-pulsed deposits may have been the relatively low proportion of the coarse tail within the suspended sediment load; early sedimentation of this coarse tail (upstream of the first sampling point) may have rendered the multi-pulsed flows only weakly capable or incapable of recording the passage of pulses by an associated coarsening-up trend in the deposit.

6.2 MERGING LENGTHS IN MULTI-PULSED FLOWS

The merging lengths observed in the saline flow experiments only constrain the distances over which the cyclically waxing-waning velocity structure of multi-pulsed gravity currents can be observed (Chapter 4). Therefore, the scaling analysis can be used to estimate merging lengths in multi-pulsed saline flows. Such lengthscales do not necessarily reflect the spatial persistence of multi-pulsed turbidite deposition in multi-pulsed sediment-bearing counterparts (Chapter 5). The reasons are i) the scaling analysis is calibrated to experimental data of saline flow model and ii) as suggested by the sediment-bearing flow experiments, single-pulsed turbidites might start to be deposited even prior to merging point. Thus, although the scaling analysis presented in Chapter 4 stands as a useful initial model which might be useful in predicting merging lengths for multi-pulsed turbidity currents, it cannot directly predict the spatial persistence of multi-pulsed turbidite deposition. The actual applicability of this model in turbidity current scenarios awaits validation from field-based data. Nevertheless, given that saline flows can act as proxies for turbidity currents, the results of Chapter 4 do confirm that merging lengthscale observed in either compositionally-driven or sediment-bearing flows is a function of initial flow parameters.

Here, by assuming that the model is applicable for turbidity currents, estimated merging lengths appear to be relatively short compared to the lengthscales in the prototype environments in which multi-pulsed turbidites are found. The experiments to model multi-pulsed saline and sediment-bearing flows were configured such that the flows were generated by a simplified setting of short, adjacent lockboxes, opened in upstream sequence (see Chapters 3, 4 and

5) within a flume with a horizontal base. Such an experimental set-up enables the generation and evolution of the multi-pulsed flows on a zero-gradient slope. However, it remains a moot point whether this experimental set-up appropriately models the initiation mechanisms believed to operate in prototype settings. In addition, it is not straightforward within the scope of this research to determine the degree to which predicted merging lengths can be used to constrain interpretations of deposits from prototype environments in terms of initiation mechanism.

The interpretation of the experimental data presented in Chapters 3, 4 and 5 disregards erosion and bypass which might occur in prototype environments. In this section, the possibility of observing longer and shorter merging lengths in natural settings is discussed with a focus on the assumptions, and configurations, of the initial flow conditions that support this study. Here, such merging lengthscales are relative to those observed when the assumptions on non-erosion, non-bypassing and zero-gradient slopes are held.

6.2.1 Multi-pulsed turbidite deposition with possibility of erosion and bypassing

In the discussion of multi-pulsed turbidite deposition, erosion has not been considered (e.g., Amy et al., 2005). However, erosion and bypass processes are very common in natural settings; erosion (re-entrainment) normally occurs simultaneously with deposition (e.g., Rimoldi et al., 1996; Sultan et al., 2007; Stevenson et al., 2013), the exception being when the force available to keep material in suspension is less than that for incipient motion of sediment from the bed (see Dorrell et al., 2013; Dorrell et al., 2018). Depending on flow composition (i.e., variation of flow density with depth, Dorrell et al., 2013; Dorrell et al., 2018) and shear stress a turbidity current might be net depositional or net erosional at different points during run-out. Here, bypassing flows are defined as those that do not leave a depositional record (i.e., flows are net erosional or where the rate of erosion balances the rate of deposition).

Closely-spaced slumping episodes and the combination of associated flows can explain the formation of multi-pulsed flows (e.g., Goldfinger et al., 2003). However, the delay times between the pulses (i.e., duration between two successive slumping episodes) affects the dynamics and deposition of multi-pulsed flows (Chapters 4 and 5). If delay times are sufficiently long such that the first pulse starts to deposit prior to the arrival of the second pulse, this second pulse, if capable, might erode materials from the first pulse's deposit. Nevertheless, the second pulse is still advected towards the flow front. As two flow components interact with each other the erosion process might occur simultaneously with deposition. Given that the first pulse progressively decelerates and as a result of the erosion the second pulse now accelerates, the latter may reach the flow front more quickly and thus shorten the merging length.

In this the prototype setting, the multi-pulsed turbidites deposited by the flow within which a second pulse is erosional are termed 'amalgamated' turbidites (cf. Van Daele et al., 2017; Chapter 3). Such depositional structures are characterised by sharp erosional surfaces between different inverse-to-normal grading cycles within the multi-pulsed turbidites (Chapter 3). Examples of long temporal delays between multiple pulses initiated by successive submarine slumping (i.e., hours to days) can be seen from shock/aftershock events (e.g., Piper et al., 1999; Canals et al., 2004).

Therefore, it could be argued that merging lengths could only be longer if either the first pulse or both of the pulses erode materials which have been deposited previously in other flow events. Regarding the latter case, a further condition would be that the re-entrainment of sediments in the first pulse is more significant. Adding erodible sediments into the multi-pulsed flow in these manners can result in an enhancement in excess density of the flow. Such increase in the density can further run-out distance of the first pulse and thus extend merging length. Thus the degree to which merging lengths can be extended may depend on relative depositional and erosional rates between the pulses. As such, the best-case scenario to extend pulse merging lengths occurs when the rate of second pulse acceleration as a result of re-entrainment is smaller than that of the

first pulse. In this case the first pulse component can accelerate at higher velocity and reach a more distal location, in comparison with the first pulse of a non-erosional flow. Then, given that merging of two pulses is an inevitable phenomenon in multi-pulsed flow evolution, the second pulse will eventually be advected towards the flow front and merging length in this case will be longer.

6.2.2 Flows generated on slopes

Due to experimental constraints, the flume was set on a zero gradient, whereas negative slope (looking downstream) in the upstream area (generally the continental slopes) is generally seen along turbidity current pathways (e.g., Mulder & Alexander, 2001; Paola et al., 2009; Meiburg & Kneller, 2010; Xu et al., 2014). Indeed, it is common that submarine slumping occurs on slopes. Although low- or zero-gradient sectors may be encountered on continental slopes, extensive areas of such gradients are generally only encountered in the deep ocean environments eventually reached by flows sourced from upstream continental slopes. It follows that a limitation of the experimental set-up is that flows were both generated and evolved on zero-gradient lower boundaries.

Turbidity currents commonly evolve on gradient slopes and thus the flows accelerate significantly during their initial phases (e.g., Middleton & Hampton, 1973; Paola et al., 2009; Monaghan, 2007); it can be envisaged that in natural settings, merging lengths of multi-pulsed flows initiated on slopes and eventually reaching areas of zero-gradient sea bed could be longer. Thus, in the experiments, flow velocity - and hence turbulence - was solely maintained by the conversion of the potential energy represented by the initial density difference between the ambient and the dense fluid to kinetic energy. In prototype environments, gradients enable flows to convert a greater potential energy into kinetic energy, depending on their run-out length. The phenomenon can both increase velocity and enhance the turbulence within each pulse of a multi-pulsed turbidity currents, possibly at the same rate. Therefore, it is thought that the pulses in natural settings can reach localities more distal than the lengthscales observed using the experimental analogue directly, i.e., with pulses merging at greater distances from

source. This consideration extends to predictions made on the basis of the scaling analysis presented in Chapter 4, which does not take this factor into account.

6.2.3 Multi-pulsed flows comprised by two initial flow components of different compositions and volumes

The simplified experimental set-up in this study assumes that individual pulse components of a multi-pulsed flow have the same volume and composition. However, in prototype environments, these parameters might vary between the two components. As an example, the volume of sediments collapsing from continental shelf due to a main shock event (i.e., first pulse) is commonly greater than that of the collapse due to an aftershock event (i.e., second pulse), given their different seismic magnitudes. At laboratory scale, this can be seen as the difference between the first and second lock lengths. In this section, two end-member examples on differences between these two initial parameters of the pulses will be discussed.

If the compositions, i.e., densities, of two pulses are the same, a difference in lock length can warrant a further travel distance of the first pulse prior to merging with the second pulse. At the beginning of slumping phase, initial flow height and density control the velocity of the first pulse ($U = \sqrt{g'h}$, Chapter 4); the importance of lock length is negligible. However, as the flux of dense fluid supplied into the first pulse increases, since the first pulse has more materials to run out, the rate at which it becomes dilute due to deposition and ambient entrainment is reduced. The first pulse in this case remains dense over a longer period compared to a pulse with shorter lock length (i.e., slumping phase is longer). Therefore, upon merging with the second pulse, the first pulse has reached a further distance from the source. Merging lengths therefore will be longer in this scenario.

If the two pulses have different initial sediment components but the same volume, the condition for a longer merging length is that the second pulse needs to be less dense than the first pulse. Such a difference in density will ensure that

the first pulse can travel to further distance from source before merging of the second pulse occurs. Although the velocity of the second pulse in this case might be much smaller than that of the first, once reaching the body of the first flow component, the second pulse will be eventually advected towards the flow front.

6.3 MULTI-PULSED TURBIDITE DEPOSITIONAL MODEL AND APPLICATION

As discussed in Chapter 3, the degree of deviation in depositional structures of turbidites from the classic normal, upward-fining grading profiles depends on the dynamics of the associated overpassing flows. Here, deposition of stacked, amalgamated, multi-pulsed and single-pulsed turbidites is discussed.

As described in Chapter 3, stacked turbidites are defined as vertically juxtaposed deposits of individual flows. If two individual, temporally separate turbidity currents are initiated such that there is no initial interaction between them (i.e., no intrusion occurring between the two flows), stacked turbidites can be deposited. Given the same temporal separation between the two flows, if the second flow is erosional, an amalgamated turbidite may develop. The stacked turbidite deposited by the two flows might be characterised by an abrupt change in grain size of the deposits, from fine to coarse grains, depending on how low a later flow erodes into the deposit of an earlier one. This is because two components of the turbidite are deposited separately by two individual flows (Chapter 3); the temporal separation between their arrivals at any sampling position is sufficiently long such that fine sediments suspended within the first flow have been deposited.

If two flows interact due to shorter delay time in flow initiation (i.e., the second flow can reach the tail of the first flow after being initiated), the second pulse will be progressively advected towards the flow front of the first. This is the pulse intrusion phenomenon described throughout this study. Possible longitudinal variations in the vertical grading structure of associated deposits are summarised in Fig. 6.1. Proximally to source either amalgamated or multi-pulsed

turbidites could be deposited, depending on whether the second pulse is erosional. Multi-pulsed turbidites, deposited without erosion, would exhibit a continuous transition in the inverse-to-normal grading elements (Chapter 3, Fig. 3.9). If the second pulse is erosional into sediments deposited by the first, deposits will have the amalgamated character with a sharp interface between multiple inverse-to-normal grading cycles (see Chapter 3 and Fig. 6.1). In this case, the change in grain size reflected in vertical grading structure would be abrupt if the degree of erosion is significant.

The longitudinal variation in depositional structures thus transitions from being multi-pulsed or amalgamated to being single-pulsed (Fig. 6.1). This interpretation is based on the experimental data from both saline and sediment-bearing flow experiments. It suggests an approach to study the linkage between deposits and initiation mechanisms of multi-pulsed flows. As such, provided that multi-pulsed turbidites found in prototype environments can be correlated to updip deposits of the same character and to downdip single-pulsed turbidites, a reconstruction of flow dynamics and initiation mechanism is possible. This correlation technique can help further the current understanding of, and broaden the interpretational template for multi-pulsed turbidites (see example of Cascadia channel system in Chapter 3; Van Daele et al., 2017). Even where direct correlation between updip multi-pulsed and downdip single-pulsed turbidites might not be straightforward, this alternative approach suggests a strong possibility of variation in the depositional structures due to the pulse merging phenomenon in overpassing flow/s (see example of Sumatran area in Chapter 3). However, this interpretation is only possible if topography data can reliably demonstrate that the updip multi-pulsed and downdip single-pulsed deposits can lie on the same pathway. Further, the result can be extended to the study of modern outcrops; pulse merging in turbidity currents and the subsequent variation in longitudinal structures of their deposits can now potentially be used in deposit correlation using field data.

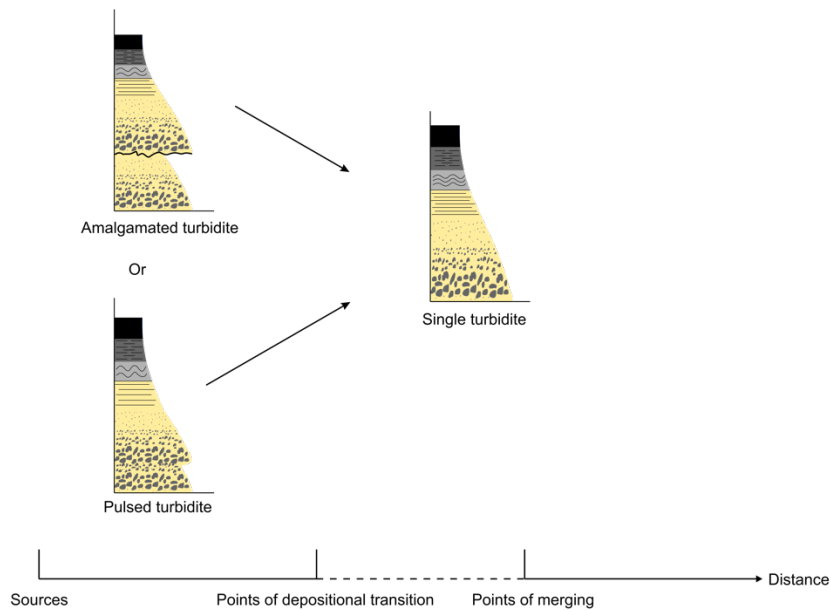


Figure 6.1 - Conceptual model of the longitudinal variation of turbidite deposition.

Note: i) deposit depth and grain size are not drawn to scale, ii) points of depositional transition indicate where single-pulsed turbidites start to be deposited and iii) dashed line indicates the distance prior to points of merging within which single-pulsed turbidites might be deposited.

As discussed in Chapter 5, the point at which single-pulsed turbidites start to be deposited could be prior to or at the point of merging, depending on the scales and composition of the individual flows. Regardless, it can be confirmed that such lengthscales are always constrained by upper thresholds defined by merging lengths, such that beyond these distances only single-pulsed turbidites are always deposited. The merging lengths then might be estimated using the scaling analysis suggested in Chapter 4 (though the direct applicability of the model still needs to be evaluated). In any case, turbidites found within merging distances can potentially be used in the interpretation of flow initiation mechanisms whereas those found distally, beyond points of merging, cannot record such initiation signals. In addition, as implied by the results of Chapter 4, merging lengths of multi-pulsed turbidity currents must be a function of initial flow conditions. Length of breaches (i.e., defined as axial extension of collapse caused by earthquakes) is a controlling parameter in the dependence of merging lengths on initial parameters.

The discussion of longitudinal variation of depositional structures herein carry assumptions that sediment bypass can be disregarded and that the individual flows carry sediment comprising a wide range of relative grain size. As inferred in Chapter 5, the proportion of coarse sediments needs to be sufficiently high for a pulse-related inverse grading signature to be detectable in the deposit. If the variation of grain size is insignificant (i.e., as the suspended sediment population tends towards being monodisperse) and/or the proportion of coarse sediments is too small, it is very unlikely that multi-pulsed turbidites can be deposited and/or recorded. This is because the inverse-to-normal grading cycles are mainly expressed in relatively coarser sediments (see Chapter 5). Therefore, this study is yet to establish the exact correspondence between depositional structures and flow initiation mechanisms.

6.4 CONCLUSIONS

6.4.1 Summary of observation from experimental data

In summary, data from all three experimental components (Chapters 3, 4 and 5) suggest that a second pulse within a multi-pulsed flow is progressively advected towards the flow front. The second pulse eventually merges with the first at the point of merging. As the two pulses merge, the whole multi-pulsed flow then evolves in a similar manner to that of single-pulsed flow. Given that waning flows suggest upward-fining deposition and waxing flows suggest the opposite, an interpretation based solely on data from saline flow experiments (Chapters 3 & 4) suggests that multi-pulsed turbidites can be deposited up to the point of merging; beyond this point only single-pulsed turbidites are deposited. Flow initiation signals might thus be preserved within localities proximal to source, progressively lost as multi-pulsed flows approach the point of merging and eventually shredded once pulses merge completely.

Lengthscales over which the persistence of the cyclically waxing-waning velocity structure in multi-pulsed saline flows (i.e., up to the point of merging) were assessed (Chapter 4). The spatial persistence of multi-pulsed turbidite

deposition might be estimated using the scaling analysis presented in this study or a similar model. However, this subject requires further verification and study. The application of such scaling analysis is probably limited to multi-pulsed flows initiated by short, sequential submarine breaches (<10 km) and propagating over quasi-horizontal flow pathways, as the experiments were tailored to model this setting.

The experiments conducted to model sediment-bearing flows provide a better understanding of the longitudinal variation of multi-pulsed flow dynamics and depositional structures. Although the velocity structure was comparable to that observed in saline flow experiments, spatial variation of the associated deposits shows deviations from the interpretation of the saline flow experimental data (Chapters 3 and 5). Multi-pulsed turbidites were deposited very proximally to source. However, the deposition of such deposits might not persist up to point of merging as there might be an early shredding of flow initiation signals. The lengthscales over which multi-pulsed turbidite deposition persists might be different from merging lengthscales, depending on the composition and scale of the pulses in a multi-pulsed flow. Thus, the variation in flow velocity structure does not have to be strictly reflected in the spatial variation of the deposits.

The deposition of multi-pulsed deposits from multi-pulsed flows may occur if the range of sediments comprising the individual pulses in a multi-pulsed flow is sufficiently large and the proportion of coarse sediments is high enough to allow a coarsening-up interval to be deposited under conditions of waxing flow. In addition, the settling velocity of sediments which comprise the multi-pulsed element in real-time density profiles of the overpassing flow needs to be sufficiently high to enable deposition of multi-pulsed turbidites on the time scale of episodes of flow waxing. Otherwise, a multi-pulsed characteristic of sediment sorting in the flow will not be recorded in the deposit due to low settling velocity. The condition of having a wide range of grain sizes and a relatively high proportion of coarse sediments were not met very effectively in the deployed experimental configurations. In addition, erosion and bypass are disregarded in the interpretation which otherwise could occur in prototype environments and might

explain any early loss of flow initiation signals and absence of multi-pulsed deposits proximally to the source.

6.4.2 Suggestions for future research

Within this study, the pulse merging phenomenon is observed in multi-pulsed saline flows modelled under a wide range of boundary conditions. Also, the variations in dynamics of saline and sediment-bearing multi-pulsed flows are confirmed to be similar. However, modelling of sediment-bearing flows does not take into account variation in the composition of the initial sediment mixture (i.e., also initial density). The experimental data in Chapter 6 suggest that there might be an early shredding of flow initiation signals (i.e., deposition of single-pulsed turbidites prior to the point of merging); this could be as a result of the deployed sediment composition. Thus, varying this boundary condition in multi-pulsed flow experiments could be a subject of future research so as to consider the variation in spatial persistence of multi-pulsed turbidite deposition. For example, one approach would be to design experiments in which the effects of varying in the composition of initial sediment mixture can be assessed. In this case the ratio of fine/coarse sediments and/or the amount of sediments used in the experiments could be varied. Conducting such experiments could also help provide assurance as to whether the pulsing phenomenon can be seen under wider range of experimental conditions (i.e., other than those presented in Chapter 5). In addition, such work would help to constrain how the variation in the relative proportions of fine/coarse sediments could affect run out distance of multi-pulsed flows, if generated, and thus merging lengths.

It can be imagined that modelling multi-pulsed flows numerically by varying initial flow conditions (i.e., lockbox dimensions, ambient height, delay time, density, composition of sediment) could also be useful. Such modelling would enable observation of multi-pulsed flow evolution and dynamics under much wider range of initial flow conditions. For example, due to the constraint on the length of the flume (i.e., 5 m) used in this study, the delay time between pulses could not be longer than 8 s as otherwise merging of pulses would not be captured

within the length of the flume (i.e., point of merging is beyond 5 m distance). Where possible, numerical and experimental data regarding flow dynamics and depositional structures could be compared. In addition, numerical study could better model the deposition of multi-pulsed flows; one focus could be to distinguish the contribution to deposition from each pulse.

Furthermore, because the current experimental setup does not distinguish the contribution of sediments in deposition from each pulse, it would be useful to consider dyeing sediments comprising each flow component using two different colours. Alongside analysing the grading structure of the deposits as conducted in Chapter 5, visually separating sediments from each pulse would enable the relative contribution in deposition of the pulses at any sampling positions to be assessed. In principle, this approach could also help determine the consequences when the second pulse in a multi-pulsed flow of certain initial flow conditions was erosional. In such scenarios, the relative contribution in sediments from each pulse can be assessed.

In this study, multi-pulsed flows initiated by the combination of multiple single-pulsed flows at confluences are not modelled. Therefore, producing an analogue to model flow combination might develop understanding of multi-pulsed flow development and subsequent behaviour in confluence settings. Boundary conditions controlling multi-pulsed flow generation in these settings are likely i) the amount of sediments comprising each individual flow and ii) the lengths of upstream flow pathways. Conducting experimental research to model single-pulsed flow combination by varying these two conditions could thus confirm whether, and to what extent, the generation of multi-pulsed flows is possible.

References

- Abad, J.D., Sequeiros, O.E., Spinewine, B., Pirmez, C., Garcia, M.H. and Parker, G.** (2011) Secondary current of saline underflow in highly meandering channel: Experiments and theory. *J. Sed. Res.*, **81**, 787-813.
- Agimelen, O.S., Hamilton, P., Haley, I., Nordon, A., Vasile, M., Sefcik, J. and Mulholland, J.** (2015) Estimation of particle size distribution and aspect ratio of non-spherical particles from chord length distribution. *Chem. Eng. Sci.*, **123**, 629-640.
- Allen, J.R.L.** (1971) Mixing at turbidity current heads, and its geological implications. *J. Sediment. Petrol.*, **41**, 97-113.
- Amy, L.A., Peakall, J. and Talling, P.J.** (2005) Density- and viscosity-stratified gravity currents: Insight from laboratory experiments and implications for submarine flow deposits. *Sed. Geol.*, **179**, 5-29.
- Baas, J.H., Haughton, P.D.W. and Choux, C.** (2005) Coupling between suspended sediment distribution and turbulence structure in a laboratory turbidity current. *J. Geophys. Res.*, **110**, C11015, 20pp, doi:10.1029/2004JC002668.
- Baas, J.H., van Kesteren, W. and Postma, G.** (2004) Deposits of depletive high-density turbidity currents: a flume analogue of bed geometry, structure and texture. *Sedimentology*, **51**, 1053-1088.
- Babonneau, N., Savoye, B., Cremer, M. and Bez, M.** (2010) Sedimentary architecture in meanders of a submarine channel: Detailed study of the present Congo turbidite channel (Zaiango project). *J. Sed. Res.*, **80**, 852-866.
- Bagnold, R.A.** (1962) Auto-suspension of transported sediment; turbidity currents. *R. Soc. Lond. Proc.*, **A265**, 315-319.
- Basilici, G., de Luca, P.H.V. and Poiré, D.G.** (2012) Hummocky cross-stratification-like structures and combined-flow ripples in the Punta Negra Formation (Lower-Middle Devonian, Argentine Precordillera): A turbiditic deep-water or storm-dominated prodelta inner-shelf system? *Sed. Geol.*, **267–268**, 73-92.
- Beeson, J.W., Johnson, S.Y., Goldfinger, C. and Ross, A.F.** (2017) The

transtensional offshore portion of the northern San Andreas fault: Fault zone geometry, late Pleistocene to Holocene sediment deposition, shallow deformation patterns, and asymmetric basin growth. *Geosphere*, **13**, 1-34.

Benjamin, T.B. (1968) Gravity currents and related phenomena. *J. Fluid Mech.*, **31**, 209-248.

Bernhardt, A., Melnick, D., Hebbeln, D., Lückge, A. and Strecker, M.R. (2015) Turbidite paleoseismology along the active continental margin of Chile – Feasible or not? *Quat. Sci. Rev.*, **120**, 71-92.

Best, J.L., Kostaschuk, R.A., Peakall, J., Villard, P.V. and Franklin, M. (2005) Whole flow field dynamics and velocity pulsing within natural sediment-laden underflows. *Geology*, **33**, 765-768.

Bolster, D., Hang, A. and Linden, P.F. (2008) The front speed of intrusion into a continuously stratified medium. *J. Fluid Mech.*, **594**, 369-377.

Bonnecaze, R.T., Huppert, H.E. and Lister, J.R. (1993) Particle-driven gravity currents. *J. Fluid Mech.*, **250**, 339-369.

Bouma, A.H. (1962) Sedimentology of some Flysch Deposits: A Graphic Approach to Facies Interpretation. Elsevier, Amsterdam, 168 pp.

Brand, A., Noss, C., Dinkel, C. and Holzner, M. (2016) High-resolution measurements of turbulent flow close to the sediment-water interface using a bistatic acoustic profiler. *J. Atmospheric Ocean. Technol.*, **33**, 769-788.

Britter, R.E. and Simpson, J.E. (1978) Experiments on the dynamics of a gravity current head. *J. Fluid Mech.*, **88**, 223-240.

Britter, R.E. and Simpson, J.E. (1981) A note on the structure of the head of an intrusive gravity current. *J. Fluid Mech.*, **112**, 459-466.

Buckingham, E. (1914) On physically similar systems; illustrations of the use of dimensional equations. *Phys. Rev.*, **4**, 345-376.

Bull, S., Cartwright, J. and Huuse, M. (2009) A subsurface evacuation model for submarine slope failure. *Basin Res.*, **21**, 433-443.

Canals, M., Lastras, G., Urgeles, R., Casamor, J.L., Mienert, J., Cattaneo, A., De Batist, M., Hafliadason, H., Imbo, Y., Laberg, J.S., Locat, J., Long, D., Longva, O., Masson, D.G., Sultan, N., Trincardi, F. and Bryn, P. (2004) Slope failure

dynamics and impacts from seafloor and shallow sub-seafloor geophysical data: Case studies from the COSTA project. *Mar. Geol.*, **213**, 9-72.

- Carter, L., Milliman, J. D., Talling P. J., Gavey, R. and Wynn, R. B.** (2012) Near-synchronous and delayed initiation of long run-out submarine sediment flows from record-breaking river flood, offshore Taiwan. *Geophys. Res. Lett.*, **39**, L12603.
- Chikita, K.** (1990) Sedimentation by river-induced turbidity currents: field measurements and interpretation. *Sedimentology*, **37**, 891-905.
- Chikita, K. and Okumura, Y.** (1990) Dynamics of turbidity currents measured in Katsurazawa reservoir, Hokkaido, Japan. *J. Hydrol.*, **117**, 323-338.
- Choux, C.M. and Druitt, T.H.** (2002) Analogue study of particle segregation in pyroclastic density currents, with implications for the emplacement mechanisms of large ignimbrites. *Sedimentology*, **49**, 907-928.
- Cooper, C., Wood, J. and Andrieux, A.** (2013) *Turbidity current measurements in the Congo Canyon. OTC Abstract 23992.* Paper presented at Offshore Technology Conference, 6-9May, Houston, Texas 12pp.
- Craig, R.G.A., Loadman, C., Clement, B., Rusello, P.J. and Siegel, E.** (2011) Characterization and testing of a new bistatic profiling acoustic doppler velocimeter: The Vectrino-II. Proceedings of the IEEE/OES/CWTM *Tenth Working Conference on Current Measurement Technology*, Monterey, CA, 246-252.
- Curran, J.C. and Waters, K.A.** (2014) The importance of bed sediment sand content for the structure of a static armor layer in a gravel bed river. *J. Geophys. Res. Earth Surf.*, **119**, 1484-1497.
- Darby, S.E. and Peakall, J.** (2012) Modelling the equilibrium bed topography of submarine meanders that exhibit reversed secondary flows. *Geomorphology*, **163-164**, 99-109.
- Dasgupta, P.** (2003) Sediment gravity flow – the conceptual problems. *Earth Sci. Rev.*, **62**, 265-281.
- De Cesare, G., Boillat, J.-L. and Schleiss, A.J.** (2006) Circulation in stratified lakes due to flood-induced turbidity currents. *J. Environ. Eng.*, **132**, 1508-1517.

- de Rooij, F., Linden, P.F. and Dalziel, S.B.** (1999) Saline and particle-driven interfacial intrusions. *J. Fluid Mech.*, **389**, 303-334.
- Dengler, A.T., Wilde, P., Noda, E.K. and Normark, W.R.** (1984) Turbidity currents generated by hurricane Iwa. *Geo-Mar. Lett.*, **4**, 5-11.
- Di Federico, V., Cintoli, S. and Bizzarri, G.** (2006) Viscous spreading of non-Newtonian gravity currents in radial geometry. *WIT Transactions on Engineering Sciences*, **52**, 399-408.
- Dorrell, R.M., Amy, L.A., Peakall, J. and McCaffrey, W.D.** (2018) Particle size distribution controls the threshold between net sediment erosion and deposition in suspended load dominated flows. *Geophys. Res. Lett.*, **45**, 1443-1452.
- Dorrell, R.M., Hogg, A.J. and Pritchard, D.** (2013) Polydisperse suspensions: Erosion, deposition, and flow capacity. *J. Geophys. Res. Earth Surf.*, **118**, 1939-1955.
- Dorrell, R.M., Peakall, J., Sumner, E.J., Parsons, D.R., Darby, S.E., Wynn, R.B., Özsoy, E. and Tezcan, D.** (2016) Flow dynamics and mixing processes in hydraulic jump arrays: Implications for channel-lobe transition zones. *Mar. Geol.*, **381**, 181-193.
- Driscoll, N.W., Weissel, J.K. and Goff, J.A.** (2000) Potential for large-scale submarine slope failure and tsunami generation along the U.S. mid-Atlantic coast. *Geology*, **28**, 407-410.
- Dzulynski, S. and Sanders, J.E.** (1962) Current marks on firm mud bottoms. *Connecticut Academy of Arts and Sciences, Transactions*, **42**, 57-96.
- Eggenhuisen, J.T., McCaffrey, W.D., Haughton, P.D.W. and Butler, R.W.H.** (2010) Small-scale spatial variability in turbidity-current flow controlled by roughness resulting from substrate erosion: field evidence for a feedback mechanism. *J. Sed. Res.*, **80**, 129-136.
- Fan, J.** (2003) A modified Levenberg-Marquardt Algorithm for singular system of nonlinear equation. *J. Comput. Math.*, **21**, 625-636.
- Felix, M.** (2002) Flow structure of turbidity currents. *Sedimentology*, **49**, 397-419.
- Felix, M. and Peakall, J.** (2006) Transformation of debris flows into turbidity currents: mechanisms inferred from laboratory experiments.

Sedimentology, **53**, 107-123.

- Felix, M., Sturton, S. and Peakall, J.** (2005) Combined measurements of velocity and concentration in experimental turbidity currents. *Sed. Geol.*, **179**, 31-47.
- Ferrer-Boix, C., Martín-Vide, J.P. and Parker, G.** (2015) Sorting of a sand-gravel mixture in a Gilbert-type delta. *Sedimentology*, **62**, 1446-1465.
- Gadstone, C., Ritchie, L.J., Sparks, R.S.J. and Woods, A.W.** (2004) An experimental investigation of density-stratified inertial gravity currents. *Sedimentology*, **51**, 767-789.
- García, M.H. and Parsons, J.D.** (1996) Mixing at the front of gravity currents. *Dynam. Atmos. Ocean*, **24**, 197-205.
- GebCO** (2014). Available online at:
http://www.gebco.net/data_and_products/gridded_bathymetry_data/
- Gilbert, R., Crookshanks, S., Hodder, K.R., Spagnol, J. and Stull, R.B.** (2006) The record of an extreme flood in the sediments of montane Lillooet lake, British Columbia: implications for paleoenvironmental assessment. *J. Paleolimnol.*, **35**, 737-745.
- Gladstone, C. and Sparks, R.S.J.** (2002) The significance of grain-size breaks in turbidites and pyroclastic density current deposit. *J. Sed. Res.*, **72**, 182-191.
- Gladstone, C. and Woods, A.W.** (2000) On the application of box models to particle-driven gravity currents. *J. Fluid Mech.*, **416**, 187-195.
- Gladstone, C., Phillips, J.C. and Sparks, R.S.J.** (1998) Experiments on bidisperse, constant-volume gravity currents: propagation and sediment deposition. *Sedimentology*, **45**, 833-843.
- Gladstone, C., Ritchie, L.J., Sparks, R.S.J. and Woods, A.W.** (2004) An experimental investigation of density-stratified inertial gravity currents. *Sedimentology*, **51**, 767-789.
- Goldfinger, C., Galer, S., Beeson, J., Hamilton, T., Black, B., Romsos, C., Patton, J., Nelson C.H., Hausmann, R. and Morey, A.** (2016) The importance of site selection, sediment supply, and hydrodynamics: A case study of submarine paleoseismology on the northern Cascadia margin, Washington USA. *Mar. Geol.*, **384**, 4-46, <https://doi.org/10.1016/j.margeo.2016.06.008>.

- Goldfinger, C., Galer, S., Beeson, J., Hamilton, T., Black, B., Romsos, C., Patton, J., Nelson, C.H., Hausmann, R. and Morey, A.** (2017) The importance of site selection, sediment supply, and hydrodynamics: A case study of submarine paleoseismology on the northern Cascadia margin, Washington USA. *Mar. Geol.*, **384**, 4-46.
- Goldfinger, C., Grijalva, K., Bürgmann, R., Morey, A.E., Johnson, J.E., Nelson, C.H., Gutiérrez-Pastor, J., Ericsson, A., Karabanov, E., Chaytor, J.D., Patton, J. and Gràcia, E.** (2008) Late Holocene rupture of the northern San Andreas fault and possible stress linkage to the Cascadia subduction zone. *Earth Bulletin of the Seismological Society of America*, **98**, 861-889.
- Goldfinger, C., Morey, A.E., Nelson, C.H., Gutiérrez-Pastor, J., Johnson, J.E., Karabanov, E., Chaytor, J. and Eriksson, A.** (2007) Rupture lengths and temporal history of significant earthquakes on the offshore and north coast segments of the Northern San Andreas Fault based on turbidite stratigraphy. *Earth Planet. Sci. Lett.*, **254**, 9-27.
- Goldfinger, C., Nelson, C.H. and Johnson, J.E.** (2003) Holocene earthquake records from the Cascadia subduction zone and northern San Andreas Fault based on precise dating of offshore turbidites. *Annu. Rev. Earth Planet. Sci.*, **31**, 555-577.
- Goldfinger, C., Nelson, C.H., Morey, A.E., Johnson, J.E., Patton, J., Karabanov, E., Gutiérrez-Pastor, J., Eriksson, A.T., Gràcia, E., Dunhill, G., Enkin, R.J., Dallimore, A. and Vallier, T.** (2012) Turbidite event history—methods and implications for Holocene paleoseismicity of the Cascadia subduction zone. U.S. Geological Survey Professional Paper 1661-F, 170p. (Available free at <http://pubs.usgs.gov/pp/pp1661f/>).
- Gray, T.E., Alexander, J. and Leeder, M.R.** (2006) Longitudinal flow evolution and turbulence structure of dynamically similar, sustained, saline density and turbidity currents. *J. Geophys. Res.*, **111**, 14pp.
- Greaves, D., Boxall, J., Mulligan, J., Montesi, A., Creek, J., Sloan, E.D. and Koh, C.A.** (2008) Measuring the particle size of a known distribution using the focus beam reflectance measurement technique. *Chem. Eng. Sci.*, **63**, 5410-5419.

- Gutiérrez-Pastor, J., Nelson, C.H., Goldfinger, C. and Escutia, C. (2013)** Sedimentology of seismo-turbidites off the Cascadia and northern California active tectonic continental margins, northwest Pacific Ocean. *Mar. Geol.*, **336**, 99-119.
- Gutscher, M.-A., Baptista, M.A. and Miranda, J.M. (2006)** The Gibraltar Arc seismogenic zone (part 2): Constraints on a shallow east dipping fault plane source for the 1755 Lisbon earthquake provided by tsunami modelling and seismic intensity. *Tectonophysics*, **426**, 153-166.
- Hacker, J., Linden, P.F. and Dalziel, S.B. (1996)** Mixing in lock-release gravity currents. *Dynam. Atmos. Ocean*, **24**, 183-195.
- Hallworth, M.A. and Huppert, H.E. (1998)** Abrupt transitions in high-concentration, particle-driven gravity currents. *Phys. Fluids*, **5**, 1083-1087.
- Hallworth, M.A., Huppert, H.E., Phillips, J. C. and Sparks, R.S.J. (1996)** Entrainment into two-dimensional and axisymmetric turbulent gravity currents. *J. Fluid Mech.*, **308**, 289-311.
- Hallworth, M.A., Phillips, J.C., Huppert, H.E. and Sparks, R.S.J. (1993)** Entrainment in turbulent gravity currents. *Nature*, **362**, 829-831.
- Hand, B.M. (1997)** Inverse grading resulting from coarse-sediment transport lag. *J. Sed. Res.*, **67**, 124-129.
- Harris, T.C., Hogg, A.J. and Huppert, H.E. (2002)** Polydisperse particle-driven gravity currents. *J. Fluid Mech.*, **472**, 333-371.
- Härtel, C., Meiburg, E. and Necker, F. (2000)** Analysis and direct numerical simulation of the flow at a gravity current head. Part 1. Flow topology and front speed for slip and no-slip boundaries. *J. Fluid Mech.*, **418**, 189-212.
- Haughton, P.D.W. (1994)** Deposits of deflected and ponded turbidity currents, Sorbas Basin, Southeast Spain. *J. Sed. Res., Section A: Sedimentary Petrology and Processes*, **64**, 233-246.
- Heezen, B.C. and Ewing, W.M. (1952)** Turbidity currents and submarine slumps and the 1929 Grand Banks (Newfoundland) earthquake. *Am. J. Sci.*, **250**, 849-873.
- Ho, V.L., Dorrell, R.M., Keevil, G.M., Burns, A.D. and McCaffrey, W.D. (2018a)** Pulse propagation in turbidity currents. *Sedimentology*, **65**, 620-637.

- Ho, V.L., Dorrell, R.M., Keevil, G.M., Burns, A.D. and McCaffrey, W.D.** (2018b) Scaling analysis of multi-pulsed turbidity current evolution with application to turbidite interpretation. *J. Geophys. Res. Oceans*, **123**, 2017JC013463.
- Hogg, A.J., Nasr-Azadani, M.M. and Ungarish, M.** (2016) Sustained gravity currents in a channel. *J. Fluid Mech.*, **798**, 853–888.
- Holyer, J.Y. and Huppert, H.E.** (1980) Gravity currents entering a two-layer fluid. *J. Fluid Mech.*, **100**, 739–767.
- Hosseini, S.A., Shamsai, A. and Ataie-Ashtiani, B.** (2006) Synchronous measurements of the velocity and concentration in low density turbidity currents using an Acoustic Doppler Velocimeter. *Flow Meas. Instrum.*, **17**, 59-68.
- Hsu, S., Kuo, J., Lo, C., Tsai, C., Doo, W., Ku, C. and Sibuet, J.** (2008) Turbidity currents, submarine landslides and the 2006 Pingtung earthquake off SW Taiwan. *Terr. Atmos. Ocean. Sci.*, **19**, 767-772.
- Huang, J., Kaul, G., Utz, J., Hernandez, P., Wong, V., Bradley, D., Nagi, A. and O’Grady, D.** (2009) A PAT approach to improve process understanding of high shear wet granulation through in-line particle measurement using FBRM C35. *J. Pharm. Sci.*, **99**, 3205-3212.
- Hughes Clarke, J.E., Brucker, S., Muggah, J., Church, I., Cartwright, D., Kuus, P., Hamilton, T., Pratomo, D. and Eisan, B.** (2012) The Squamish ProDelta: Monitoring active landslide and turbidity currents. *New and Emerging Technology*, CHC2012, The Arctic, Old Challenges New, Niagara Falls, Canada 15-17 May 2012.
- Hughes, G.O.** (2016) Inside the head and tail of turbulent gravity current. *J. Fluid Mech.*, **790**, 1-4.
- Huppert, H.E.** (1982) Propagation of two-dimensional and axisymmetric viscous gravity currents over a rigid horizontal surface. *J. Fluid Mech.*, **121**, 43-58.
- Huppert, H.E.** (1998) Quantitative modelling of granular suspension flows. *Philosophical Transactions of the Royal Society A: Mathematical, Physical and Engineering Sciences*, **356**, 2471-2496.
- Huppert, H.E.** (2006) Gravity currents: A personal perspective. *J. Fluid Mech.*, **554**, 299-322.

- Huppert, H.E. and Simpson, J.E.** (1980) The slumping of gravity currents. *J. Fluid Mech.*, **99**, 785-799.
- Islam, M.A. and Imran, J.** (2010) Vertical structure of continuous release saline and turbidity currents. *J. Geophys. Res.*, **115**, 1-14, doi:10.1029/2009JC005365.
- Ismail, H., Viparelli, E. and Imran, J.** (2016) Confluence of density currents over an erodible bed. *J. Geophys. Res.*, **121**, 1251-1272.
- Janz, G.J. and Singer, S.K.** (1975) Copenhagen standard sea water: Conductivity and salinity. *J. Solution Chem.*, **4**, 995-1003.
- Jerolmack, D.J. and Paola, C.** (2010) Shredding of environmental signals by sediment transport. *Geophys. Res. Lett.*, **37**, 1-5.
- Johnson, C.G. and Hogg, A.J.** (2013) Entraining gravity currents. *J. Fluid Mech.*, **731**, 477-508.
- Johnson, H.P., Gomberg, J.S., Hautala, S.L. and Salmi, M.S.** (2017) Sediment gravity flows triggered by remotely generated earthquake waves. *J. Geophys. Res. Solid Earth*, **122**, doi:10.1002/2016JB013689.
- Johnson, J.M. and Satake, K.** (1994) Rupture extent of the 1938 Alaskan earthquake as inferred from tsunami waveforms, *Geophys. Res. Lett.*, **21**, 733-736.
- Khripounoff, A., Vangriesheim, A., Babonneau, N., Crassous, P., Dennielou, B. and Savoye, B.** (2003) Direct observation of intensity turbidity current activity in the Zaire submarine valley at 4000 m water depth. *Mar. Geol.*, **194**, 151-158.
- Kneller, B. and Buckee, C.** (2000) The structure and fluid mechanics of turbidity currents: a review of some recent studies and their geological implications. *Sedimentology*, **47**, 62-94.
- Kneller, B. and McCaffrey, W.D.** (2003) The interpretation of vertical sequences in turbidite beds: the influence of longitudinal flow. *J. Sed. Res.*, **73**, 706-713.
- Kneller, B.C. and Branney, M.J.** (1995) Sustained High-Density Turbidity Currents and the Deposition of Thick Massive Sands. *Sedimentology*, **42**, 607-616.
- Kneller, B.C., Bennett, S.J. and McCaffrey, W.D.** (1999) Velocity structure,

turbulence and fluid stresses in experimental gravity currents. *J. Geophys. Res.*, **104**, 5381-5391.

Kuenen, P.H.H. and **Menard, H.W.** (1952) Turbidity currents, graded and non-graded deposits. *J. Sediment. Petrol.*, **22**, 83-96.

Lambert, A. and **Giovanoli, F.** (1988) Records of riverborne turbidity currents and indications of slope failures in the Rhone delta of Lake Geneva. *Limnol. Oceanogr.*, **33**, 458-468.

Lintern, D.G., Hill, P.R. and **Stacey, C.** (2016) Powerful unconfined turbidity current captured by cabled observatory on the Fraser River delta slope, British Columbia, Canada. *Sedimentology*, **63**, 1041-1064.

Liu, J.T., Wang, Y.-H., Yang, R.J., Hsu, R.T., Kao, S.J., Lin, H.L. and **Kuo, F.H.** (2012) Cyclone-induced hyperpycnal turbidity currents in a submarine canyon. *J. Geophys. Res.*, **117**, C04033.

Lowe, D.R. (1982) Sediment gravity flows; II, Depositional models with special reference to the deposits of high-density turbidity currents. *J. Sed. Petrol.*, **52**, 279-297.

Lowe, R.J., Linden, P.F. and **Rottman, J.W.** (2002) A laboratory study of the velocity structure in an intrusive gravity current. *J. Fluid Mech.*, **456**, 33-48.

Lupi, M. and **Miller, S.A.** (2014) Short-lived tectonic switch mechanism for long-term pulses of volcanic activity after mega-thrust earthquakes. *Solid Earth*, **5**, 13-24.

MacVicar, B.J., Dilling, S., Lacey, R.W.J. and **Hipel, K.** (2014) A quality analysis of the Vectrino II instrument using a new open-source MATLAB toolbox and 2D ARMA models to detect and replace spikes. In: *Schleiss AJ, de Cesare G, Franca MJ, Pfister M, (eds.), River Flow 2014, CRC Press/Balkema: Leiden;* 1951-1959

Marquardt, D.W. (1963) An algorithm for least-squares estimation of nonlinear parameters. *J. Soc. Indust. Appl. Math.*, **11**, 431-441.

MathWorks^R (2018a) Granulometry of snowflakes. Available online at <https://uk.mathworks.com/help/images/examples/granulometry-of-snowflakes.html>

MathWorks^R (2018b) *lsqnonlin*. Available online at:

<https://uk.mathworks.com/help/optim/ug/lsqnonlin.html>

McLeod, P., Carey, S. and Sparks, R.S.J. (1999) Behaviour of particle-laden flows into the ocean: experimental simulation and geological implications. *Sedimentology*, **46**, 523-536.

Meiburg, E. and Kneller, B. (2010) Turbidity currents and their deposits. *Ann. Rev. Fluid Mech.*, **42**, 135-156.

Mettler-Toledo (2013) Hardware manual, ParticleTrack™ E25, Inline particle size and count. *Mettler-Toledo AutoChem, Inc.*

Mettler-Toledo (2017) Specifications – InLab 752-6mm. Available at: https://www.mt.com/gb/en/home/products/Laboratory_Analytics_Browse/pH/sensor_electrode/Conductivity_Cells/for_Bench_Meters/51344031.html.

Middleton, G.V. (1966) Experiments on density and turbidity currents II. *Can. J. Earth Sci.*, **3**, 523–546.

Middleton, G.V. (1993) Sediment deposition from turbidity currents. *Annu. Rev. Earth Planet. Sci.*, **21**, 89–114.

Middleton, G.V. and Hampton, M.A. (1973) Sediment gravity flows: Mechanics of flow and deposition. *Turbidites and Deep Water Sedimentation*, 38pp.

Mikada, H., Mitsuzawa, K., Matsumoto, H., Watanabe, T., Morita, S., Otsuka, R., Sugioka, H., Baba, T., Araki, E. and Suyehiro, K. (2006) New discoveries in dynamics of an M8 earthquake-phenomena and their implications from the 2003 Tokachi-oki earthquake using a long term monitoring cabled observatory. *Tectonophysics*, **426**, 95-105.

Miragliotta, G. (2011) The power of dimensional analysis in production systems design. *Int. J. Production Economics*, **131**, 175–182.

Monaghan, J.J. (2007) Gravity current interaction with interfaces. *Ann. Rev. Fluid Mech.*, **39**, 245-261.

Mulder, T. and Alexander, J. (2001) The physical character of subaqueous sedimentary density flow and their deposits. *Sedimentology*, **48**, 269–299.

- Mulder, T., Syvitski, J.P.M., Migeon, S., Faugères, J.C. and Savoye, B.** (2003) Marine hyperpycnal flows: Initiation, behavior and related deposits. A review. *Mar. Petrol. Geol.*, **20**, 861–882.
- Nakajima, T. and Kanai, Y.** (2000) Sedimentary features of seismoturbidites triggered by the 1983 and older historical earthquakes in the eastern margin of the Japan Sea. *Sed. Geol.*, **135**, 1-19.
- Nelson, A.R., Briggs, R.W., Dura, T., Engelhart, S.E., Gelfenbaum, G., Bradley, L.-A., Forman, S.L., Vane, C.H and Kelley, K.A.** (2015) Tsunami recurrence in the eastern Alaska-Aleutian arc: A Holocene stratigraphic record from Chirikof Island, Alaska. *Geosphere*, **11**, 1172-1203.
- Nokes, R.I., Davidson, M.J., Stepien, C.A., Veale, W.B. and Oliver, R.L.** (2008) The front condition for intrusive gravity currents. *J. Hydraul. Res.*, **46**, 788-801.
- Palanques, A., Martín, J., Puig, P., Guillén, J., Company, J.B. and Sardà, F.** (2006) Evidence of sediment gravity flows induced by trawling in the Palamós (Fonera) submarine canyon (northwestern Mediterranean). *Deep-Sea Res. I*, **53**, 201-214.
- Pantin, H.M.** (1979) Interaction between velocity and effective density in turbidity flow: Phase-plane analysis, with criteria for autosuspension. *Mar. Geol.*, **31**, 59-99.
- Paola, C., Straub, K., Mohrig, D. and Reinhardt, L.** (2009) The 'unreasonable effectiveness' of stratigraphic and geometric experiments. *Earth-Sci. Rev.*, **97**, 1-43.
- Parker, G., Fukushima, Y. and Pantin, H.M.** (1986) Self-accelerating turbidity currents. *J. Fluid Mech.*, **171**, 145-181.
- Parker, G., Garcia, M., Fukushima, Y. and Yu, W.** (1987) Experiments on turbidity currents over an erodible bed. *J. Hydraul. Res.*, **25**, 123–147.
- Patton, J.R., Goldfinger, C., Morey, A.E., Ikehara, K., Romsos, C., Stoner, J., Djadjadihardja, Y., Udrek, Ardhyastuti, S., Gaffar, E.Z. and Vizcaino, A.** (2015) A 6600 year earthquake history in the region of the 2004 Sumatra-Andaman subduction zone earthquake. *Geosphere*, **11**, 2067–2129.

- Peakall, J., Felix, M., McCaffrey, W.D. and Kneller, B.** (2001) Particulate gravity currents: perspectives. *Special publications of International Association of Sedimentologists*, 31, doi:[10.1002/9781444304275.ch1](https://doi.org/10.1002/9781444304275.ch1).
- Peakall, J., McCaffrey, W.D. and Kneller, B.** (2000) A process model for the evolution, morphology and architecture of sinuous submarine channels. *J. Sed. Res.*, **70**, 434-448.
- Pharo, C.H. and Carmack, E.C.** (1979) Sedimentation processes in short residence-time intermontane lake, Kamloops lake, British Columbia, *Sedimentology*, **26**, 523-541.
- Piper, D.J.W. and Normark, W.R.** (2009) Processes That Initiate Turbidity Currents and Their Influence on Turbidites: A Marine Geology Perspective. *J. Sed. Res.*, **79**, 347–362.
- Piper, D.J.W. and Savoye, B.** (1993) Processes of late Quaternary turbidity current flow and deposition on the Var deep-sea fan, north-west Mediterranean sea. *Sedimentology*, **40**, 557-582.
- Piper, D.J.W., Cochonat, P. and Morrison, M.L.** (1999) The sequence of events around the epicentre of the 1929 Grand Banks earthquake: initiation of debris flows and turbidity current inferred from sidescan sonar. *Sedimentology*, **46**, 79-97.
- Piper, D.J.W., Shor, A.N. and Clarke, J.E.H.** (1988) The 1929 “Grand Banks” earthquake, slump, and turbidity current. *Geol. Soc. Am. Spec. Pap.*, **229**, 77–92.
- Postma, G., Nemec, W. and Kleinspehn, K.L.** (1988) large floating clasts in turbidites: a mechanism for their emplacement. *Sediment. Geol.*, **58**, 47-61.
- Potters** (2018) Spheriglass^R 5000 solid glass microspheres – Technical data sheet. *Potters Europe*, **3-04-529-1-03**.
- Puig, P., Ogston, A.S., Mullenbach, B.L., Nittrouer, C.A. and Sternberg, R.W.** (2003) Shelf-to-canyon sediment-transport processes on the Eel continental margin (northern California). *Mar. Geol.*, **193**, 129-149.
- Puig, P., Ogston, A.S., Mullenbach, B.L., Nittrouer, C.A., Parsons, J.D. and Sternberg, R.W.** (2004) Storm-induced sediment gravity flows at the head

of the Eel submarine canyon, northern California margin. *J. Geophys. Res.*, **109**, C03019.

- Rimoldi, B., Alexander, J. and Morris, S.** (1996) Experimental turbidity currents entering density-stratified water: analogues for turbidites in Mediterranean hypersaline basins. *Sedimentology*, **43**, 527-540.
- Rottman, J.W. and Simpson, J.E.** (1983) Gravity currents produced by instantaneous releases of a heavy fluid in a rectangular channel. *J. Fluid Mech.*, **135**, 95-110.
- Sequeiros, O.E.** (2012) Estimating turbidity current conditions from channel morphology: A Froude number approach. *J. Geophys. Res.*, **117**, C04003.
- Shanmugam, G.** (1997) The Bouma sequence and the turbidite mind set. *Earth-Sci. Rev.*, **42**, 201-229.
- Shanmugam, G.** (2002) Ten turbidite myths. *Earth Sci. Rev.*, **58**, 311-341.
- Sher, D. and Woods, A.W.** (2015) Gravity currents: entrainment, stratification and self-similarity. *J. Fluid Mech.*, **784**, 130–162.
- Shiki, T., Cita, M. and Gorsline, D.** (2000) Sedimentary features of seismites, seismo-turbidites and tsunamiites—an introduction. *Sed. Geol.*, **135**, vii–ix.
- Shin, J.O., Dalziel, S.B. and Linden, P.F.** (2004) Gravity currents produced by lock exchange. *J. Fluid Mech.*, **521**, 1-34.
- Silva, A.F.T., Burggraeve, A., Denon, Q., Van der Meeren, P., Sandler, N., Van Den Kerkhof, T., Hellings, M., Vervaet, C., Remon, J.P., Lopes, J.A. and De Beer, T.** (2013) Particle sizing measurements in pharmaceutical applications: Comparison of in-process methods versus off-line methods. *Eur. J. Pharm. Biopharm.*, **85**, 1006-1018.
- Simpson, J.E.** (1982) Gravity currents in the laboratory, atmosphere, and ocean. *Annu. Rev. Fluid Mech.*, **14**, 213–234.
- Simpson, J.E. and Britter, R.E.** (1979) The dynamics of the head of a gravity current advancing over a horizontal surface. *J. Fluid Mech.*, **94**, 477-495.
- Sohn, Y.K., Choe, M.Y. and Jo, H.R.** (2002) Transition from debris flow to hyperconcentrated flow in a submarine channel (the Cretaceous Cerro Toro Formation, southern Chile). *Terra Nova*, **14**, 405-415.

- Stagnaro, M. and Pittaluga, M.B.** (2014) Velocity and concentration profiles of saline and turbidity currents flowing in a straight channel under quasi-uniform conditions. *Earth Surf. Dynam.*, **2**, 167-180.
- Stevenson, C.J., Talling, P.J., Wynn, R.B., Masson, D.G., Hunt, J.E., Frenz, M., Akhmetzhanov, A. and Cronin, B.T.** (2013) The flows that left no trace: Very large-volume turbidity currents that bypassed sediment through submarine channels without eroding the sea floor. *Mar. Petrol. Geol.*, **41**, 186–205.
- St-Onge, G., Chapron, E., Mulsow, S., Salas, M., Viel, M., Debret, M., Foucher, A., Mulder, T., Winiarski, T. and Desmet, M.** (2012) Comparison of earthquake-triggered turbidites from the Saguenay (Eastern Canada) and Reloncavi (Chilean margin) Fjords: implications for paleoseismicity and sedimentology. *Sed. Geol.*, **243**, 89-107.
- Strachan, L.J.** (2008) Flow transformations in slumps: a case study from the Waitemata Basin, New Zealand. *Sedimentology*, **55**, 1311-1332.
- Sultan, N., Gaudin, M., Berne, S., Canals, M., Urgeles, R. and Lafuerza, S.** (2007) Analysis of slope failures in submarine canyon heads: An example from the Gulf of Lions. *J. Geophys. Res.: Earth Surf.*, **112**, F01009.
- Sumner, E.J. and Paull, C.K.** (2014) Swept away by a turbidity current in Mendocino submarine canyon, California. *Geophys. Res. Lett.*, **41**, 7611-7618.
- Sumner, E.J., Siti, M.I., McNeill, L.C., Talling, P.J., Henstock, T.J., Wynn, R.B., Djajadihardja, Y.S. and Permana, H.** (2013) Can turbidites be used to reconstruct a paleoearthquake record for the central Sumatran margin? *Geology*, **41**, 763–766.
- Talling, P.J.** (2013) Hybrid submarine flows comprising turbidity current and cohesive debris flow: Deposits, theoretical and experimental analyses, and generalized models. *Geosphere*, **9**, 460–488.
- Talling, P.J.** (2014) On the triggers, resulting flow types and frequencies of subaqueous sediment gravity flows in different settings. *Mar. Geol.*, **352**, 155-182.

- Talling, P.J., Allin, J., Armitage, D.A., Arnott, R.W.C., Cartigny, M.J.B., Clare, M.A., Felletti, F., Covault, J.A., Girardclos, S., Hansen, E., Hill, P.R., Hiscott, R.N., Hogg, A.J., Clarke, J.H., Jobe, Z.R., Malgesini, G., Mozzato, A., Naruse, H., Parkinson, S., Peel, F.J., Piper, D.J.W., Pope, E., Postma, M., Rowley, P., Sguazzini, A., Stevenson, C.J., Sumner, E.J., Sylvester, Z., Watts, C. and Xu, J.** (2015) Key Future Directions for Research on Turbidity Currents and Their Deposits. *J. Sed. Res.*, **85**, 153–169.
- Talling, P.J., Paull, C.K. and Piper, D.J.W.** (2013) How are subaqueous sediment density flows triggered, what is their internal structure and how does it evolve? Direct observations from monitoring of active flows. *Earth Sci. Rev.*, **125**, 244-287.
- Tappin, D.R.** (2010) Submarine mass failures as tsunami sources: their climate control. *Phil. Trans. R. Soc.*, **368**, 2417-2434.
- Thomas, R.E., Schindfessel, L., McLelland, S.J., Creelle, S. and De Mulder, T.** (2017) Bias in mean velocities and noise in variances and covariances measured using a multistatic acoustic profiler: the Nortek Vectrino Profiler. *Meas. Sci. Technol.*, **28**, 1–25.
- Umeda, M., Yokoyama, K. and Ishikawa, T.** (2006) Observation and simulation of floodwater intrusion and sedimentation in the Shichikashuku reservoir. *J. Hydraul. Eng.*, **132**, 881-891.
- Unesco** (1983) Algorithms for computation of fundamental properties of seawater. *Unesco technical papers in marine science*, **44**, 1-58.
- Van Daele, M., Meyer, I., Moernaut, J., De Decker, S., Verschuren, D. and De Batist, M.** (2017) A revised classification and terminology for stacked and amalgamated turbidites in environments dominated by (hemi)pelagic sedimentation. *Sed. Geol.*, **357**, 72-82.
- van de Berg, J.H., Martinius, A.W. and Houthuys, R.** (2017) Breaching-related turbidites in fluvial and estuarine channels: Examples from outcrop and core and implications to reservoir models. *Mar. Pet. Geol.*, **82**, 178-205.
- van de Berg, J.H., van Gelder, A. and Mastbergeb, D.R.** (2002) The importance of breaching as a mechanism of subaqueous slope failure in fine sand. *Sedimentology*, **49**, 81-95.

- Vangriesheim, A., Khripounoff, A. and Crassous, P.** (2009) Turbidity events observed in situ along the Congo submarine channel. *Deep-Sea Research Part II: Topical Studies in Oceanography*, **56**, 2208-2222.
- Waltham, D.** (2004) Flow transformation in particulate gravity currents. *J. Sed. Res.*, **74**, 129-134.
- Weirich, F.H.** (1989) The generation of turbidity currents by subaerial debris flows, California. *Geo. Soc. Am. Bull.*, **101**, 278-291.
- Whelan, J., Murphy, E., Pearson, A., Jeffers, P., Kieran, P., McDonnell, S. and Glennon, B.** (2012) Use of focussed beam reflectance measurement (FBRM) for monitoring changes in biomass concentration. *Bioprocess Biosyst. Eng.*, **35**, 963-975.
- Wynn, E.J.W.** (2003) Relationship between particle-size and chord length distributions in focused beam reflectance measurement: stability of direct inversion and weighting. *Powder Technology*, **133**, 125-133.
- Xu, J.P.** (2010) Normalized velocity profiles of field-measured turbidity currents. *Geology*, **38**, 563-566.
- Xu, J.P.** (2011) Measuring currents in submarine canyons: Technological and scientific progress in the past 30 years. *Geosphere*, **7**, 868-876.
- Xu, J.P., Noble, M.A. and Rosenfeld, L.K.** (2004) In-situ measurements of velocity structure within turbidity currents. *Geophys. Res. Lett.*, **31**, L09311.
- Xu, J.P., Sequeiros, O.E. and Noble, M.A.** (2014) Deep-Sea Research I Sediment concentrations, flow conditions, and downstream evolution of two turbidity currents, Monterey Canyon, USA. *Deep-Sea Res. I*, **89**, 11-34.
- Xu, J.P., Swatzenski, P.W., Noble, M. and Li, A.-C.** (2010) Event-driven sediment flux in Hueneme and Mugu submarine canyons, Southern California. *Mar. Geol.*, **269**, 74-88.

Appendix A

Natural flow data

Table A.1 - Parameters of natural flows; this data set is used in Chapter 5.

Area	Flow event	References	Slope (radian)	Velocity (m/s)	Flow height (m)	Concentration
Offshore Newfoundland	Grand Bank 1929	Heezen & Ewing (1952); Piper et al. (1988); Piper et al. (1999); Talling et al. (2013)	0.026	19	160	0.0423 [¥]
			0.026	20	270	0.0278 [¥]
			0.174	19	160	0.0131 [¥]
			0.174	20	270	0.0086 [¥]
Offshore Taiwan	Pingtung earthquake-generated 2006	Hsu et al. (2008); Talling et al. (2013)	0.021	20	100 [*]	0.0867 [¥]
			0.014	5.7	100 [*]	0.0092 [¥]
Offshore Japan	Tokachi-oki earthquake-generated 2003	Mlkada et al. (2006)	0.036	1.4	60	0.0005 [¥]
Gioia Canyon, Italy	1977	Talling et al. (2013)	0.04	4.5	20 [*]	0.0145 [¥]
Offshore southwest Oahu, Hawaii	Hurricane Iwa, 1982	Dengler et al. (1984)	0.042	2	25 [*]	0.0022 [¥]
Scripps and La Jolla, California	Wave action	Xu, 2004; Talling et al. (2013)	0.017	1.9	65 [*]	0.0014 [¥]

Zaire Canyon, West Africa	2004	Vangriesheim et al. (2009)	0.004	3.5	120*	0.0072 [¥]
	2009	Cooper et al. (2013)	0.006	2.5	120*	0.0026 [¥]
Taiwan	Typhoon Morakot, 2009	Carter et al. (2012); Talling et al. (2013)	0.019	16.6	100*	0.0632 [¥]
			0.007	10.3	100*	0.0491 [¥]
Squamish River delta, Canada	2004-2012 field data	Hughes Clarke et al. (2012); Talling et al. (2013)	0.087	0.5	40*	0.0001 [¥]
Itirbilung Fjord		Talling et al. (2013)	0.099	0.36	2	0.0005 [¥]
Lake Geneva, Switzerland		Lambert & Giovanoli (1988); Talling et al. (2013)	0.020	0.5	13*	0.0004 [¥]
Monterey Canyon		Xu, 2011; Talling et al. (2013); Xu et al. (2014)			80	0.0006
					52.5	0.0002
					57.1	0.0004
					23.9	0.0136
					38.2	0.0011
					31.1	0.0016
Var Canyon, Mediterranean	Nice Airport, 1979	Piper & Savoye (1993)	0.140	11.3	30	0.09
Typhoon Kalmaegi, Taiwan	2008	Liu et al. (2012)			150	0.0017
Hueneme and Mugu Canyon		Xu et al. (2010); Xu (2010); Talling et al. (2013)	0.037		25	0.0033

La Fonera Canyon		Palanques et al. (2006); Talling et al. (2013)		0.38	22	0.0001
Shichikashuku Reservoir, Japan		Umeda et al. (2000); Talling et al. (2013)		0.08	3	0.000028
Katsurazawa Reservoir, Japan		Chikita & Okumura (1990); Chikita (1990); Talling et al. (2013)		0.32	6	0.0007
Lillooet Lake, British Columbia		Best et al. (2005); Gilbert et al. (2006); Talling et al. (2013)		0.58	16	0.0002
Kluane Lake, Yukon		Talling et al. (2013)		0.6	13	0.0005
Lake Lugano, Switzerland		De Cesare et al. (2006); Talling et al. (2013)		0.17	10	0.0002
Expectation Lake, British Columbia		Talling et al. (2013)		1.1	3	0.0001
Kamloops Lake, British Columbia		Pharo & Carmack (1979); Talling et al. (2013)		0.28	10	0.00001
Lake Wallensee, Switzerland		Talling et al. (2013)		0.5	7	0.0002
Lake Superior		Talling et al. (2013)		0.15	16	0.00002
Bute Inlet, Canada		Talling et al. (2013)			40	0.005
Rupert Inlet		Talling et al. (2013)			5	0.0001

*Flow heights that were estimated based on channel depths.

¥Flow concentrations that were estimated using the frictional-gravitational force balance model of Parker et al. (1987).

Appendix B

MatLab™ script in the processing of SEM images, provided by Thomas, R.E. (2017)

```

% Process SEM image(s) to extract grain size distribution(s) and
summary
% statistics for vertical slices of the image(s), with width max
^diameter
% and 50% overlap, together with the entire image(s)
%
% Method is based on The Mathworks' Granulometry of Snowflakes
example
%
% Currently outputs particle size distribution (distribOut),
cumulative
% particle size distribution (cumDistribOut), d16, d50, d84,
dmean, d84-d16
% and porosity (these 6 variables to output). Also saves median-
filtered
% raw image (I), black and white thresholded raw image (BW),
slice bounds
% (in pixels), image scale and user input parameters (march
direction (left
% to right or right to left), width of size classes (phi
intervals),
% threshold (grayscale threshold between background and
particles)
%
% distribOut and cumDistribOut are arranged as first row -
centroid of slice
% (NB last column = whole image); first column - upper bound of
particle
% size class; rows 2:nclasses, columns 2:nSlices+1 - percent in
class or
% cumulative percent in class
%
% output is arranged as first column - centroid of slice (NB last
row =
% whole image); columns 2:7 - d16, d50, d84, dmean, d84-d16,
porosity
%
%% User MUST input march direction (marchDir; left to right [1]
or right to
%% left [other]), width of size classes (phiGrad; phi intervals),
threshold
%% (thresh; grayscale threshold between background and
particles), infill
%% (boolean array defining whether imfill is applied to holes
between
%% particles)
%
% Copyright 2017 Rob Thomas, r.e.thomas02@members.leeds.ac.uk
% School of Earth and Environment,
% University of Leeds,
% Woodhouse Lane,

```

```

% Leeds. LS2 9JT. UK
% $Date: 2017/11/23 16:00:00 $
% All rights reserved.
%
% Redistribution and use in source and binary forms, with or
without
% modification, are permitted provided that the following
conditions are met:
%   * Redistributions of source code must retain the above
copyright
%   notice, this list of conditions and the following
disclaimer.
%   * Redistributions in binary form must reproduce the above
copyright
%   notice, this list of conditions and the following
disclaimer in the
%   documentation and/or other materials provided with the
distribution.
%   * Neither the name of the University of Leeds nor the names
of its
%   contributors may be used to endorse or promote products
derived from
%   this software without specific prior written permission.
%
% THIS SOFTWARE IS PROVIDED BY THE COPYRIGHT HOLDERS AND
CONTRIBUTORS "AS IS" AND
% ANY EXPRESS OR IMPLIED WARRANTIES, INCLUDING, BUT NOT LIMITED
TO, THE IMPLIED
% WARRANTIES OF MERCHANTABILITY AND FITNESS FOR A PARTICULAR
PURPOSE ARE
% DISCLAIMED. IN NO EVENT SHALL THE COPYRIGHT HOLDER BE LIABLE
FOR ANY
% DIRECT, INDIRECT, INCIDENTAL, SPECIAL, EXEMPLARY, OR
CONSEQUENTIAL DAMAGES
% (INCLUDING, BUT NOT LIMITED TO, PROCUREMENT OF SUBSTITUTE GOODS
OR SERVICES;
% LOSS OF USE, DATA, OR PROFITS; OR BUSINESS INTERRUPTION)
HOWEVER CAUSED AND
% ON ANY THEORY OF LIABILITY, WHETHER IN CONTRACT, STRICT
LIABILITY, OR TORT
% (INCLUDING NEGLIGENCE OR OTHERWISE) ARISING IN ANY WAY OUT OF
THE USE OF THIS
% SOFTWARE, EVEN IF ADVISED OF THE POSSIBILITY OF SUCH DAMAGE.
%
*****
*****
clear cumDistribOut distribOut intensity_area
intensity_area_prime output
% Parallelise the imopen loop
numCores = feature('numcores');
p = parpool(numCores);
%%
% Fixed parameters
%
% thresh sets the highest pixel value that should be considered
background.
% 65 seems about right but again, you might want to play with it
thresh = [44, 62, 49];
%
% infill is a boolean specifying whether the imfill command is
used or not

```

```

infill = [0 1 1];
%
% phiGrad sets the phi gradation of the output
phiGrad = 0.25;
%
% marchDir sets the direction the moving window moves in
marchDir = 1;
%%
% Pre-process the image
%
% Ask the user to select the image to process
[fileName, pathName, fileTypeIndex] =
uigetfile({'*.jpg;*.tif;*.png;*.gif', 'All Image Files';...
          '*.*', 'All Files' }, 'Select the image file that
contains the largest particle in all the scans');
%
% if Cancel is selected then return
if isequal (fileTypeIndex, 0); return; end
%
% Open the image; isolate the first channel
cd(pathName);
I = imread(fileName);
I = I(:,:,1);
%
% Set imageHeight and filterSize depending on the resolution of
the image
if isequal(size(I, 2), 8192)
% imageHeight sets the height of the image
    imageHeight = 4096;
% filterSize sets the size of the median filter to remove
speckle;
% 7x7 pixels seems to be the optimum but you might want to play
with it
    filterSize = 7;
else
    imageHeight = 8192;
    filterSize = 15;
end
%%
%
% Get the dimensions of the scale bar and set the scale
multiplier
prompt = 'Enter the "View field" in microns then press enter
(leave blank if it is not printed)';
scale = input(prompt);
width = size(I, 2);
if isempty(scale)
    h = figure;
    imagesc(I), colormap 'gray', axis equal
    title('Select the left and right edges of the scale bar');
    hold on
    [x, y] = ginput2(2);
    plot(x, y, 'g');
    prompt = 'Enter the width of the scale bar in microns then
press enter';
    scale = input(prompt);
    width = abs(x(1)-x(2));
else
    h = figure;
    imagesc(I), colormap 'gray', axis equal
    hold on

```

```

end
%
scale = scale / width;
%
% Get the dimensions of the largest particle
title(['Now, select the edge of the largest particle so that the
line connecting' ...
' the two points would pass through the centre of the
particle']);
[x, y] = ginput2(2);
plot(x, y, 'r');
%
max_radius = ceil(0.5 * max([abs(x(1)-x(2)), abs(y(1)-y(2)),
sqrt((x(1)-x(2)).^2 + (y(1)-y(2)).^2)])); % radius = half
diameter
radius_range = 0:max_radius;
pause(1);
close(h);
%%
% Initialise the loop to compute particle areas
disp('Computing particle areas... Please wait');
% Pre-process the image
%
% Ask the user to select the image to process
[fileNames, pathName, fileTypeIndex] =
uigetfile({'*.jpg;*.tif;*.png;*.gif', 'All Image Files';...
'*. *', 'All Files' }, 'Select input file(s)',
'MultiSelect', 'on');
%
% if Cancel is selected then return
if isequal (fileTypeIndex, 0); return; end
cd(pathName);
%
% Count the number of files selected by the user
no_files = 1;
if iscellstr(fileNames)
    no_files = numel(fileNames);
end
%
% Loop over all of the selected files
for f = 1: no_files
%
% Get the file name to open
if isequal(no_files, 1)
    fileName = fileNames;
else
    fileName = char(fileNames(1,f));
end
disp(['Pre-processing image ' num2str(f) '... Please wait']);
%
% Open the image and perform a median filter to remove speckle
I = imread(fileName);
I = I(:,:,1);
I = medfilt2(I, [filterSize filterSize]);
%
% Threshold the image to isolate particles and background
BW = I(1:imageHeight,:);
BW(BW<=thresh(f)) = 0;
BW(BW>thresh(f)) = 1;
%

```

```

% Fill any "holes" within individual particles to reduce the
number of
% erroneous particle splits
    if infill(f)
        BW = imfill(BW, 'holes');
    end
%
% Set the edges of each slice
    radius_range = 0:max_radius;

    if marchDir == 1
        scanEdge = 1:marchDir*2*max_radius:size(BW,2);
        if ~isequal(scanEdge(end), size(BW,2))
            scanEdge(end+1) = size(BW,2);
        end
    else
        scanEdge = size(BW,2):marchDir*2*max_radius:1;
        if ~isequal(scanEdge(end), 1)
            scanEdge(end+1) = 1;
        end
        scanEdge = fliplr(scanEdge);
    end

%
% Set the first column of the output array
    distribOut(:,1) = 2.^(floor(log2(0.002 * 0.5 .* scale)):
phiGrad: ceil(log2(0.002 * radius_range(end-1) .* scale)));
    cumDistribOut(:,1) = distribOut(:,1);
    output = zeros(size(scanEdge, 2)-1, 7);
    output(1:end-1, 1) = 0.001 * scale * 0.5 * (scanEdge(3:end) +
scanEdge(1:end-2));
    output(end, 1) = marchDir * 0.001 * scale * scanEdge(end);
%
% Adjust the edges of slice so that they're correct
    scanEdge(2,1:(end-2)) = scanEdge(1, 3:end);
    scanEdge(:, (end-1)) = [1; scanEdge(1,end)];
    scanEdge(:,end) = [];
%
% The first column of intensity_area_prime should not change in
the loop
    intensity_area_prime = 0.002 * radius_range(1:end-1)' .*
scale; % particle diameter
    intensity_area_prime(1, 1) = 0.001 * scale;

    for i = 1:size(scanEdge, 2)
        intensity_area = zeros(size(radius_range));
%
% Loop over the particle radii, computing the area shaded by
discs of
% radius 'r' or smaller
        temp = BW(:, scanEdge(1, i):scanEdge(2, i));
        parfor r = radius_range
            remain = imopen(temp, strel('disk', r));
            intensity_area(r + 1) = sum(remain(:));
        end
%
% In their snowflake granulometry example, The Mathworks claim
that "A
% significant drop in intensity surface area between two
consecutive
% openings indicates that the image contains objects of
comparable size to

```

```

% the smaller opening. This is equivalent to the first derivative
of the
% intensity surface area array, which contains the size
distribution of the
% particles in the image. Calculate the first derivative with the
DIFF
% function."
    temp = find(diff(intensity_area) > 0);
    intensity_area(temp) = intensity_area(temp+1);
    intensity_area_prime(:,2) = -diff(intensity_area)';
%
% Use the hist command to create phi-scale histogram
%
% First, arrange a vector of number of counts per diameter
    vect = repelem(intensity_area_prime(1:end,1),
intensity_area_prime(1:end,2));
%
% Second, use discretize and normalise
    distribOut(:,i+1) = 100 * histcounts(vect, [0;
distribOut(:,1)] ./ intensity_area(1);
    cumDistribOut(:,i+1) = cumsum(distribOut(:,i+1));
%
% Summary stats
    output(i, 2) = 2.^interp1q(cumDistribOut(:,i+1),
log2(cumDistribOut(:,1)), 16);
    output(i, 3) = 2.^interp1q(cumDistribOut(:,i+1),
log2(cumDistribOut(:,1)), 50);
    output(i, 4) = 2.^interp1q(cumDistribOut(:,i+1),
log2(cumDistribOut(:,1)), 84);
    output(i, 5) = mean(vect);
    output(i, 7) = 1 - (intensity_area(1) ./ ((scanEdge(2, i)
- scanEdge(1, i) + 1) * imageHeight));
    end
    output(:, 6) = 0.5 * (output(:, 4) - output(:, 2));
    distribOut = [0 output(:,1)'; distribOut];
    cumDistribOut = [0 output(:,1)'; cumDistribOut];
%
% Save outputs
    tempOut = thresh(f);
    save([ pathName, filesep, fileName(1:end-4), '.mat' ], 'BW',
'cumDistribOut', 'distribOut', 'filterSize', 'I', 'marchDir',
'output', 'phiGrad', 'scale', 'scanEdge', 'thresh');
    clear cumDistribOut distribOut tempOut
    disp(['Image ' num2str(f) ' of ' num2str(no_files) ' ...
completed']);
end
%
%
% % Plot a few figures
% figure
% plot(output(1:end-1,3), output(1:end-1,1), 'k-')
% hold on
% plot(output(1:end-1,2), output(1:end-1,1), 'k:')
% plot(output(1:end-1,4), output(1:end-1,1), 'k:')
% grid on
% title('Vertical variation of d50, d16 and d84')
% xlabel('Diameter of particles (microns)')
% ylabel('Vertical distance (mm)')
%
%
% temp = cell(1, size(cumDistribOut,2)-2);
% figure
% for i = 2:(size(distribOut,2)-1)

```

```
% plot(distribOut(:,1), distribOut(:,i))
% temp{1, i-1} = num2str(distribOut(1,i));
% hold on
% end
% grid on
% title('Vertical variation of particle size distributions')
% xlabel('Diameter of particles (microns)')
% ylabel('Percent total particle area in class (% finer)')
% legend(temp)
% %
% figure
% for i = 2:(size(cumDistribOut,2)-1)
%     plot(cumDistribOut(:,1), cumDistribOut(:,i))
%     hold on
% end
% grid on
% title('Vertical variation of cumulative particle size
distributions')
% xlabel('Diameter of particles (microns)')
% ylabel('Cumulative percent total particle area (% finer)')
% legend(temp)
% %
% Tidy up:
% Release parpool
delete(gcf('nocreate'));
% Clear
clear variables
```